UNIVERSITY OF LIVERPOOL

Compressed Sensing on Terahertz Imaging

Thesis submitted in accordance with the requirements of the University of Liverpool for the degree of Doctor of Philosophy

by

Lin Liu

May 2017

Department of Electrical Engineering and Electronics

Abstract

THz range is in the middle of the well studied electronics part and photonics part of the electromagnetic field. Since THz imaging can be applied in many applications such as nondestructive detections of chemical compositions, medical diagnosing, chemical mapping and detection of drugs and explosives, security check, and industry quality control, THz time-domain imaging systems have been studied and developed rapidly over the last 20 years.

For now most terahertz (THz) time-domain imaging experiments are implemented by raster scanning, which either scan the sample or the THz beam. It might take hours to get an image depending on the total pixel numbers required. It is not suitable for real time applications due to the slow imaging speed. There are other systems which can provide faster speed such as systems using focal plane arrays, but they have poor performance in terms of sensitivity and cost. No spectroscopic information could be obtained from those systems.

Developed from the concept of compressive sensing (CS), random projection method using binary sampling operators (masks) were used to develop faster and higher resolution THz imaging systems. Compared with conventional raster scanning THz imaging systems, no scanning of the THz beam or the sample is needed. The imaging process significantly speeds up with acceptable image resolutions. Spectroscopic information can also be obtained.

Researches on CS sampling operators, especially those which are not random matrixes are within the major area of CS research. Designed sampling operators in CS imaging are more efficient corresponding to practical applications. The main design criteria are imaging quality, imaging speed, resolution, sampling rate and implementation complexity. The designed operators need to be validated by experiment. Feedback from validation is useful for the designing process.

Two CS imaging systems which can provide fast physical results to support simulation results in CS sampling operator design were studied in this thesis. Here

different CS sampling operators were applied in the CS imaging systems and discussed in terms of imaging quality, imaging speed, resolution, sampling rate and implementation complexity. By designing better masks, the sampling rate needed for a CS imaging system can be reduced and the calculation speed of the image reconstruction process can be increased. Both of these benefits can increase the speed of a CS imaging procedure.

A spinning disk with binary patterns was designed to speed up the transfer speed of sampling operators from one to another. The binary patterns on the disk were designed Toeplitz structured sampling operators. During imaging process, the disk rotates automatically and a series of sampling operators can be captured from an effective imaging window. This spinning disk set up, allows CS imaging experiments to be performed automatically and continuously, hence increasing the imaging speed.

This spinning disk was made from a 0.28mm-thick steel plate. The diameter of the plate was 200mm. A number of 2mm-diameter holes were chemically etched on this steel plate. Each hole was 100% transparent to light while the stainless steel was 100% opaque to light. This disk had no substrate so there was no absorption and dispersion caused by the substrate material. The size of the round holes on the disk was relatively large so the performance against diffraction and scattering effects should be acceptable. The spinning disk had been applied in THz CS imaging processes using a strong THz beam in the Daresbury particle accelerator lab, and in a conventional EO crystal based THz time domain system. The results showed that both spectral and spatial can be obtained from THz CS imaging using the spinning disk.

To further increase the imaging speed, the idea of increasing the number of detectors in CS imaging experiments showed up along with the developments of CS sampling operators. By dividing the images into blocks and applying CS imaging separately and simultaneously to each block, the speed of a CS imaging procedure can be further increased. Block CS experiments have been performed experimentally for the first time using the spinning disk to demonstrate its potential in CS THz imaging.

Acknowledgments

My PHD work and thesis were finished with help and support from many people who are acknowledged here. Mostly, I want to say thank you to my supervisor, Dr. Yaochun Shen. I deeply appreciate the valuable suggestions about my research he gave to me over the past few years. He has supported me with his knowledge and experience in his research area. I am grateful to Dr. Lu Gan who gave me many valuable ideas about my research and shared her knowledge about signal processing with me. It was really a great honor for me to work with her team in several projects. I would also like to thank Prof. Yi Huang for supporting me in my research.

I am grateful to the Department of Electrical Engineering and Electronics for the support I received during my study. I would like to thank Dr Xu Zhu and Dr Harm Van Zalinge for their suggestions every year during annual presentation. Also, I would like to thank Mark Surman for supporting my experiments in Daresbury Lab.

Finally, I would like to thank my family and all my friends who have supported me during these years.

Table of Contents

List of Figures

List of Tables

Abbreviations

2D: two-dimensional
3D: three-dimensional
ADC: analog-to-digital converter
API: active pharmaceutical ingredient
AR(1): autoregressive model of order 1
ATR: attenuated total reflection
BS: beam splitter
BWO: backward wave oscillator
CCD: charge-coupled device
CMOS: complementary metal-oxide semiconductor
CS: compressed/compressive sensing/sampling
CW: continuous wave
DAQ: data acquisition
DCT: discrete cosine transform
DFG: difference-frequency generation
DMD: digital micro-mirror device
DSP: digital signal processing
EO: electro-optic
FEL: free electron laser
FET: field-effect transistor
FIR: far infrared
FOCUSS: focal underdetermined system solver
FTIR: Fourier transform infrared
LED: light emitting diode
LTG: low-temperature-grown
MMSE: minimum mean square error
MRI: magnetic resonance imaging
MSE: mean square error
NEP: noise equipment power
NM: number of measurements
NP: non-deterministic polynomial-time
NSP: null space property
OMP: orthogonal matching pursuit
PCA: photoconductive antenna
PCB: print circuit board
PD: photodiode
PM: parabolic mirror
PSNR: peak signal-to-noise ratio
QCL: quantum cascade laser
RGB: red-green-blue
RIP: restricted isometry property
RNG: random number generator
SDC: spinning disk configuration
SFG: sum-frequency generation
SNR: signal-to-noise ratio
SOCP's: second order cone programs
SR: sampling rate
TDS: terahertz time-domain spectroscopy
THz: terahertz
TPI: terahertz time-domain (pulsed) imaging
TV-min: total-variation minimization

List of Publications and Conference Presentations

[1] L Gan, L Liu, YC Shen, “Golay sequence for partial Fourier and Hadamard compressive imaging”, 2013 IEEE International Conference on Acoustics, Speech and Signal Processing (ICASSP), (2013) 6048-6052

[2] Lin Liu, Lu Gan, Yi Huang and Yaochun Shen, “Terahertz imaging via block-based compressive sensing,” IET Colloquium on Millimeter-wave and Terahertz Engineering & Technology, March 6, 2014, Liverpool, UK.

[3] Z. J. Zhang, L. Liu, L. Gan, Y. Huang, Y. C. Shen, “Compressed sensing for rapid THz imaging,” IET Colloquium on Millimeter-wave and Terahertz Engineering & Technology, March 31, 2016, London, UK.

[4] L. Liu, Z. J. Zhang, L. Gan ,Y. C. Shen, Y. Huang, “A Spinning Disk as a Spatial Light Modulator for Rapid Infrared Imaging”, 2016 UK-Europe-China Workshop on mm-waves and THz Technologies committee (UCMMT2016), Sept 05-07, 2016, Qingdao, China.

[5] Z. J. Zhang, L. Liu, Y. C. Shen,“A Spinning Disk as a Spatial Light Modulator for Rapid Infrared Imaging”, IET Microwaves, Antennas & Propagation, 2017, 11, (3), p. 317-323, DOI: 10.1049/iet-map.2016.0398.

Chapter 1

Introduction

1.1. Motivation of the work

Terahertz (THz) range is in the middle of the well studied electronics part and photonics part of the electromagnetic field as shown in Figure.1.1. Unlike its neighbour frequency ranges on the electromagnetic field, THz radiation has not been well studied, and many of its features have not been proved and developed into applications. Many features of THz radiation and their potential applications have made research in this area very popular over the last twenty years. In this thesis, imaging using pulsed (time domain) THz radiation will be mainly discussed among all the features and potential applications.

Different crystalline substances have different inter-molecular or intra-molecular vibration modes, which affect the spectral features of those materials in THz range [1, 2]. Some chemical compositions (many chemical explosives) have typical and identifiable THz spectral features. Another important feature of THz radiation is that it can propagate through non-metal packages such as bags, boxes and suitcases but only with difficulty through water. These features combine together make THz imaging can be applied in many applications such as nondestructive detections of chemical compositions, medical diagnosing, chemical mapping and detection of drugs and explosives, and industry quality control [3-7].

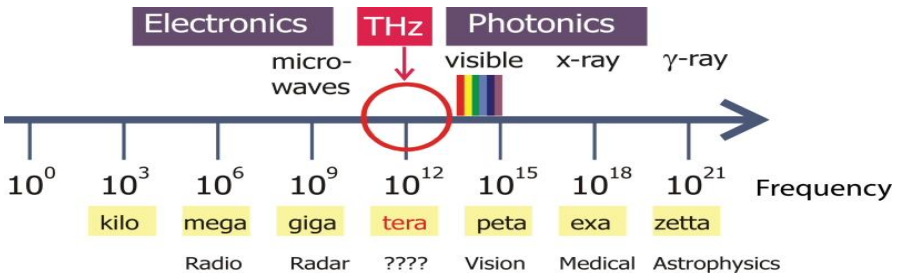

Figure.1.1 Location of THz range showed on the electromagnetic field.

THz time-domain imaging systems have been studied and developed rapidly for the last 20 years. Most of those systems used photoconductive emitters as THz sources. The THz powers from those emitters were relatively low compared with the current single point detectors, so for now most terahertz pulsed imaging experiments have been implemented by raster scanning. This approach either scans the focused THz beam or the sample, point by point, and then the THz beam is collected by a single point detector. The imaging speed is limited by the point by point scanning process and not fast enough for real time applications such as vivo medical imaging, security imaging or industrial quality checking. There are systems using focal plane detector arrays which can provide faster THz imaging speed [8, 9]. However, these systems are expensive and require higher computation complexity. More importantly, no spectroscopic information can be obtained from those systems. The number of measurements can be reduced by interferometric or tomographic approaches which apply non-uniform sampling in the Fourier domain [10-12]. However, those systems still need raster scanning, either the sample or the THz beam. Therefore, it is necessary to improve the current techniques to achieve a fast, cost-effective THz imaging system.

Fortunately the theory called compressive sensing (CS) [13, 14] has been proposed and developed over the past 10 year. Based on the CS theory, sparse signals can be sensed on a reduced sampling rate. A 2-D THz image can meet the need for most THz imaging applications and it can be considered as sparse signal. Chan *et al.* [15, 16] reported the first THz imaging system based on the concept of CS. The proposed CS THz imaging system can significantly increase the imaging speed by replacing the conventional raster scanning process. In the CS THz imaging set up, the THz wave travelling through the sample from the source to the single point detector was modulated by a series of spatial light modulators (also known as masks or sampling operators). The linear projection of a sample and the series of 2D spatial modulators were recorded by a single point THz detector. These recorded THz data in corresponding to each 2D spatial modulator were used to reconstruct a 2D THz image.

Each spatial modulator was a binary (either opaque or transparent to THz waves) image of 32×32 pixels [15]. By using this system, there was no need for raster scanning either the sample or the THz beam. For the same resolution, the numbers of measurements needed were significantly reduced hence the imaging speed was significantly increased.

The CS THz system reported by Chan *et al.* [15, 16] had not been proved to obtain any spectral information while Yaochun *et al.* [17] reported a CS THz system which can obtain spatial and spectral information of a sample at the same time. The time domain CS THz set up was similar to Chan's, while the spatial light modulators applied in this system performed much better.

The imaging speed could be further increased by speeding up the transfer rate from one spatial light modulator to another. A spinning disk based CS THz configuration had been reported by Hao *et al.* [18]. In this configuration, the spatial light modulators were fabricated on a spinning disk. During imaging process, the spatial light modulators were transferred automatically by an electric rotation stage so the imaging speed was highly increased. By using those spatial light modulators on the spinning disk, THz images with acceptable resolution and quality were obtained. However, those spatial light modulators were made on a PCB substrate which absorbs THz radiation non-uniformly. This absorption added relatively large noise to the imaging process, plus the design defect of the spatial light modulator patterns, made it impossible for this configuration to achieve any spectral information due to the low signal to noise ratio.

The motivation of this thesis is to further improve the performance of current CS THz systems in terms of imaging quality and imaging speed. In the current spinning disk configuration, the non-uniform absorption of the substrate and the design defect of the spatial light modulator patterns all contributed to the noise. The patterns were a number of 1-mm-diameter squares randomly carved on the PCB board. The THz radiation spans a frequency range from 300 GHz to 10 THz (wavelength is from 1mm to 30um). Thus, when the pixel size of such patterns was close to the wavelength of

THz radiation, the scattering and the diffraction effects were no longer negligible. The scattering effect of THz radiation at the sharp corners of the squares also degraded the overall signal to noise rate. These all added noise to the imaging procedure and affected the encoding accuracy thus weakening the quality of the reconstructed images. Better designs of spatial light modulators and spinning are needed to obtain both the spatial and spectral information of a sample from CS THz system. The sampling rate and the computational complexity of CS imaging process could be reduced by a better design of spatial light modulators which would also increase the THz imaging speed.

1.2. Organization of the Thesis

Chapter 2 studied the background of THz imaging and compressive sensing respectively. In section 2.1, the sources and detectors of THz radiation, THz-TDS system, THz imaging and the corresponding applications were discussed. As a powerful method which can be used for improving the performance of THz imaging systems, CS was introduced in section 2.2. Following a brief introduction and background of CS, discussions of the sparse signal model, alternative constructions for structured CS matrices were presented. Then the theory and algorithms for sparse recovery were discussed.

Chapter 3 demonstrated some main criteria for spatial light modulator designing on two experiment implementations which provided fast physical validation. The brief guidelines in CS spatial light modulator designing were introduced with experiment results. These results were discussed in terms of imaging quality, imaging speed, resolution, sampling rate and implementation complexity [19]. Compared to conventional CS system, these two implementations could provide rapid physical validation and feedbacks for the designing process.

Chapter 4 introduced a new designed spinning disk for CS THz imaging. The disk was fabricated on a piece of steel plate, so no substrate was needed. This not only

increased the intensity of THz signal transmit through the disk but also minimized the noise caused by the non-uniform substrate. The 1-mm-diameter circle spatial light modulator patterns gave this disk better performance against the scattering and the diffraction effects. The performance of the spinning disk was tested in different implementations. A video rate CS imaging system in IR range using this new designed disk was demonstrated to achieve 10 frames per second.

Chapter 5 gave a brief introduction to the concept of block CS imaging and experiments that had been done on two implementations using the spinning disk for block based CS imaging. Based on block CS theory, the resolution, imaging speed and reconstruction speed can be enhanced. The hardware limits for resolution and reconstruction calculations were broken by blocked CS. Some of the results are published in [20]. The results showed the block CS approach have great potential in THz imaging.

Chapter 6 demonstrated how the new spinning disk was applied in THz imaging systems. The experiments carried out using ultra-strong THz beam from the particle accelerator in Daresbury lab were aimed at studying the imaging properties of THz radiation after transmitting through food patterns. A typical time domain THz system based of femto-second laser, photoconductive antenna and EO crystal was implemented. Some CS THz imaging experiments had been done on this system to demonstrate how spatial and spectral information could be obtained using the spinning disk.

Chapter 7 concluded the current achievements, i.e., mask designing in THz CS imaging and block based CS (Chapter 3, 4& 5), video rate THz imaging (Chapter 5), THz imaging using the spinning disk (Chapter 6). All the skills and experience obtained were shown here. In addition, this chapter included some suggestions for future work.

Chapter 2

Background

2.1. Terahertz imaging

From the 1960's, due to limited resources (e.g. sensitive detectors, components for manipulations of terahertz radiation, etc.), studies for terahertz spectrum had developed slowly. There has not been a proper solution to spectroscopy in the range of THz until the 1980's when method called THz time-domain spectroscopy (THz TDS) based on femtosecond laser emerged [21-24]. The method utilized the optical excitation of photoconductive antennas. The image showed in b) of Figure.2.1 was obtained by using THz TDS by Hu and Nuss [4, 25]. This great achievement was a milestone in the history of THz imaging and started a new era of THz imaging technologies. New derivative approaches based on THz TDS were developed by researchers using the ultra fast laser technique, especially the Ti:sapphire femtosecond laser [26]. In this section, we would like to introduce THz sources and detectors, THz-TDS, THz imaging and corresponding applications.

Figure.2.1 The first THz-TDS image in the world. (a) was a photo of a packaged integrated circuit. (b) was a THz image obtained from a).. Figure adapted from [4].

2.1.1. THz sources

A few THz sources make use of photoconduction, optical rectification, photo mixing, backward wave oscillator (BWO), far infrared laser (FIR laser), quantum cascade laser (QCL) and free electron laser (FEL), which will be briefly discussed in this section.

A. Photoconduction

THz emitters driven by ultra short lasers, based on frequency down conversion within optical regions, are the most popular broadband time domain THz sources in current researches [27]. One of the most common methods is photoconduction, which uses femtosecond laser pulses to excite a photoconductive antenna. The content in the frequency domain is determined by the dynamics of transient current which excite the electromagnetic field. In other words, a radiation in the range of THz will be excited by a current transient which is between a few hundred femtoseconds and a few picoseconds in time scale [28]. To make it easier to understand, Figure.2.2 [29, 30] illustrates how a biased photoconductive antenna generates THz pulses. The photoconductive gap is biased by the metallic electrodes. Current impulses are produced when there are femtosecond laser pulses impinging onto the gap. Photons with higher energy can excite electrons energy level transition to conduction band in the photoconductor. THz pulses will be generated from the antenna by the current transients when excited by femtosecond laser pulses. More detailed information about THz pulses generation and detection from biased semiconductor antennas are discussed in [31].

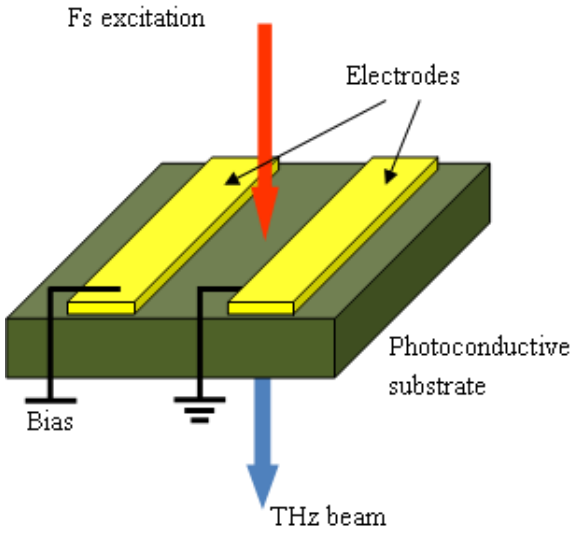

Figure.2.2 Photoconductive antenna emitter for broadband THz pulses generation.

B. Optical Rectification

There is another approach called optical rectification which can generate broadband THz radiation. Optical rectification refers to a difference frequency mixing process happened in no-linear medium. It can be considered as a frequency doubling process, in which a polarization will be induced in the non-linear medium that is the difference between individual frequencies instead of their sum as showed in Figure.2.3. To make it more clear, the time domain view of a distribution of different frequencies could be treated as an electric field transient, which has an envelope with a similar shape to the laser pulse. THz wave can be generated by making use of difference-frequency mixing of an electro-optic crystal which mixed all the frequencies of a femtosecond laser pulse [28]. Firstly published in 1969 [32], nonlinear frequencies mixing of laser beams in LiNbO3 and quartz was proved to have the potential generating THz radiation. Many different materials (e.g. LiNbO3 and LiTaO3, GaAs and CdTe, and ZnTe) were proved to achieve ultra broadband generation of THz pulses using this method [33-40]. THz generation and detection using four-wave mixing in focal region of intense laser field are popular in this area in recent years [41-43].

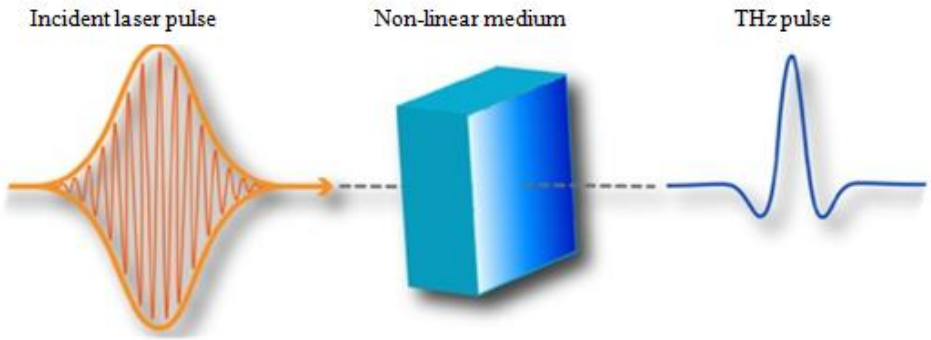

Figure.2.3 Optical rectification process in non-linear crystal.

The non-linear crystal is not biased so the THz output power is totally for the incident laser pulse. Efficient difference-frequency mixing of every frequency component in the spectrum of the laser pulses is required in the process of generation of THz radiation. There are two factors that determine the bandwidth and shape of the THz transient. One is the bandwidth of the excitation pulse and the other is the phase

matching between the generated THz field and the near-infrared pump beam [28]. The THz photons interact with the pump photons in nonlinear crystals and create sidebands to the pump frequencies by difference and sum frequency generation (DFG and SFG). This SFG process which leads to the electro-optic effect is widely used for optical detection [28].

The typical frequency range of generated THz radiation is between 0.1 and 3 THz or even higher by applying photoconduction and optical rectification approaches. The range of average power levels is from nano-watts to hundred micro-watts; and the range of pulse energies are from femto-joule to nano-joule [27].

C. Photo mixing Sources

Photo mixing is the process of generating CW THz radiation using two lasers. As a complementary method for photoconductive generation, photo mixing has outstanding performance in terms of spectral resolution. Moreover, in contrast with photoconductive broadband time-domain THz generation methods, CW systems do not need femtosecond lasers. The outputs of two CW lasers were spatially overlapped and focused onto a biased photoconductive antenna (PCA) with optimized electrode geometry [44]. The frequency of CW THz radiation generated is determined by the frequency difference of the two incoming lasers [45-47]. The emission frequency will be swept in a wide spectral range by detuning one of the lasers. A homodyne detection scheme is used to detect the amplitude and phase of the CW THz radiation coherently [45, 48].

The basic principle of CW THz generation is similar to broadband generation. Two CW lasers with identical polarization and slightly differently frequencies ν_1 and ν_2 are spatially overlapped and then focused on a photoconductive emitter to generate THz wave. The frequency of THz radiation generated is $\nu_{THz} = \nu_1 - \nu_2$. Since those two CW lasers are very stable, this method can be applied in THz spectroscopy and performs better than the others method in terms of the spectral resolution [28].

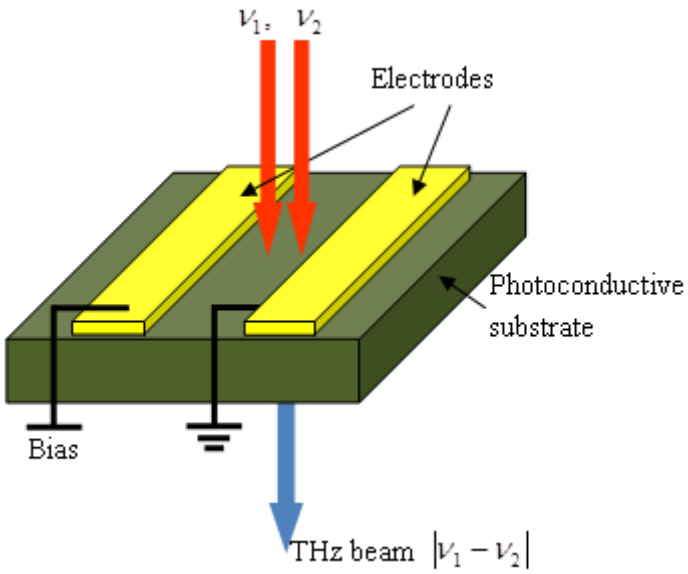

Figure.2.4 Photoconductive antenna emitter for continued THz waves generation.

D. Backward Wave Oscillator (BWO)

Backward Wave Oscillator (BWO) basically uses a vacuum tube to generate THz radiation [49]. An electron beam produced by an electron gun is interacting with the slow wave structure in the backward wave tube. The group velocity of the generated THz radiation is opposite to the motion direction of the electrons. The output THz power from BWOs is moderate (1-100 mw). A system containing a number of BWOs is able to generate a THz radiation with a wide range of frequency. Figure.2.5 shows an example of BWO source that provides electromagnetic radiation at 0.14 THz.

Figure.2.5 A photo of the BWO THz source in our lab.

E. Far Infrared (FIR) Laser

Among all the sources that are developed in THz region, FIR gas laser is relatively old. This kind of laser consists of a long waveguide filled with gaseous organic molecules. Methanol gas is the most widely used one which can provide a powerful emission line (around 100mW) at 118μm [27]. The output range of the line-tunable FIR laser is between 0.3 and 5 THz. The FIR laser techniques have not been developed in recent years due to some ineffectiveness, for example it usually requires helium cooling and is line-tunable only.

F. Quantum Cascade Laser (QCL)

QCL emits in the middle to far infrared regions. It is an efficient THz emission method while limited by the long wavelength of THz radiation. The method requires a large optical module which results in poor coupling between the small gain medium and the optical fields. Moreover, the optical loss is high, due to free electrons in the material [50]. NEST-Pisa and the Cavendish Lab developed the first QCL that operates in the THz region and mentioned the problems above in their design [51]. Their THz QCL emitted at 4.4 THz and provided an average power around 2mW. The operation temperature of the system is around 10K. MIT, University of Leeds, etc. have developed their own QCL based THz systems [52, 53].

G. Free Electron Laser (FEL)

A key feature of FEL is the ultra high power THz emission benefits from its energy recovering linear accelerators [54]. In gas, liquid or solid state lasers, electrons are excited in bound atomic or molecular states while FELs make use of a high velocity bunches of electron beams that propagate through a strong spatially varying magnetic field in vacuum [50]. The electron bunches are oscillated by the magnetic field and emit photons. FEL has a widely tunable frequency range and provides CW or pulse THz waves. FEL systems are limited by the requirements of large space, high cost and dedicated facilities.

2.1.2 THz detectors

In this section, methods for THz detection will be introduced, e.g. photoconductive sampling, free-space electro-optic sampling, thermal detectors, heterodyne detectors, extrinsic germanium detectors, and field-effect transistor (FET) detectors, etc.

A. Photoconductive Sampling

Photoconductive antennas, which have the same structure as the THz photoconductive antenna emitter mentioned in Chapter 2.1.1, are the most popular broadband time-domain (pulsed) THz detection equipment. The difference between them is that the photoconductive antennas used for detection are not biased by any external circuit. In a photoconductive antennas based THz TDS system, the femtosecond laser pulses were split into two parts to drive the emitter and detector antenna respectively. The detected THz pulses provide the electric field needed to drive the photocurrent in the detector. The photocurrent here is a convolution of the electric field from the transient photoconductivity and the antenna [28]. The photocurrent is proportional to the THz field strength only if the transient photoconductivity is much faster than the duration of the THz field. In other words, the photocurrent will be proportional to the temporal integral of the THz field if photoconductivity is not fast enough. Therefore the bandwidth of the detector is determined by the trapping and recombination time of the photo-induced carriers [28].

In order to achieve higher bandwidth, the photoconductive materials must have fast trapping and recombination time. Nowadays, a common way is to use low-temperature-grown (LTG) GaAs which have a few hundred fs carrier lifetimes [55-58]. There are also some other materials with smaller band gaps be applied, e.g. LTG-GaAsSb [59], LTG-InGaAs [60], super lattice structures with LTG-InGaAs/InAlAs [61, 62] and ion-implanted InGaAs [63-65].

B. Free-Space Electro-Optic Sampling

As another popular approach of broadband time-domain (pulsed) THz detection, electro-optic (EO) sampling is a coupling of optical pulse (the laser beam) and THz pulse (low frequency electric field). When both the laser pulse and THz pulse are in the EO crystal the birefringence of the EO crystal which induced by the THz pulse can be quantified by measuring polarization of the laser light. The modulated birefringence of the EO crystal modulates the polarization ellipticity of the optical pulse [50]. After travelling through a λ/4 plate, the beam is split into two orthogonal components by a Wollaston prism and then sent to a balanced photo detector. The difference between the two orthogonal components of the probe pulse which results from ellipticity modulation of the laser pulse will then be used to analyze the phase and amplitude information of the THz pulse. The operating temperature of the EO crystal and the photoconductive detectors are at room temperature. In our THz CS experiment demonstrated later, we applied this EO sampling approach to detect broadband time-domain (pulsed) THz radiation.

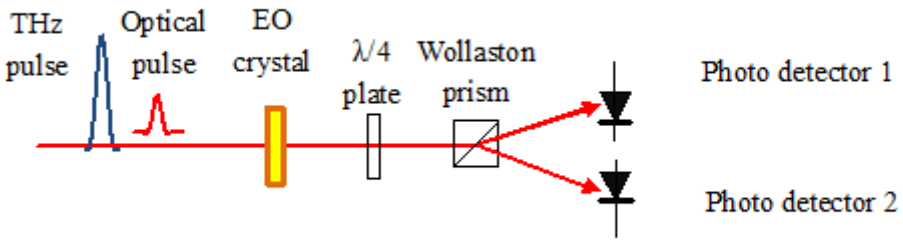

Figure.2.6 EO crystal pulse THz detection setup.

C. Thermal Detectors

Bolometers, Golay cells, and pyro electric detectors are typical thermal detectors used in THz region [66]. These systems all need cooling to reduce high levels of thermal background radiation since the output powers of THz sources are relatively low. In the condition when temperature is as low as 4K or even lower, such approaches can reach NEP (noise equivalent power) around10^{-17} W/Hz$^{1/2}$. The NEP can get to 3×10^{-19} W/Hz$^{1/2}$ by using the hot-electron Titanium Nano bolometers at 0.3K [67]. The

principle of how the thermal detectors operated was introduced in [68]. Some thermal detectors operate at room temperature but the NEP is relatively larger. Figure.2.7 is a photo of a pyro electric detector in our lab.

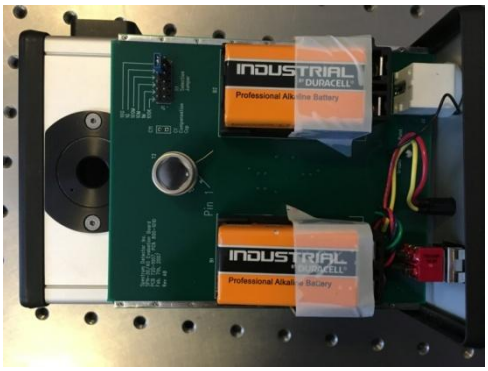

Figure.2.7 A photo of the pyro electric detector used in our lab.

D. Heterodyne Detectors

Heterodyne detectors are used in applications that require high spectral resolution. In such systems, a local oscillator source at the THz frequency is mixed with the THz signal detected. Then the downshifted signal is amplified and analyzed [31]. A Schottky-diode mixer was applied in THz detection at 2.5 THz [69]. Cryogenic cooling can be applied to increase sensitivity in heterodyne detectors. The superconductor-insulator-superconductor tunnel junction mixer is the most widely used mixer [70]. More details of heterodyne detectors are illustrated in [71].

E. Extrinsic Germanium Detectors

The first extrinsic photo detector is the germanium based extrinsic photoconductor detector. There are no suitable shallow dopants for silicon when the wavelengths are longer than 40μm so there are no suitable silicon detectors. More details about extrinsic germanium detectors are shown in [66].

F. Field-Effect transistor (FET) Detectors

FET detectors could be a good solution for resonant and non-resonant THz detection. They can be tuned by easily changing the gate voltage. They can operate at room temperature to achieve a NEP around 10^{-10} W/Hz$^{1/2}$. FET detectors are discussed in detail in [66].

2.1.3 THz time domain spectroscopy (THz-TDS)

Experimental Setup

THz-TDS is an efficient way to study the optical properties of a material in far infrared region [28, 90-94]. Photoconduction and optical rectification are most popular solutions for THz generation in THz TDS systems; and photoconductive sampling and free-space EO sampling are used for THz detection respectively. The THz-TDS system later used in our experiment, which is a typical transmission THz-TDS setup, is showed in Figure.2.8. The system used a photoconductive emitter and an EO crystal detector. The emitter and detector were pumped by a Ti:sapphire ultra short (femtosecond) laser. For the emitter part, the optical pulse is focused on a biased PCA (photoconductive antenna). The THz pulse generated from the PCA is collimated by a set of parabolic mirrors and then focused onto the EO crystal with the other part of the optical pulse. Apart from this method, reflection and attenuated total reflection (ATR) THz-TDS systems are also well developed in spectroscopy applications [77-85].

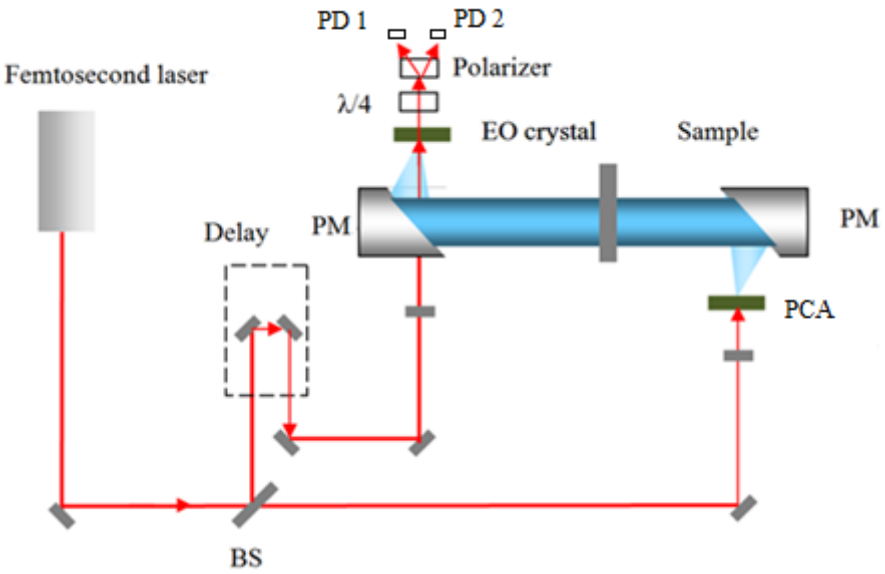

Figure.2.8 A transmission THz-TDS system using a photoconductive antenna as emitter and an EO crystal as detector. (PM: parabolic mirror, BS: beam splitter, PCA: photoconductive antenna, PD: photo diode, and EO: electro-optic).

Data Analysis

The first transmission THz-TDS experiment on water vapor was proposed in 1989 [24]. As a further research, the absorption coefficient and refraction index of a range of dielectrics and semiconductors were showed in [86]. Nowadays, most of THz spectroscopy experiments are performed using transmission THz-TDS systems.

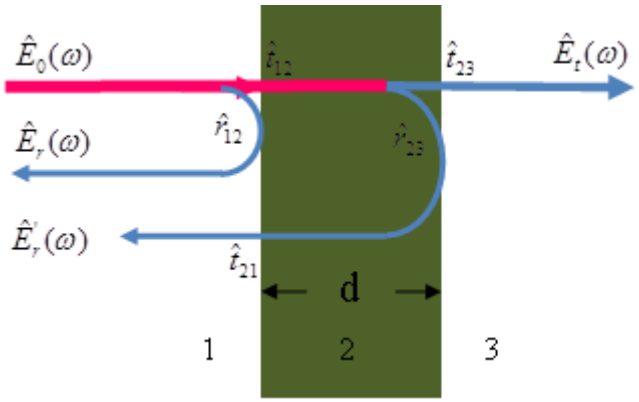

Figure.2.9 Schematic diagram of the THz fields demonstrating a sample in transmission and reflection THz spectroscopy. $\hat{E}_0(\omega)$ is the incident field, $\hat{E}_t(\omega)$ is the transmitted field, $\hat{E}_r(\omega)$ and $\hat{E}_r'(\omega)$ are the reflected fields from front and back interface of the sample. Figure adapted from [28].

Figure.2.9 shows a schematic diagram of the THz fields demonstrating a sample in transmission and reflection THz spectroscopy. The spectral amplitude and phase of the incident THz pulse $\hat{E}_0(\omega)$ is obtained by Fourier Transformation of the measured THz pulse in time domain. Equations below describe the transmitted and reflected signals by considering the sample as uniform [28]:

$$\begin{aligned}\hat{E}_t(\omega) &= \hat{E}_0(\omega)\hat{t}_{12}\hat{t}_{23}e^{-\alpha d/2}e^{in\omega d/c},\\ \hat{E}_r(\omega) &= \hat{E}_0\hat{r}_{12},\\ \hat{E}_r'(\omega) &= \hat{E}_0\hat{t}_{12}\hat{r}_{23}\hat{t}_{21}e^{-\alpha d/2}e^{in\omega d/c},\end{aligned} \tag{2.1}$$

where $\hat{t}_{12}$, $\hat{t}_{23}$, $\hat{r}_{12}$, and $\hat{r}_{23}$ are various complex Fresnel field transmission and reflection coefficients. Such transmission and reflection spectroscopy can be used to acquire the complex index of refraction of the sample, $\hat{n}(\omega) = n(\omega) + i\kappa(\omega)$, where $\kappa(\omega)$ is the extinction coefficient which related to the absorption coefficient $\alpha(\omega)$

through $\kappa(\omega) = \alpha(\omega)c/2\omega$. The two THz pulses which are propagate via air and the sample are recorded in transmission THz-TDS. Their spectral amplitudes and phases can be expressed as [28]:

$$\frac{\hat{E}_{sam}(\omega)}{\hat{E}_{ref}(\omega)} = T(\omega)e^{i\varphi(\omega)} = \hat{t}_{12}\hat{t}_{23}e^{-\alpha d/2}e^{i(n-1)\omega d/c}. \tag{2.2}$$

When analyzing samples with low absorption coefficient in normal incidence, the Fresnel transmission coefficients can be considered as real-valued [28]:

$$n(\omega) = 1 + \frac{\varphi(\omega)c}{\omega d}, \tag{2.3}$$

$$\alpha(\omega) = -\frac{2}{d}\ln\left(\frac{(n+1)^2}{4n}T(\omega)\right). \tag{2.4}$$

An example of a typical transmission THz-TDS measurement is shown in Figure.2.10. Part a) shows the THz pulse measured in time domain and part b) shows the frequency domain information obtained from a).

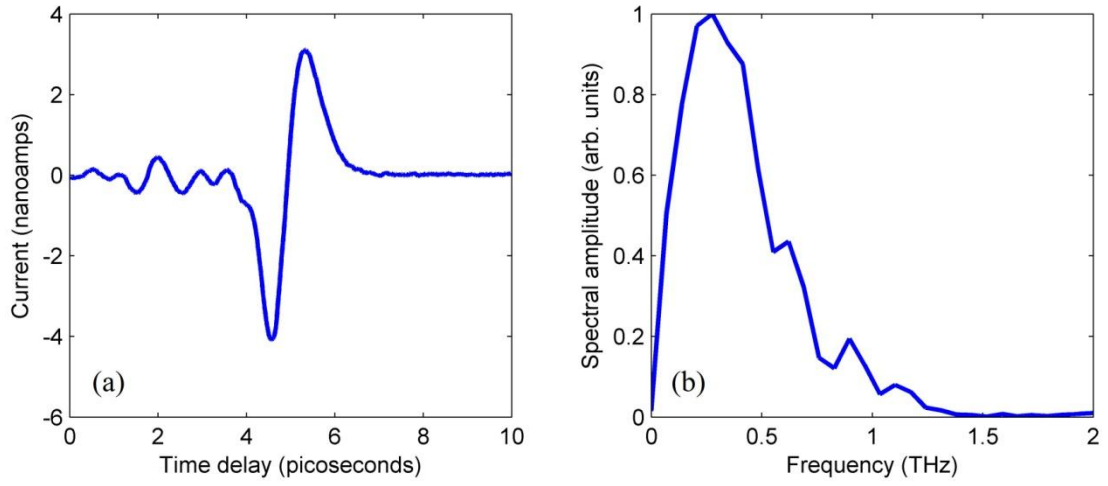

Figure.2.10 A THz pulse recorded in the time domain (a) and its corresponding frequency domain waveform (b).

In the detector the THz pulse provided the electric field to the induced electrons as discussed in Chapter 2.12 A), so the current in part a) of Figure.2.10 is proportional to the amplitude and orientation of THz field. The positive peak is the transmitted THz wave and the negative peak is due to the surface and interface reflection of the sample. The thickness of the sample can be calculated by the time difference between the two main peaks.

In the time domain view, the sequence of signal echoes indicates the multiple reflection and absorption inside the sample. Equations (2.3) and (2.4) are based on the assumption that the sample is non-absorption and have infinite thickness. For thin samples, the multi reflection inside the sample can't be ignored. Duvillaret *et al.* proposed a solution introducing a Fabry-Perot factor $FP(\omega)$ and complex valued Fresnel transmission coefficients [87]. For a sample in air, a general transmission function $\hat{T}(\omega)$ can be expressed as [28, 87]

$$\hat{T}(\omega) = \frac{\hat{E}_{sam}(\omega)}{\hat{E}_{ref}(\omega)} = \frac{4\hat{n}}{(\hat{n}+1)^2} e^{-\alpha d/2} e^{in\omega d/c} FP(\omega), \tag{2.5}$$

Where

$$FP(\omega) = \frac{1}{1-(\frac{\hat{n}-1}{\hat{n}+1})e^{-\alpha d} e^{2in\omega d/c}}. \tag{2.6}$$

The sample thickness and absorption rate of different frequencies can be calculated by considerations of the multi echoes [88]. This method is able to calculate the thickness of samples with moderate absorption.

Comparisons between FTIR and Time-Domain Approach

Fourier transform infrared (FTIR) spectroscopy is well developed and became the standard analytical method in the infrared range since 1950's. A discussion of advantages and disadvantages of the time domain approach comparing to FTIR spectroscopy is showed below.

Firstly, time-domain approach measures the whole transient electric field in a certain time rather than the intensity of the THz radiation. This gives THz spectrum better sensitivity and dynamic range than FTIR method [89]. As a result, high quality THz spectrum can be obtained easily.

Secondly, all TDS systems are using coherent detection technique which avoids most background interference. In coherent detection, the detector is only sensitive to signals which match the phase of the original signal. In TDS systems the detectors are

only sensitive to coherent radiation that is phase-locked to the repetition rate of the femto-second laser. The noise from thermal background radiation can be minimized which enables the system to operate at room temperature. No liquid cryogens cooling system is needed and the whole system is more compact.

Thirdly, the time domain approach can get time domain and frequency domain information of a signal from the same measurement as shown in Figure 2.10. The measured time domain waveform contains amplitude and phase information.
Fourthly, as another benefit, the bandwidth of the radiation is broader than any other source in THz range. In THz-TDS, the broadband coverage can be used for chemical mapping which means that materials are located by their unique THz absorption signatures.

There are some limitations of THz-TDS. The power of the THz beam is very low due to the inefficient non-linear optical mixing. Although the detector is able to filter certain amounts of common noise [90], the operation power is still insufficient. Hence, most of existing THz imaging systems are operated by raster scanning, which scans the beam or the object using a single detector. The image acquisition time is strongly limited in practice.

Some limitations are unavoidable due to the nature of time-domain systems [76]. In a typical Fourier transform spectrometer, the length of the scanned delay line limits the spectral resolution, which means such a system can hardly achieve high resolution. THz-TDS systems have a good performance below 1 THz, but not so good compared to a quantum cascade laser operating at higher THz range [27]. The femtosecond laser used as pump source is expensive.

Recognizing the advantages and limitations mentioned above, transmission/reflection/ATR THz-TDS have respective benefits: transmission configuration provides reliable and quantitative THz spectra; reflection configuration helps research of opaque samples; and ATR configuration is good for rapid screening of samples.

2.1.4 THz time domain (pulsed) imaging (TPI)

Since the first TDS imaging system was reported in 1995 [4, 25], most of the THz imaging is based on THz-TDS, so called THz time-domain (pulsed) imaging (TPI). Such imaging systems have all the above advantages of time-domain approach. Here this technique will be briefly discussed including its imaging modes, experimental setup and data analysis.

Experimental Methods (Transmission/Reflection TPI)

The experimental setup of a transmission TPI system is similar to the THz TDS system showed before in Figure. 2.8. The THz emitter and detector were pumped by a Ti:sapphire ultra short (femto-second) laser. For the emitter part, the optical pulse is focused on a biased PCA (photoconductive antenna). The THz pulse generated from the PCA is collimated by a set of parabolic mirrors and then focused onto the EO crystal with the other part of the optical pulse.

A time delay scan measurement is taken on every point of the sample in TPI imaging process. For each point, 3D information is provided by the imaging system: vertical, horizontal and the time-delay (depth) of the sample. Different images contain different information of the sample which can be reconstructed using the time delay waveform. Each image can be recovered using different position of the sample pixel by pixel. For example, the peak-to-peak amplitude of the time delay waveform shows THz absorption rate of each point; the phase of the waveform shows the thickness of each point.

Most TPI experiments were performed using transmission approach in the early researches [4, 25]. The strong absorption of the samples limits the penetration depth to only few hundred microns. As a result, reflection TPI is more suitable for some THz imaging applications since it allows not only opaque sample but also the use of time-of-flight capabilities of the technique [30, 91]. The thickness of a sample can be obtained by measuring the time difference of THz pulses reflected from the surface and the internal structures of the sample. This is much better than the near IR method

[91, 92]. Thickness information of every layer in a multi-layered sample can be obtained using this method. A diagram of a reflection TPI system is illustrated in Figure.2.11.

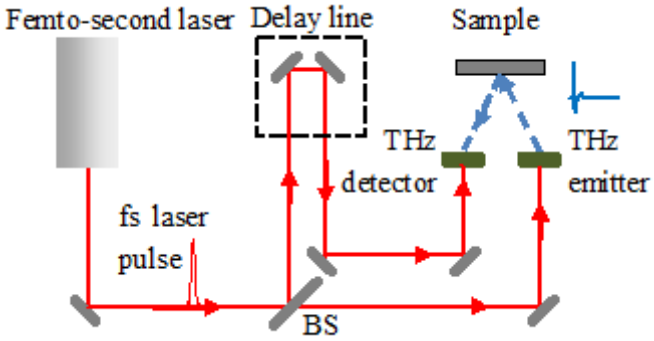

Figure.2.11 A reflection THz pulsed imaging system. (BS: beam splitter, fs: femto second).

Data Analysis

A multi-layer structure is showed in Figure.2.12. Assume that the incident THz radiation is *p*-polarized and the *M*-layered medium is uniform in the transverse. Firstly, Fourier transforms the incident THz pulse into frequency domain. The coefficients of transmission and reflection can be obtained at every single frequency using the 1-D model [93]. Then reflection coefficients are inverse Fourier transformed back to time domain as a THz waveform. The magnetic field of the THz radiation with *z*-component (1D) is expressed as [81, 93],

$$H_z^{(i)}(x,y) = A_i \exp(j(\beta_0 x - \beta_i y)) + B_i \exp(j(\beta_0 x + \beta_i y)) \quad (i = 1, 2, ..., M), \qquad (2.7)$$

Where

$$\beta_0 = \sqrt{\varepsilon_1(\nu)} k_0 \sin\theta$$

$$\beta_i = \sqrt{\varepsilon_i(\nu) k_0^2 - \beta_0^2} \quad (i = 1, 2, ..., M) \qquad (2.8)$$

k_0 is the wave vector in vacuum; θ is the incidence angle; and $\varepsilon_i(\nu)$ is the dielectric function in the *i*th layer of the sample. The *x*-component of the electric field can be obtained by Maxwell's equation [81, 93],

$$E_x^{(i)}(x,y) = \frac{1}{j\omega\varepsilon_i(\nu)} \frac{\partial[H_z^i(x,y)]}{\partial y}. \qquad (2.9)$$

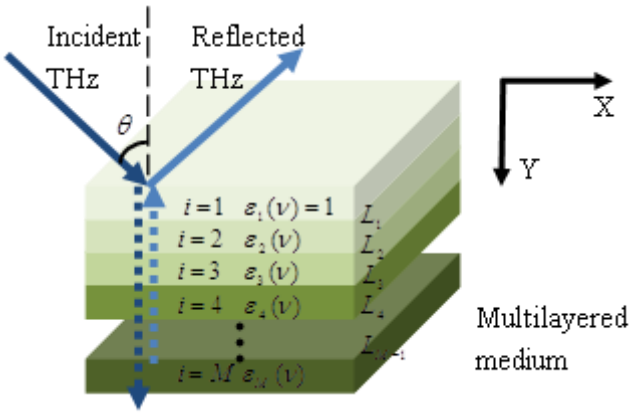

Figure.2.12 A 1D model showed how THz propagate through a multilayered material.

Because of the continuity of $H_z^{(i)}(x,y)$ and $E_x^{(i)}(x,y)$ at the boundary $y=L_i$, the boundary conditions are [93],

$$H_z^{(i)}(x,L_i)=H_z^{(i+1)}(x,L_i)$$

$$E_x^{(i)}(x,L_i)=E_x^{(i+1)}(x,L_i)\quad (i=1,2,...,M-1). \tag{2.10}$$

Hence, the iterative formula is obtained [93],

$$A_i=\frac{\exp(j\beta_i L_i)}{2}[A_{i+1}(1+\tau_i)\exp(-j\beta_{i+1}L_i)+B_{i+1}(1-\tau_i)\exp(j\beta_{i+1}L_i)]$$
$$B_i=\frac{\exp(j\beta_i L_i)}{2}[A_{i+1}(1-\tau_i)\exp(-j\beta_{i+1}L_i)+B_{i+1}(1+\tau_i)\exp(j\beta_{i+1}L_i)] \tag{2.11}$$

Where $\tau_i=\varepsilon_i\beta_{i+1}/\varepsilon_{i+1}\beta_i$. Assume that $A_M=1$ and $B_M=0$, A_1 and B_1 can be calculated by iterating equation (2.9).The reflection coefficient can be written as $|B_1/A_1|$. The transmission coefficient can be written as $|A_M/A_1|$. The absorptance coefficient can be written as $1-|B_1/A_1|-|A_M/A_1|$. Note that, in the case of *s*-polarized incident THz, we can use the similar way for analysis, but $\tau_i^{\cdot}=\beta_{i+1}/\beta_i$ will be used to replace τ_i [93].

The complex dielectric function in the *i*th layer of the sample is expressed by using a Lorentz model with *K*-oscillators [81],

$$\varepsilon_i(\nu)=[n_i(\nu)+j\frac{\alpha(\nu)c}{4\pi\nu}]^2$$
$$=\sum_{k=1}^{K}\frac{S_k^{(i)}(\nu_k^{(i)})^2}{(\nu_k^{(i)})^2-\nu^2-j\nu\Gamma_k^{(i)}}+[n_0^{(i)}-j(C_1^{(i)}+C_2^{(i)}\nu+C_3^{(i)}\nu^2+C_4^{(i)}\nu^3)]^2 \tag{2.12}$$

where $\nu_n^{(i)}$, $\Gamma_n^{(i)}$, and $S_n^{(i)}$ are the center frequency, width, and strength of the *k*th oscillator (*k*=1, 2, ..., *K*) for the *i*th layer (*i*=1, 2, ..., *M*). The real part of this equation is the refractive index and the imaginary part is an empirical expression for the extinction coefficient. Such an oscillator introduces the spectral feature of a sample in terms of refractive index and extinction coefficient. The THz waveform reflected from a multi-layer sample under normal incident condition can be expressed as [81]:

$$R(\nu) = \frac{B_1(\nu)}{A_1(\nu)} \equiv r_1(\nu) + \frac{[1-r_1(\nu)][1+r_1(\nu)]r_2(\nu)\exp(-j2\beta_2(\nu)D)}{1+r_1(\nu)r_2(\nu)\exp(-j2\beta_2(\nu)D)} \qquad (2.13)$$

Where *D* is the coating thickness, and

$$r_1(\nu) = \frac{1-\tau_1(\nu)}{1+\tau_1(\nu)} = \frac{\sqrt{\varepsilon_2(\nu)}-\sqrt{\varepsilon_1(\nu)}}{\sqrt{\varepsilon_2(\nu)}+\sqrt{\varepsilon_1(\nu)}}$$

$$r_2(\nu) = \frac{1-\tau_2(\nu)}{1+\tau_2(\nu)} = \frac{\sqrt{\varepsilon_3(\nu)}-\sqrt{\varepsilon_2(\nu)}}{\sqrt{\varepsilon_3(\nu)}+\sqrt{\varepsilon_2(\nu)}}. \qquad (2.14)$$

To express the physical meaning better, the equation (2.13) is rewrite using Taylor expansion as [81]:

$$R = r_1 + (1-r_1^2)r_2[\exp(-j2\beta_2 D) - r_1 r_2 \exp(-j4\beta_2 D) + r_1^2 r_2^2 \exp(-j6\beta_2 D) - ...]. \qquad (2.15)$$

r_1 is the THz reflection on the surface and the rest of the equation is the multiple reflection of the sample. The first item in the bracket corresponds to the "fundamental" reflection and the rest of items correspond to the "parasitic" reflection [81]. Due to the phase difference, all the reflections are separated after transfer back to time domain. The "fundamental" reflection is normally much stronger than the "parasitic" reflection unless the refractive index changed sharply at the interface. As a result, "parasitic" reflection can be used as an identification reference to determine air gap within the multiple layered medium.

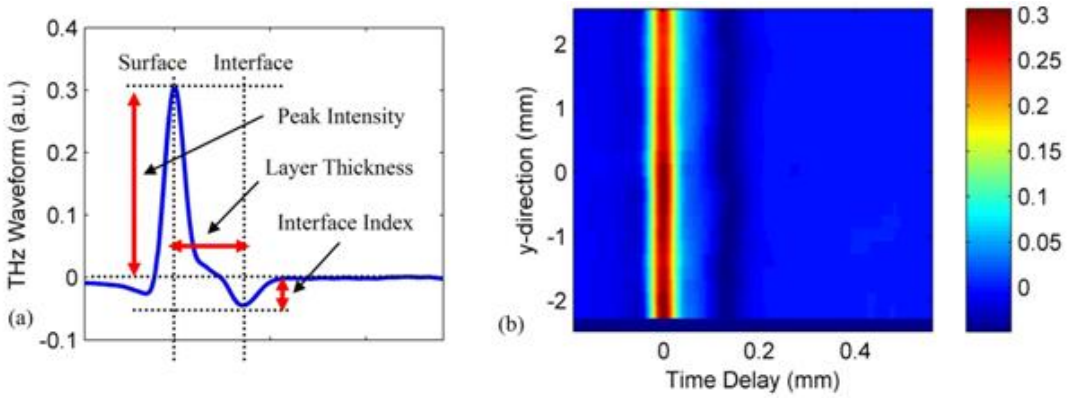

Figure.2.13 A typical time domain THz waveform measured for a one-layer sample (a) and its B-scan model (b).

The time domain THz waveform obtained from a single layer sample and the corresponding B scan image are showed in Figure.2.13. It's easy to identify the peak intensity which indicates the refractive index of the surface as shown in part a) of the figure. The interface index which gives a measure of the strength of reflection from the interface can also be obtained. The layer thickness can be calculated according to the distance between these two peaks, the surface reflection and the interface reflection. More details about the reflection TPI, such as the discussion about the oscillation-like features caused by resonance absorption, etc., were discussed in [81]. Part b) of Figure 2.13 shows the B-scan of the single layer sample. It is clear to see the surface in red and the interface in dark blue. By performing raster scanning for the sample, a complete image can be built up.

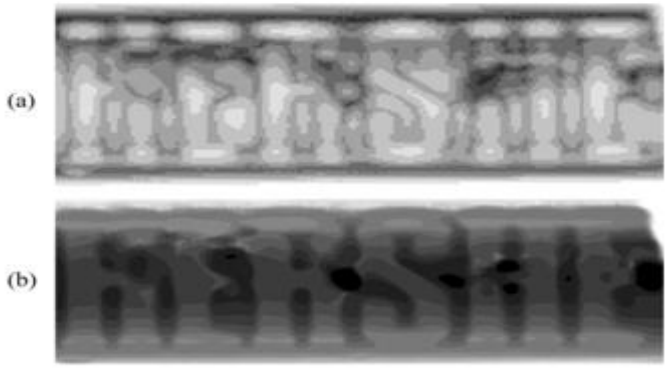

Figure.2.14 THz images obtained by using amplitude of the transmitted time domain pulse transmitted through a chocolate bar (a) and THz image obtained by using transit time of the THz pulse through the sample (b). Figure adapted from [95].

As mentioned above, the data obtained from a TPI system is 3D: the vertical and horizontal dimension of the sample, and the time delay (depth) dimension. In order to obtain a full 2D image, a different view of the time delay date can be applied. Part (a) of Figure.2.14 shows the image which is obtained by using the amplitude of the time domain THz pulses. In this image, it can be seen that the middle is thicker than top and bottom because of the Plano-convex structure. In addition, the embossed letters are visible but not clear enough because the scattering effects of the sample. Part (b) of Figure.2.14 shows the image obtained using the transit time of the THz pulse through the sample. The thicker part of the sample will cause more delay to the THz pulse, so by using this method an image containing thickness information can be obtained. Consequently, as the embossed letters are thicker than other parts of the sample, it is easier to distinguish them from the each other. The output power of the femtosecond laser is a primary source of noise in a TPI system. The noise affect more on amplitude of the THz pulsed than the phase. As a result, images obtained from time delay of the pulse provide better quality. More details of transmission TPI system are shown in [95].

Raster scanning the image pixel by pixel is a widely used method for TPI systems. Apart from that, there are still a lot of promising approaches, e.g. CW THz systems, chirped-pulse technique, THz tomography and interferometric imaging, electro-optic sensing using crossed polarizer and CCD cameras, and a parallel method with the time-domain techniques, are well discussed in [8-12, 96-98].

2.1.5 Applications of THz imaging

By making use of special properties of THz radiation, many applications of THz imaging have been developed. The first THz TDS image was reported in 1995 [4] and the first CW THz image was obtained in 2001 [99]. After that THz imaging has been applied to areas of security screening [6, 100-103], plastic industry [104-108], pharmaceutical industry [30, 81, 109-113], and art conservation [114-118].

A. Security Screening

In the area of security checking, the nondestructive property of THz systems can be taken in to account, e.g. body inspection, mail and luggage scanning, and hand-help optoelectronic THz systems [6, 100-103]. In public utilities such as airport security checking points, THz body inspection can be applied which operates at a few tens of GHz [28]. Strictly speaking these systems are not in THz range.

THz systems have been developed in detection of explosives or illicit drugs in containers such as parcels, envelopes or suitcases, by making use of their sharp spectral features in the THz range and the capability of THz radiation to propagate through non-metal materials. The THz spectrums of RDX based bulk explosives have been well studied so it's quite easy to identify them [100, 101] however the liquid explosives still need to be studied. Picometrix has proposed a QA-1000 THz imaging system for transmission imaging and the THz images the system obtained is showed in Figure.2.15 [103]. A knife, a gun and a bottle in that suitcase were clearly shown. The system takes 100 minutes to complete a scan for an area of $1m^2$. In consideration of imaging time and the popular aluminum suitcases which THz radiation can't propagate through, THz imaging is only suitable to be a supplement to X-ray techniques in security check but can hardly replace them.

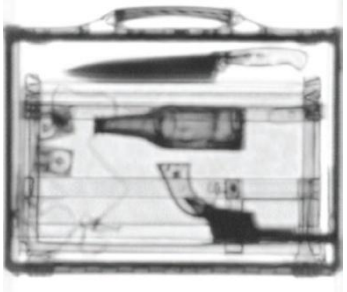

Figure.2.15 An image captured using QA-1000 THz imaging system. Figure adapted from [91].

B. Plastic Industry

THz systems have plenty of applications in plastic industry such as online monitoring of polymeric compounding process, quality control of plastic weld joints and fiber orientation [104-108].

The determination of additive content in polymeric compounds with THz-TDS is a

popular application [104]. Polymeric compounds are mixtures between polymeric based materials and various additives. These substances are essential in order to improve the properties of standard polymers for different applications. In plastic industry, the precise composition of material is a kernel factor.

THz-TDS can be used to identify different additive-polymer combinations with different additive substances [104].Standard polymers are transparent at low THz frequencies; additives affect the THz properties when processed into compounds. The additive content can be calculated from the THz refractive index. As a result, THz-TDS is used in quality control by detecting the refractive index of compound.

C. Pharmaceutical Industry

In the pharmaceutical industry, the release kinetics of the active pharmaceutical ingredient (API) is determined by the coating thickness and the inner structures of the solid dosages forms. The desired dose delivery and bioavailability can be affected if the coating is non-uniform or has any defects [81]. It's important to measure the coating thickness precisely and map the inner structures nondestructively.

THz waves can transmit through most of the pharmaceutical materials and many recipients and ingredients have typical spectral features in the THz range. Therefore THz systems have great potential in the pharmaceutical industry and some were recently proposed by Teraview [109-113].

D. Art Conservation

Paintings and murals are valuable cultural heritage which normally have many layers as they were covered and repainted in different time. Each layer represents an artwork of that era. Some nondestructive approaches are used for image detection but have limitations such as resolution and penetration depth. Thus THz systems were developed in art conservation as another potential method [114-118].

To sum up, many THz applications have been discussed. Applications in nondestructive detection and inspection using THz system were developed. The data

acquisition rate is a key factor to be considered. There is always a tradeoff between data acquisition rate and the quality of the data obtained in a THz imaging system. Technically, it cannot have both high scan rates and long scan range. A long scan range can provide better spectral resolution but will results in a slow imaging speed. The resolution will be restricted by a short scan range, and so as the depth of penetration of THz radiation on a sample. The relatively slow imaging speed and the high cost of the hardware implementation need to be improved to meet any commercial requirements.

2.2. Compressed sensing

Over the past few years, compressed/compressive sensing/sampling (CS) has been well developed in the research area of applied mathematics, electrical engineering, and computer science because it can outstrip the limits of traditional sampling theory. Based on CS theory, sparse signals can be represented using only a few non-zero coefficients in a proper dictionary or basis. Then the signal can be recovered from very few experimental measurements using non-linear optimizations and algorithms. The concept was introduced by Candès, Romberg, Tao and Donoho in 2006 [13, 14, and 119]. Research in the area has grown rapidly over these years and thousands of papers have been published, including some excellent tutorials and review articles [120-128]. More references and software are listed on the website from Rice University [129].

In this section, we reviewed the basic theory underlying CS. Following a brief introduction and background of CS, we begin with a discussion of the sparse signal model. After that, alternative constructions for structured CS matrices have been reviewed. Then we focused on the theory and algorithms for sparse recovery. By the end some of the sparse recovery framework's extension is discussed.

2.2.1 Background of CS: From Shannon-Nyquist Theorem to Compressed sensing

Analog to digital conversion (ADC) plays a fundamental role in the digital world nowadays. The analog-to-digital converters (ADC) translate the analog signal into a stream of digital numbers. The analog signal is sensed discontinuously according to some rate and this discontinued data is processed to digital data. Since the measurements are spaced in time, only the prior structures of the signal can be recovered. After this discontinuous sampling, lots of data from the detector are supposed be transferred to the ADC and then processed. As a result, the ADC needs a large storage space and a powerful processer. The processer can compress the data to digital by removing the useless part of data obtained from the detector before. The data removed is a total waste of measurement time, communication time, storage space and processing time. CS can solve these problems by combining compression and sampling, i.e., directly measure the effective part that won't be removed in the compression process [13].

A. Shannon-Nyquist Theorem

According to Shannon-Nyquist theorem, a band limited signal with maximum frequency B can be reconstructed from equal spaced discrete samples at a minimum sampling rate of 2B [130, 131]. By assuming an analog signal is band limited (have limited time variation), it can be represented by a discrete samples at a proper sampling rate.

Shannon-Nyquist theorem can be defined as following: If no frequencies in a time varying function $x(t)$ are higher than B, the function can be completely represented by a series of $1/(2B)$ seconds spaced ordinates [131]. Shannon-Nyquist theory shows a clear relation between $x(t)$ and its samples $x(nT)$, where n must be more than 2B. This enables the continuous signal to be transferred to a discrete signal.

Many Digital Signal Processing (DSP) device works based on Shannon-Nyquist theorem for both detecting and estimating the analog signals. The signal acquisition

devices have been developed so rapidly in the last half century that the amount of data processed challenges the DSP unit a lot. It becomes difficult to sample a signal at twice of its maximum frequency. Processing structured analog signals can be more effective than using the Shannon-Nyquist theorem. However the reconstruction part requires knowing the structure of the signals which are not suitable in most practice applications. So finding a method to recover the unknown structured models at sampling rate much lower than Shannon-Nyquist sampling rate is needed.

B. Compressed Sensing

The concept of Compressed Sensing was first showed by Candès, Romberg, Tao and Donoho: a signal can be reconstructed using sparse representation from a small set of linear measurements [13, 14, 119, and 121]. An advantage of CS is to sense sparse signals by reducing the sampling rate and storage of acquisition devices.

CS theory provides a mathematical algorithm for sensing and compressing vectors with finite dimensional simultaneously. In CS a signal $x_{N\times 1}$ can be acquired from M ($M << N$) linear measurements $y_{M\times 1} = \Phi_{M\times N} x_{N\times 1}$ using a $M \times N$ CS sampling matrix Φ. If the sample matrix Φ is well-chosen (satisfies with some properties and conditions which will be discussed below) and a degree of reconstruction error is allowed, the number of *M* can be much smaller than *N*.

There are three major differences between CS and conventional recovery methods: First, classical sampling theory considers continuous-time signals with infinite length. However, CS is focused on measuring finite-dimensional vector. Secondly, based on the knowledge of modern sampling method [132, 133], more general linear measurements are used during the process of CS acquiring signals, rather than using sampling signal at certain time points in time. Thirdly, a linear process is used in Shannon-Nyquist framework to achieve signal recovery. Alternatively, signal recovery is achieved using non-linear method in CS method.

Many practical implementations based on CS have been developed for numerous applications [134-139]. The researches in CS are mainly focused on two areas as follows [127]: The first area is theory and applications in CS sampling operators that are not random matrices and with special structures. The random sampling operators, which are fundamental in conventional CS theory, largely need to be optimized or replaced by more efficient structured sensing operators corresponding to practical applications. The second area consists of signal representations that are not in sparsely structures such as continuous signals with infinite dimensional representations. For many signals, their structure allows them to be compressed more and it's not efficient to describing their complex structure using standard sparsity. Since reducing the sampling rate is one of the primary advantages of CS, it is significant to build theory that is suitable for low dimensional signal in arbitrary Hilbert spaces（important tools in Fourier analysis theory）.

2.2.2 Sparse signal model

Signal processing refers to the processes of acquiring, processing and extracting information from the signals. Generally, signals can be analyzed more efficiently and accurately if they are processed using proper models. Models can help distinguish the interesting part of signals from the uninteresting part directly. In most traditional signal processing methods, signals are treated as vectors within an appropriate vector space. The complex structures in many signals cannot be captured using this simple linear model [126]. To improve against this, sparse signal model, one kind of low dimension models, which has particular geometrical structures has been applied in signal processing. The sparse signal model enables signal information to be obtained via a simple linear and non-adaptive projection to a much lower dimensional space. The projection dimension is also independent of their ambient dimension [140].

A signal can be defined as sparse signal if it can be approximated as linear combinations of a few elements from a designed basis or dictionary. Some signals with high dimension contained little information compared to their ambient dimension. Sparse models can capture these signals efficiently using a mathematical

expression. Sparsity is the most popular signal model and it's been applied in many compression algorithms in CS. Sparsity has been exploited in signal processing applications as diverse as compression, denoising, deconvolution, restoration and inpainting [141-147].

2.2.2.1 Sensing matrices

Given a signal $x \in R^N$, the CS process can be represented using M linear measurements mathematically as

$$y_{M\times 1} = \Phi_{M\times N} x_{N\times 1}, \tag{2.16}$$

Where Φ_{MxN} is a $M \times N$ sensing matrix and $y \in R^M$. Sensing matrix Φ_{MxN} aims to reduce the dimension from R^N to R^M ($M << N$). Actually, the sensing matrix $\Phi_{\mathrm{MxN}=} = \Phi\Psi$, where Φ is the measurement matrix and Ψ is the sparsity basis. In CS process, the sensing matrices are fixed in advance so we assume that the measurements are non-adaptive.

Generally a proper dictionary and basis can be chosen in two ways: the first is the sparsifying dictionary obtained from a mathematical model of the data [148-154]; the second is a dictionary learned from training sets [155-159]. The first way is called predefined transforms, which are well known for fast implicit implementations and analytic formulations. The analytic dictionaries obtained from this way are normally formulated as tight frames, which mean it can be describe by an equation $\Phi\Phi^T x = x$. A representation over the dictionary can be derived from the dictionary using the equation [148]. The dictionary can be ready by analyzing the behavior of the filter-set $\Phi^T x$ and establishing decay rates and error bounds.

The way to design the sensing matrix to ensure the desired information from the signal *x* will be discussed in this section and the method to recover the signal x from the received measurement y will be discussed in the next section.

2.2.2.1.1 Sparsity basis

As discussed, there are several benefits from the tight frame approach [148]: firstly, it is easier to analyze the behavior of $\Phi^T x$ as an analysis operator than to derive sparsity bounds in a synthesis framework. Secondly, the algorithms for both analysis and synthesis operators become reversals which simplifies the algorithm designing. Thirdly, such approach produces a useful structure for both the analysis and synthesis frameworks.

Currently, several typical signal processing methods, such as discrete cosine transform (DCT), wavelets, wavelet packets, curvelets, contourlets, and bandelets, are all proposed to exploit one-dimensional and two-dimensional mathematical models for constructing effective dictionaries for signal and images [149-154]. All nature images can be considered as sparse signal in DCT and wavelets basis so they are especially popular in compressed sensing imaging.

As an example of the sparse models, a typical THz image or a THz waveform can be approximated as a sparse signal under certain dictionary and basis. For now most THz images are quite simple with large smooth regions and relatively small sharp edges. Signals with such structure are approximately sparse under DCT or wavelet transform. A rough scale of the image is provided by the lowest frequency components, while the high frequency components provide the details about the edge information [126]. As most of the coefficients are very small, after setting a threshold to assume these small coefficients to be zero, a good approximation of sparse representation can be obtained. Thus, CS approach has a great potential in THz imaging.

2.2.2.1.2 Measurement matrix

There are some properties the sensing matrix needs to satisfy such as null space property (NSP), restricted isometry property (RIP), and coherence. The NSP (null space property) is enough for establishing guarantees but it’s difficult to show directly and these guarantees don’t work for noise. The RIP is easier to deal with and performs

well with noise. The RIP will be briefly discussed and more details about these three properties and conditions were demonstrated in [126].

The measurement matrix Φ needs to be incoherent with the sparsity basis Ψ to guarantee the accuracy and uniqueness of the sparse vector in equation (2.16). It is known that the RIP holds if the measurement matrix Φ is incoherent with the sparsity basis Ψ. The RIP was first reported as an essential property of CS matrices by Candès, Romberg and Tao [119, 155]. The isometry condition can be mathematically described as following [156]: the restricted isometry constant δ_k of a matrix Φ is the smallest number such that

$$(1-\delta_k)\|x\|_2^2 \le \|\Phi x\|_2^2 \le (1+\delta_k)\|x\|_2^2, \tag{2.17}$$

for all $x \in \sum_k$.

A matrix Φ is said to satisfy the RIP of order *k* if constant $\delta_k \in (0,1)$ exists. By the definition RIP it is assumed that the bounds that are symmetric to approximately 1 for convenience. In practice, it could be extended to be

$$\alpha\|x\|_2^2 \le \|\Phi x\|_2^2 \le \beta\|x\|_2^2, \tag{2.18}$$

where $0 < \alpha < \beta < \infty$. Giving such bounds, we can scale Φ and let it satisfy the symmetric bound about 1 in equation (2.17).

The way to construct matrices that satisfy these properties and conditions is introduced here by taking random matrices as an example. Random matrices are in constructions as sensing matrices. The entries of random $M \times N$ sized matrices Φ are identically distributed and independent. The RIP can be satisfied by the random matrices if the entries are chosen as a Gaussian, Bernoulli, or any sub-Gaussian distribution [155, 156]. These random constructions also make the sensing matrices that satisfy the NSP.

There are several advantages using these random matrices to construct the sensing matrix. Firstly, random matrices are democratic so a signal can be recovered given sufficient measurements [157, 158]. Secondly, the signal *x* in practice is often sparse

to some basis or frame Ψ which means ΦΨ are actually required to satisfy the RIP. Since the random matrices are almost incoherent with any sparse signals, in most of cases, ΦΨ must satisfy the RIP whatever the Ψ is. Thirdly, when dealing with sparse signals, the incoherence property of random matrices require less numbers of measurements than any other matrices.

A number of hardware implementations have been developed to enable random measurements such as random demodulator [159], random filtering [160], the modulated wideband converter [161], random convolution [162], and the compressive multiplexer [163].

However, there are a number of disadvantages. The full random matrix is impractical to build in hardware. Due to its unstructured property, it requires relatively more complicated computations and larger storage space.

There still exists a number of sensing matrices satisfying the RIP such as Toeplitz and circulant matrix, Vandermonde matrix, uniform spherical matrix, random signs matrix, partial Fourier matrix, Partial Hadamard matrix, sparse projection matrix and very sparse projection matrix, and structurally random matrices. More details are discussed in [164-174].

2.2.2.2 Signal recovery algorithms：An optimization problem of ℓ_0 norm

Signal recovery algorithms, which recover the sparse signal $x_{N\times 1}$ from only $M << N$ measurements $y_{M\times 1} = \Phi_{M\times N} x_{N\times 1}$, is a key part in CS theory. The process of recovering the signal *x* can be described as solving an optimization problem of ℓ_0 norm:

$$\hat{x} = \arg\min_{z} \|x\|_0 \quad s.t. \quad z \in B(y), \tag{2.19}$$

Where $B(y)$ ensures that $\hat{x}$ is consistent with the measurements *y*. For noise-free signals, $B(y)$ can be assumed as $B(y) = \{z : \Phi x = y\}$; and for noisy signals, $B(y)$

can be considered as $B(y) = \{z : \|\Phi x - y\|_2 \leq \varepsilon\}$.

Mathematically, ℓ_0 norm means the number of non-zero elements in the vector. Unfortunately, the function $\|.\|_0$ is non-convex and difficult to solve. Solving problem (2.19) is both numerically unstable and non-deterministic polynomial-time (NP) hard. The ℓ_0 norm problem is too complex and almost impossible to solve but so it become an optimization problem: it can't be solved but the number of non-zero elements can be minimized. Detailed enumeration of all possible locations of the nonzero entries C_N^k is required [170].

Currently, there are two ways to solve the ℓ_0 norm optimization: linear solution and non-linear solutions. The minimum mean square error (MMSE) linear estimation is the linear solution. The non-linear solutions include a number of nonlinear algorithmic based on iteration such as ℓ_1 minimization algorithms, greedy algorithms, and total-variation minimization (TV-min) algorithms.

2.2.2.2.1 Linear solution: MMSE Linear Estimation

The minimum mean square error (MMSE) is estimation in a Bayesian setting with quadratic cost function. As discussed, the CS process using *M* linear measurements can be presented mathematically as $y_{M\times 1} = \Phi_{M\times N} x_{N\times 1}$. Reconstructed images can be obtained by the MMSE linear estimation [175, 176]. The reconstruction matrix $\hat{\Phi}_{N\times M}$ according to $\hat{x}_{N\times 1} = \hat{\Phi}_{N\times M} y_{M\times 1}$ can be written as

$$\hat{\Phi} = R_{xx}\Phi^T(\Phi R_{xx}\Phi^T)^{-1}, \tag{2.20}$$

where R_{xx} represents the autocorrelation function of the input signal. For nature images, we approximate R_{xx} using the autoregressive model of order 1 (AR(1) model) with correlation coefficient $\rho = 0.95$. A good reconstructed image can be easily obtained by the MMSE linear estimation if the image is simple. The

reconstruction quality drops if the image is complex and has lots of sharp edges. For the purpose of improving the quality of the reconstructed images by a further level, several nonlinear reconstruction algorithms are discussed as below.

2.2.2.2.2 Non-linear solutions

The non-linear solutions discussed here are ℓ_1 minimization algorithms, greedy algorithms, and total-variation minimization (TV-min) algorithms. All of them are based on iteration algorithm. The basic algorithm of iteration is showed below.

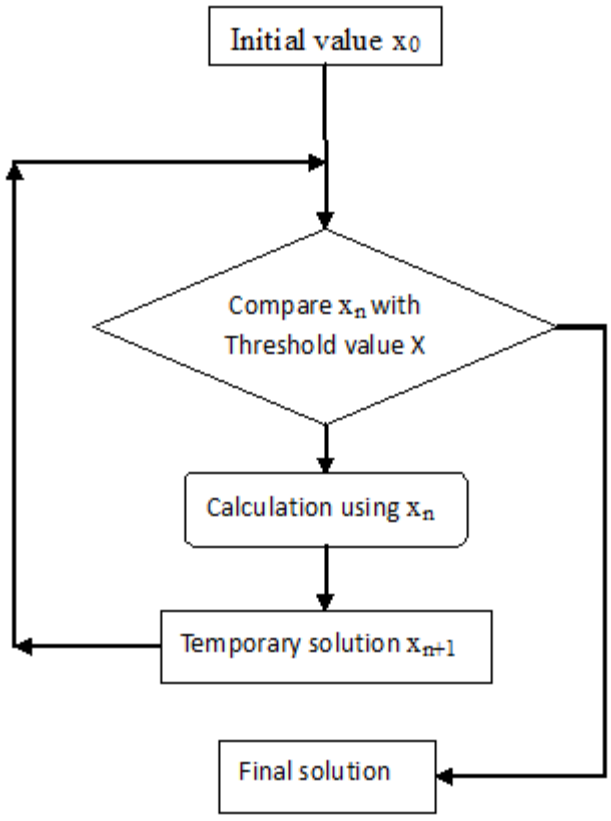

Figure.2.16 Flow chart of a typical iteration procedure when solving the ℓ_0 norm optimization problem. The initial value and the threshold value are experiential estimations

A. l_1 Minimization Algorithms

B. Logan reported the first use of ℓ_1 in relation with sparse frequency estimation in his Ph.D. thesis [177]. Donoho and Logan proposed the earliest theory on recovering

sparse signal using ℓ_1 minimization in 1992. The optimization problem of ℓ_0 norm can be solved more tractable by replacing $\|.\|_0$ with its convex approximation $\|.\|_1$.

$$\hat{x} = \arg\min_z \|x\|_1 \quad s.t. \quad z \in B(y). \tag{2.21}$$

From [149, 178], problem (2.19) has been proved to be equivalent to problem (2.21). The *k*-space signals can be fully recovered from optimization based on the ℓ_1 norm from only $M \geq Ck\log(N/k)$ i.i.d. Gaussian measurements [13, 14].

There exist some other algorithms aiming to solve the problem (2.21) such as interior-point method [179], gradient projection [180] method and homotopy method [181]. Interior-point method provides accurate recovery whereas its computation speed is slow; gradient projection has relatively faster computation speed; and homotopy method is practical for the small scale problems. Furthermore, reweighted ℓ_1 algorithm is proposed to reduce the effect from measurement noise on the reconstruction algorithms [182].

B. Greedy Algorithms

There are many varieties of greedy/iterative methods for computing sparse models [183-191]. Greedy algorithms are based on iterative approximation of the signal coefficients and support. There are two ways to realize the approximation: the first one is to recognize the support of the signal iteratively until it's a convergence criterion; the second one is to acquire a more accurate estimate of the sparse signal at any iteration that not matched to the measured data [126]. Two of the most common greedy methods are Orthogonal Matching Pursuit (OMP) and iterative threshold [126, 192-194].

C. Total-Variation Minimization Algorithms

Total-variation minimization (TV-min) is highly related to ℓ_1 minimization and was first reported by Rudin, Osher and Fatemi in 1990 [195]. The ℓ_1 minimization is

suitable for one-dimensional signal recovery while TV-min has been proved to perform better in recovering two-dimensional images [14]. The optimization of TV norm can be described as:

$$\min \|x\|_{TV} \quad s.t. \quad y = \Phi x, \tag{2.22}$$

where $\|x\|_{TV}$ is the TV norm of a two-dimensional signal x. For discrete data $x(t_1, t_2)$, $0 \le t_1, t_2 \le N-1$,

$$\|x\|_{TV} = \sum_{t_1, t_2} \sqrt{|D_1 x(t_1, t_2)|^2 + |D_2 x(t_1, t_2)|^2}, \tag{2.23}$$

where $D_1 x = x(t_1, t_2) - x(t_1 - 1, t_2)$ and $D_2 x = x(t_1, t_2) - x(t_1, t_2 - 1)$. The TV-min problem then can be recast as special convex programs known as second order cone programs (SOCP's) [14, 196]. By applying TV-min method, two-dimensional images can be reconstructed accurately but with relatively slow computation speed.

The MMSE linear estimation is used in fast compressed imaging as its corresponding computational time is relatively short; and the TV-min nonlinear reconstruction algorithm is used for high quality image reconstruction.

2.2.3 CS imaging applications

There are a wide range of CS imaging applications such as optical single-pixel camera, tomography, digital holography, spectral imaging, geophysical imaging, and medical imaging (including magnetic resonance imaging (MRI)), and photo-acoustic imaging [14, 135, 197-203]. Some of those applications with impressive advantages such as great imaging acquisition efficiency and simply hardware implementation are discussed below.

A. Single-Pixel Camera

As shown in Figure.2.17, the incident light on to the sample is reflected by the sample and then focused onto the digital mirror device (DMD) array. The orientation of each mirror in the DMD array is modulated by a random number generator (RNG). Liner

projections of an image onto pseudorandom binary patterns are achieved using this DMD array. After this optical modulation, the light is focused onto a photodiode detector. Then the data recorded are used for reconstruction [14, 197]. The numbers of measurements needed are much smaller than the number of pixels. It is noted that this system relies on a single-pixel photodiode for detection rather than a CCD or CMOS array which is simpler and cheaper.

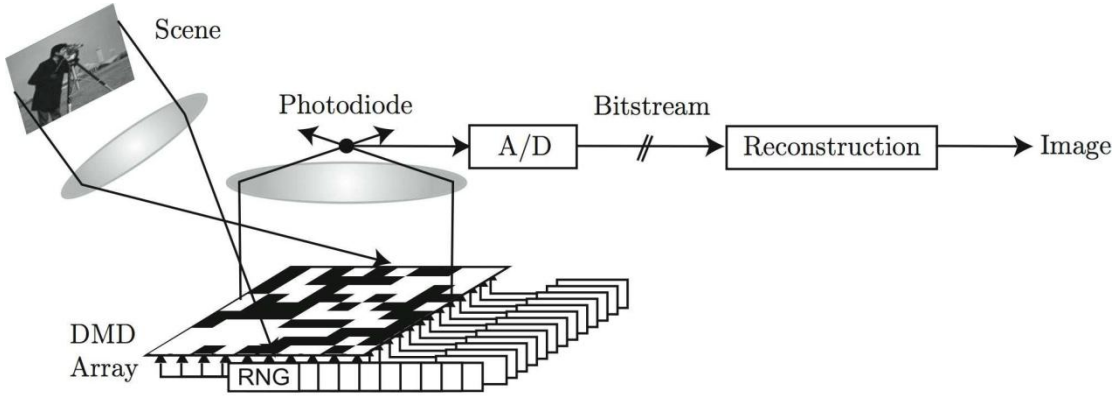

Figure.2.17 Single-pixel camera. Figure adapted from [197] (DMD: digital mirror device. A/D: analogue to digital.

B. Digital Holography

Digital holography is an computational imaging process using holograms recorded by electronic detector arrays [198]. Since 3D estimation from the data is underdetermined, traditional digital holography cannot be regard as 3D tomographic method. Using the CS approach, the 3D tomography can be obtained from a single 2D monochromatic digital holography. The results and more details were presented in [198].

C. Spectral Imaging

The spectral nature of the materials can be obtained using a variety of applications based on spectral imaging. Conventional spectral imaging is slow due to the tradeoffs among spatial resolution, spectral resolution and measurement speed. A novel single-shot compressive spectral imaging system based on the concept of CS was developed to eliminate these tradeoffs [199]. The key feature of the system is two dispersive elements located in opposition and surrounding a binary-valued aperture

code. Spatially varying, easily controllable, spectral filter functions with narrow features can be achieved by such structure [199].

D. Magnetic Resonance Imaging (MRI)

Imaging speed in many MRI applications is mainly limited by physical (gradient amplitude and slew-rate) and physiological (nerve stimulation) constraints [202]. Many CS based implementations are developed for rapid MRI aiming to exploit the sparsity in MR images. Some CS based implementations for 2D and 3D Cartesian imaging showed that the sparsity of MR images can be exploited to significantly reduce scan time or improve the spatial resolution. More details about the experimental implementations and corresponding results were proposed in [202].

Chapter 3

Fast experimental validation for CS imaging sampling operator design

3.1. Criteria of sampling operators (masks) design

Most terahertz pulsed imaging experiments were implemented by raster scanning. This approach either scanned the focused THz beam or the sample and then the THz beam was collected by a single point detector. Due to the slow scan speed, an imaging process could take minutes or even hours, depending on the number of pixels required. For example, normally it took 6 minutes to scan a 4×4 pixels image [204].

A typical THz image or waveform can be approximated as a sparse signal so CS imaging can be applied. CS imaging can dramatically decreases the measurement time as compared with the conventional raster scanning method, since fewer signal samples are required to reconstruct an image [218]. The single pixel camera introduced in Chapter 2.2.3 can be adapted to work in THz range. Thus, a THz single pixel camera system can be built based on the concept of CS as showed in Figure.3.1. The THz beam was modulated to parallel wave before travelling through the masks and sample. The THz linear projections of the sample and masks were recorded for reconstruction. Compared with conventional THz imaging systems, no raster scanning of the sample or THz beam was needed.

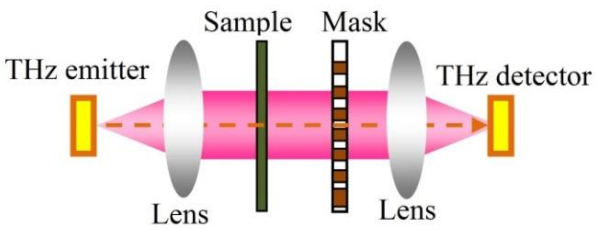

Figure.3.1 THz single pixel camera system. The THz beam was collimated by a focus lens onto the detector after travelling through the sample and masks. The linear projections of the sample and mask patterns were recorded and used for reconstruction procedure.

Almost all the CS THz configurations were adapted from the single pixel camera. In practical applications, there were more lenses than showed in Figure.3.1 to collimated THz beam better (transmit through sample or reflect from sample). The core technique was to reconstruct the original sample from THz projections of the sample and masks. The masks were a key factor in a CS THz imaging system to control the imaging quality and imaging speed. Mathematical model of a CS imaging process (including the measurement process and reconstruction process) is showed in the flowchart below.

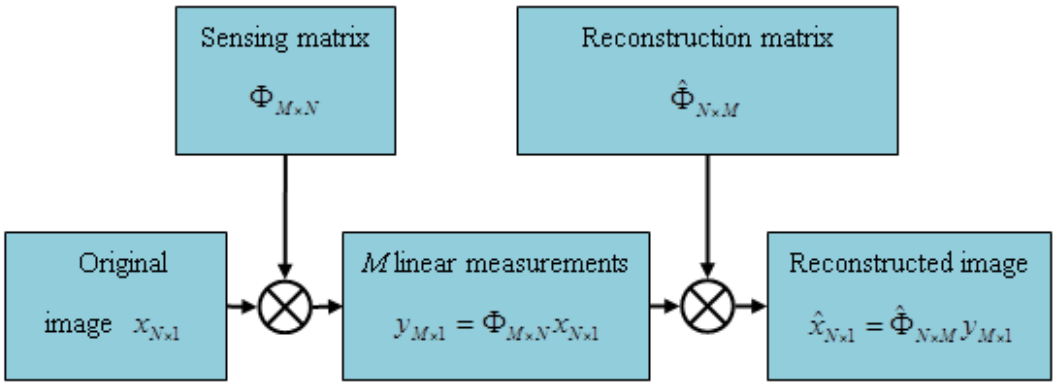

Figure.3.2 Flowchart diagram of CS imaging procedure.

Researches on CS masks, especially those which are not random matrixes are the major area of CS research. Designed sampling operators in CS imaging are more efficient corresponding to practical applications. Let x represent vector version of an image with N pixels. Suppose that x has a K-sparse representation $\hat{x}$ under a sparsity basisΨ (e.g. the discrete cosine transform or the wavelet). The CS sampling process can be described as [13, 119]

$$y = \Phi x = \Phi\Psi\hat{x}$$

where y is the $M \times 1$measured signal vector , Φ is an $M \times N$ ($M \ll N$) sensing matrix. The original signal x then can be obtained by solving the following equations:

$$\min_{\hat{x}} \|\hat{x}\|_0 \quad \text{s.t. } A\hat{x} = y$$

Satisfying $x = \Psi\hat{x}$, where, $A = \Phi\Psi$.

The sensing matrices should match with some properties such as null space property (NSP) and restricted isometry property (RIP). It is known that the RIP holds if the

measurement matrix Φ is incoherent with the sparsity basisΨ [155, 156]. There are some popular sensing matrix such as Toeplitz and circulant matrix, Vandermonde matrix, uniform spherical matrix, random signs matrix, partial Fourier matrix, Partial Hadamard matrix, sparse projection matrix and structurally random matrices [205-215].

The masks need to be fabricated physically so not all those sensing matrix satisfying RIP are suitable for CS THz imaging. The masks need to be designed to meet practical requirements for CS THz imaging. Some of the main design criteria of masks are as following:

- Imaging quality
- Sampling rate
- Resolution
- Implementation complexity
- Imaging speed

The masks designed based on those fundamental requirements need to be validated by simulation and physical experiments. The single pixel camera set up was too slow for mask designing validation since all the masks need to be fabricated physically before testing. To make the designing process more efficient, the time consuming fabrication of physical masks should be avoidable during the designing process. A fast experimental validation system which can provide fast feedbacks for mask designing is highly needed.

3.2. Demonstrations of sampling operator (masks) design criteria by using on screen based CS imaging set up

3.2.1 Experimental set up

A schematic diagram of the on-screen compressive imaging system is showed in Figure.3.3. A computer monitor was used as the light source and a photo diode was used as the detector. The light from the screen was focused by a set of lenses onto the detector and the intensity of the light was measured. The images shown on the screen simulated the linear projection of sample and masks. The system can be considered as an adaption from single pixel camera. The size of the imaging window on the screen was 512 by 512 pixels and the lens set was about 0.5 meter away from the screen.

In real word CS systems, the linear measurements $y_{M\times1}$, i.e., linear projections of an image and masks should be measured using detectors. In simulation experiments, the linear projections can be obtained by multiplying the original image $x_{N\times1}$ and sensing matrix Φ. The on screen system utilized these simulated linear projections as light source, which presented on the screen. This system can be considered as half physical and half simulation.

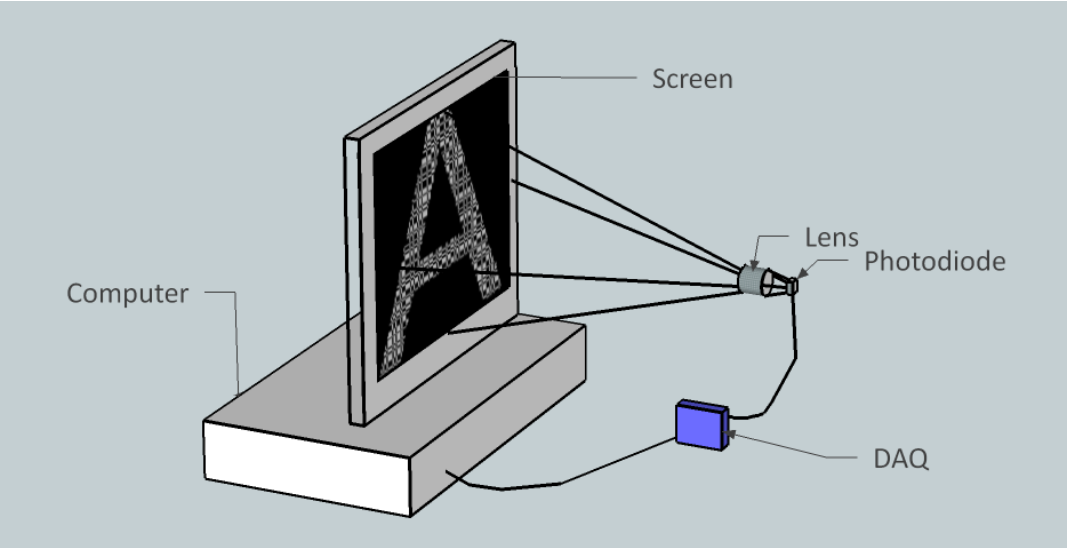

Figure.3.3 On-screen compressive imaging system.

In the on screen based CS system, there were no physical masks or samples. There was no need to fabricate the masks physically, which was time and cost effective. During conventional CS imaging process, the masks need to be changed from one to another for every single measurement. While in the on screen CS system, there was no limitation on speed of changing the masks since there were no physical masks. The limitation on speed of changing masks is the refresh rate of the screen and the response time of the photodiode. In practice, it took 0.1 second for the system to be stabilized during each measurement.

3.2.2 Random Bernoulli masks: sampling rate, resolution and image quality

The entries of Random Bernoulli matrices are 0 and 1 with equal probabilities. They have been well proofed in research of compressive sensing since they are almost incoherent with any sparse signal, which means that they always satisfy RIP. In an optical CS imaging system, 0 and 1 represent check-boards which are either transparent or block the light. In this case, only 50% of light from a light source could transmit through samples.

Image quality VS sampling rate

A group of measurements have been done using random masks to study the relation between sampling rate and the quality of reconstructed images. The original pattern ‘O’ and images reconstructed according to sampling rates of 5%, 10%, 15% and 20% respectively are shown in Figure.3.4. The resolution of these images was 40 by 40 pixels so the sampling rates of 5%, 10%, 15% and 20% equal to numbers of measurements 80, 160, 240 and 320 respectively.

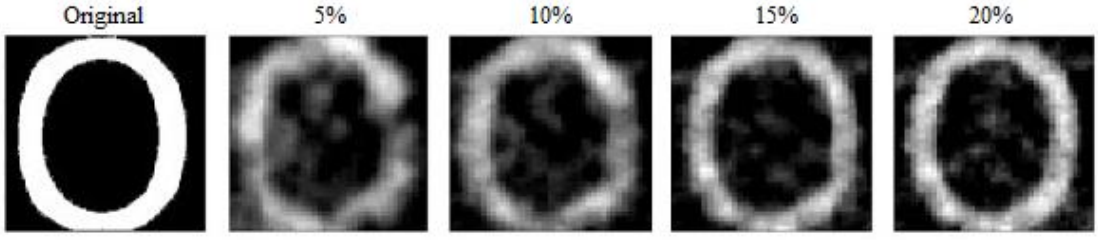

Figure.3.4 Images reconstructed according to different sampling rates using random masks. The original pattern was a letter ‘O’. The images were reconstructed according to sampling rates of 5%, 10%, 15% and 20% respectively. The resolutions of all the images were 40 by 40 pixels.

As can be seen from Figure.3.4, the image quality was getting better as the sampling rate increased. The edge of the pattern was getting more and more sharper. The quality of image reconstructed according to 20% sampling rate was quite good. There are different minimum sampling rates for different kinds of masks to achieve acceptable imaging quality. Quantitative evaluations of the quality of reconstructed images according to different sampling rates are shown in Table.3.1. The evaluation parameters used were Peak Signal-to-Noise Ratio (PSNR), Structural Similarity (SSIM) index, Mean Structural Similarity (MSSIM) and Feature Similarity (FSIM) index [223], [229].

Table.3.1 Quality evaluations of 40 by 40 pixels images reconstructed according to different sampling rates using random masks as shown in Figure.3.4.

Sampling rate	PSNR	SSIM	FSIM
5%	9.77	0.64	0.40
10%	10.49	0.69	0.45
15%	11.61	0.77	0.47
20%	12.59	0.82	0.50

Image quality VS resolution

A group of measurements have been done using random masks to study the relation between image resolution and the quality of reconstructed images. The original pattern ‘O’ and reconstructed images of different resolution (20 by 20 pixels, 40 by 40 pixels and 80 by 80 pixels respectively) are shown in Figure.3.5. The sampling rates of these reconstructed images were the same (20%).

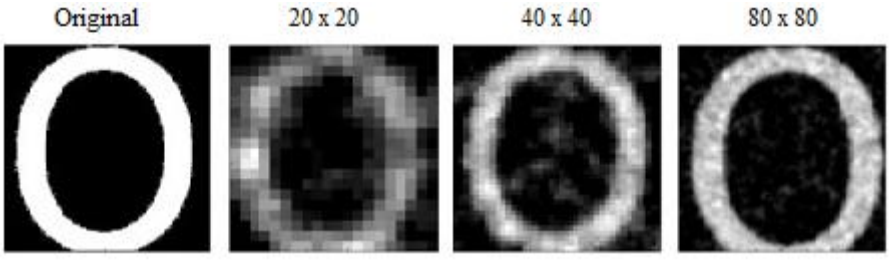

Figure.3.5 Experiment results of different resolution for the same pattern using random masks. The original pattern was the letter ‘O’. The images were reconstructed to different resolution from different measurements (20 by 20 pixels, 40 by 40 pixels and 80 by 80 pixels respectively). The sampling rates for all the images were 20%.

For the same sampling rate, the image quality was getting better as the resolution increased. The patterns in the reconstructed images were more clear and sharper. Quantitative evaluations of the quality of these reconstructed images are shown in Table.3.2. The sampling rates were the same but the number of measurements needed for different resolutions were different. More measurements were needed for a higher resolution which means longer measurement time. The resolution need to be selected appropriately depending on practical applications.

Table.3.2 Quality evaluations of images of different resolutions reconstructed according to same sampling rate as shown in Figure.3.5.

Resolution (pixels)	PSNR	SSIM	FSIM
20 x 20	9.85	0.63	0.61
40 x 40	12.59	0.82	0.50
80 x 80	14.48	0.89	0.48

3.2.3 Optimized masks: better performance in sampling rate

A set of masks were designed aiming at better sampling rate. The group of 40 optimized masks is shown in Figure.3.6. In brief, the binary masks were optimized to approximate the Karhunen-Loeve transform (KLT). The idea was quite similar to that of [240] where the 2D discrete cosine transform was quantized with the ternary set {1, 0, -1}.

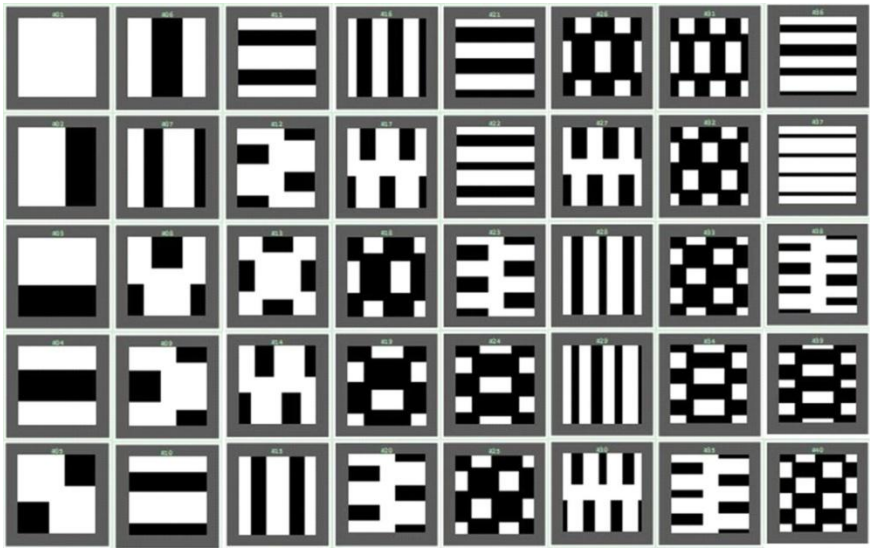

Figure.3.6 The set of 40 optimized masks for CS experiment.

Each mask comprised of 20 by 20 pixels. They were designed for sensing and reconstructing images of 20 by 20 pixels. The sampling rate was 10%, which performs much better than using random masks at the same sampling rate. A group of simulation experiments have been done to compare the reconstruction image quality of the 40 optimized masks and random masks. The original pattern 'O' and images reconstructed using the designed 40 masks (sampling rate 10%) and using random masks according to sampling rates (10%, 15% and 20%) are shown in Figure.3.7.

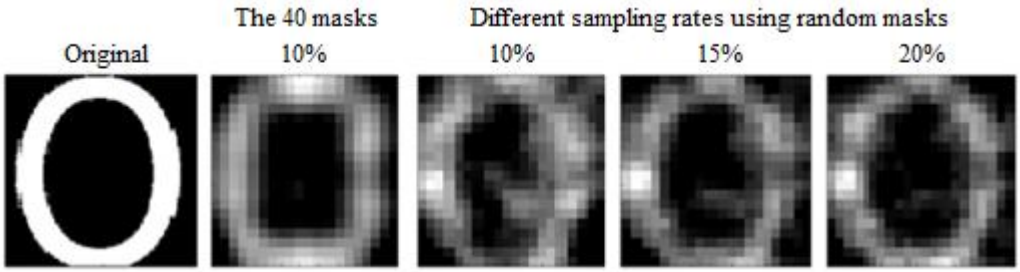

Figure.3.7 Comparisons of imaging quality between the 40 designed masks and random masks of different sampling rates. The original pattern was a letter 'O'. The sampling rate of image measured and reconstructed using the 40 designed masks was 10%. The sampling rates of images reconstructed using random masks were 10%, 15% and 20%. The resolutions of all the images were 20 by 20 pixels.

Although the sampling rate was only 10%, the image quality obtained using the 40 masks was much better than the others using random masks. Quantitative evaluations of the quality of reconstructed images according to different masks and sampling rates are shown in Table.3.3. Compared with random masks, by using designed masks, better image quality can be achieved at lower sampling rate.

Table.3.3 Comparisons of quality evaluations of 20 by 20 pixels images reconstructed using the 40 masks and random masks according to different sampling rates as shown in Figure.3.7.

	PSNR	SSIM	FSIM
40 masks	10.10	0.67	0.59
Sampling rate 10%	8.69	0.52	0.53
Sampling rate 15%	9.21	0.57	0.56
Sampling rate 20%	9.85	0.63	0.61

Several groups of measurements have been done using the 40 masks. The original patterns were 4 letters 'O', 'M', 'G' and 'T'. The simulation and experiment results obtained using the designed 40 masks are shown in Figure.3.8.

Figure.3.8 Simulation and experiment results of the 40 designed masks. Each image had 20×20 pixels and was reconstructed using the 40 optimized masks.

The sampling rates of all the images were only 10%, but the imaging quality was as good as those obtained using random masks. As shown in Table.3.4, the experiments results were as good as simulation results. The masks performed better on patterns with straight lines like the letter 'T' than others.

In CS imaging experiments, lower sampling rates means the number of measurements needed is less for the same size of resolution. Also, the computation complexity for the reconstruction process is much lower hence increase the reconstruction speed. These all increase the imaging speed. In practical applications, the imaging time is always limited so imaging speed is an important evaluation factor of a CS imaging system.

Table.3.4 Quality evaluations of 20 by 20 pixels images reconstructed using the 40 masks as shown in Figure.3.8. Simu is for simulation results and Expt is for experiments results.

	O		G		M		T	
	Simu	Expt	Simu	Expt	Simu	Expt	Simu	Expt
PSNR	10.10	10.13	11.05	10.79	8.84	8.74	12.10	12.04
SSIM	0.67	0.68	0.75	0.73	0.58	0.58	0.68	0.68
FSIM	0.59	0.57	0.62	0.60	0.48	0.49	0.53	0.54

3.2.4 Random masks chain: easier physical implementation

In CS measurements, one new mask is needed for every measurement. The imaging speed is usually limited by the transition speed of masks from one to another. In some cases, it's impossible to change masks manually for each measurement. By setting a series of random masks in a chain and then fixing the chain on a vertical or horizontal electric step stage is a way to increase the transition speed since it can be transferred automatically.

The matrix in Figure.3.9 is an 80 x 200 full random matrix, in which 0 and 1 have equal probabilities. The red box was the imaging window which was fixed to that location. For each measurement, the matrix shifted 3 pixels left so a new mask can be captured from the red window. Each mask was highly overlapped with the neighbouring ones. In practice, since each mask continues with the one before so it's easy and fast to transfer from one mask to another by fixing the whole physical random matrix on a horizontal step stage. The electric stage moved one step left to generate a new mask in the imaging window for each measurement.

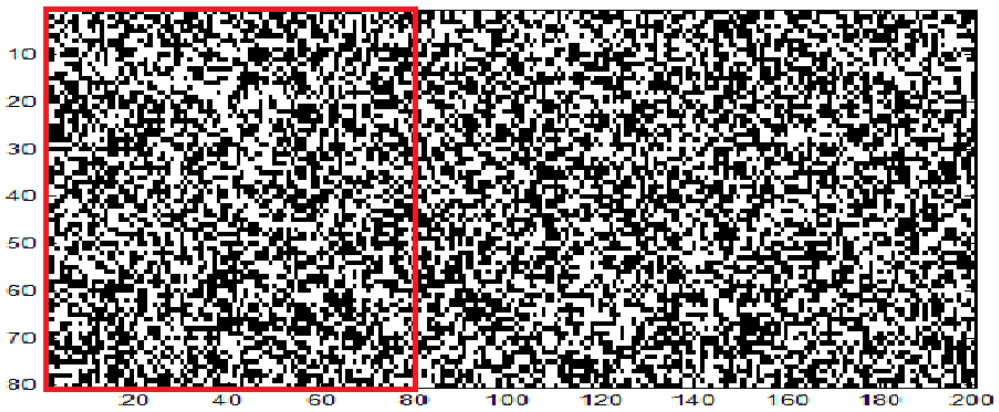

Figure.3.9 Image of an 80 x 200 full random matrix. The red box was an 80 x 80 mask window. For each measurement, the matrix shifted 3 pixels left so a new mask could be captured from the red window. In total, 40 masks of size 80 by 80 pixels could be generated from this 80 x 200 matrix.

A group of measurements have been done for patterns of 80 by 80 pixels using 1600 masks generated from an 80 x 5000 full random matrix this way.

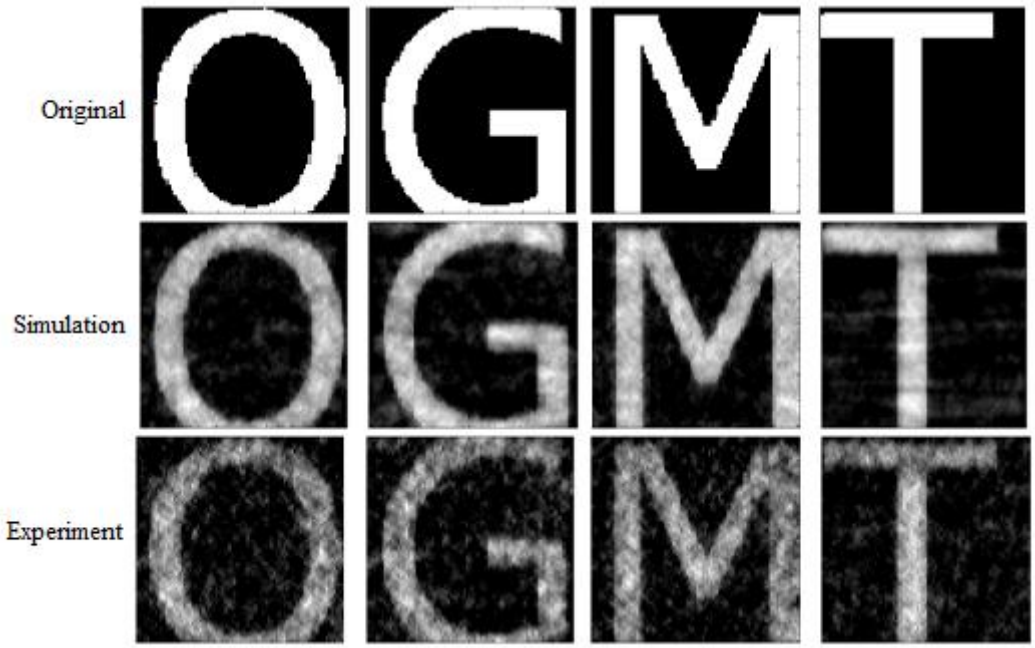

Figure.3.10 Simulation and experiment results of continued random masks captured from random matrix. Each image had 80×80 pixels and was reconstructed using 1600 random masks (equals to 25% sampling rate).

The sampling rates of these measurements were 25%. Although the masks used here were not full random ones, the imaging quality in simulation and experiment were both acceptable as shown in Table.3.5. The masks performed better on patterns with straight lines like the letter 'T' than others.

By using this stop – measure – shift routine, the measurements can be done automatically hence increase the imaging speed. Every mask was overlapped with its neighbouring ones so the system was more compact. The need for storage space and the complexity to fabricate physical masks were also reduced compared with fully random masks.

Table.3.5 Quality evaluations of 80×80 pixels images reconstructed using random masks captured from random matrix chain as shown in Figure.3.10. Simu is for simulation results and Expt is for experiments results.

	O		G		M		T	
	Simu	Expt	Simu	Expt	Simu	Expt	Simu	Expt
PSNR	12.88	9.91	13.04	9.96	13.37	9.34	15.46	12.30
SSIM	0.83	0.63	0.84	0.63	0.87	0.63	0.89	0.72
FSIM	0.47	0.36	0.47	0.36	0.50	0.38	0.47	0.36

3.2.5 High definition masks: Golay sequence modulated Hadamard matrix

If the resolution of the imaging system is large, the reconstruction computation complexity using random masks is really high and the process is time costing. There is strong need for easy and fast computable measurement matrix. Partial FFT and the Walsh-Hadamard transform (WHT) were introduced for fast computation of large resolution CS sensing since they already had many imaging applications. But most natural images were sparse in the DCT or the wavelet basis, which were coherent with FFT or WHT. Hence the idea to pre-modulate the signal through random permuatation or random sign flipping before applying FFT or WHT was developed [236, 237].

The HD imaging in this thesis was realized by pre-processing the signal using a binary Golay sequence before applying Hadamard transform. It can be considered as a de-randomized version of the random WHT operators. Golay sequence was defined by Marcel Golay in 1960 [238]. One of his definitions was as following:

a=[a(0), a(1), a(2),……a(N-1)] and b=[b(0), b(1), b(2),……b(N-1)] are two length N sequence where a_k , $b_k \in \{-1, +1\}$ and $0 \leq k \leq N-1$. The aperiodic correlation of a length N sequence q is defined as:

$$r(l) = \sum_{k=0}^{N-L-1} s(k)s(k+l)$$

a and b are defined to be a Golay complementary pair if:

$r_a(l) + r_b(l) = 0, \quad 1 \leq l \leq N-1.$

Then sequence a (or b) is defined as a Golay sequence.

The resulting measurement matrix was proved mathematically to be incoherent with DCT and wavelet basis [216] hence satisfied RIP, which is the fundamental condition of compressive sensing. By using this deterministic Golay sequence, it's simplified the hardware design since its needed less memory. In practical, the '1' and '-1' in the matrix mean 'transparent' and 'opaque' on the binary masks. ALL the images were

reconstructed using the NESTA package [239] and the reconstruction process was much faster than using random masks.

64 by 64 pixels: image quality VS sampling rate

A group of measurements have been done to study the relation between sampling rate and the quality of reconstructed images using HD masks. Part a) in Figure.3.11 shows the simulation results of different sampling rates and part b) shows the corresponding experiment results.

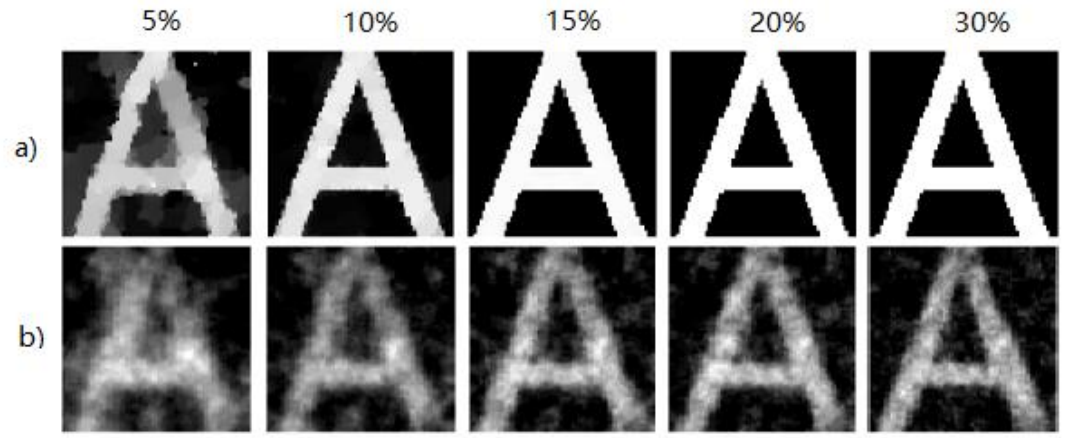

Figure.3.11 Images reconstructed according to different sampling rates using HD masks. The original pattern was a letter 'A'. a) shows the simulation results of reconstruction according to different sampling rates. b) shows the experiment results. All the images were 64 by 64 pixels.

As can be seen from part a), the image quality was acceptable around sampling rate 15%. The image quality wasn't getting much better as the sampling rate went higher than 20%. This meets the quantitative analysis of the quality of reconstructed images as show in Table.3.6. A visual relation between PSNR of reconstructed images and sampling rates is shown in Figure.3.12.

Table.3.6 Quality evaluations of 64 by 64 pixels images reconstructed using HD masks according to different sampling rates as shown in Figure.3.11. Simu is for simulation results and Expt is for experiments results.

Sampling rate	5%		10%		15%		20%		30%	
	Simu	Expt	Simu	Expt	Simu	Expt	Simu	Expt	Simu	Expt
PSNR	12.78	9.34	21.51	9.92	34.07	11.19	43.53	11.43	45.79	11.33
SSIM	0.84	0.59	0.98	0.63	1.00	0.74	1.00	0.75	1.00	0.74
FSIM	0.66	0.37	0.88	0.38	0.99	0.38	1.00	0.40	1.00	0.41

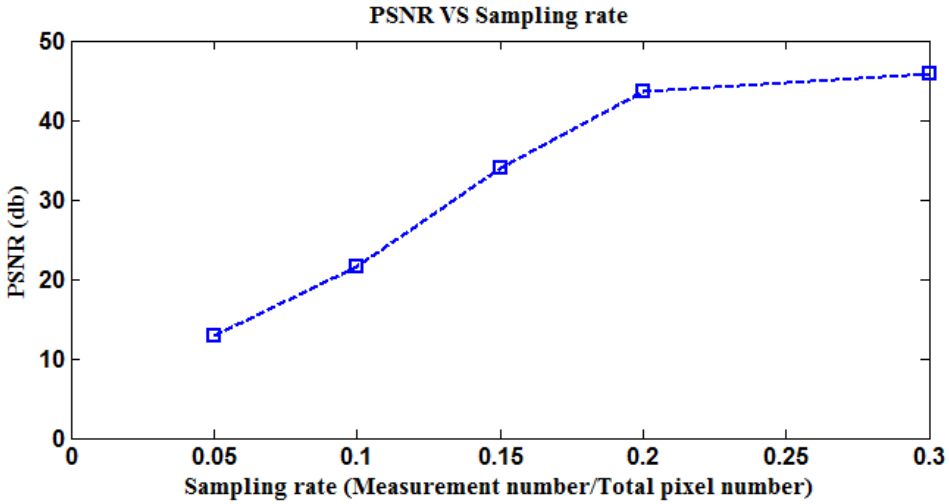

Figure.3.12 Relation between PSNR of reconstructed images and sampling rate of the HD mask.

128 by 128 pixels: HD masks VS random masks

Comparisons of image quality of simulation and experiment results using HD masks and random masks according to different sampling rates are shown in Figure.3.13.

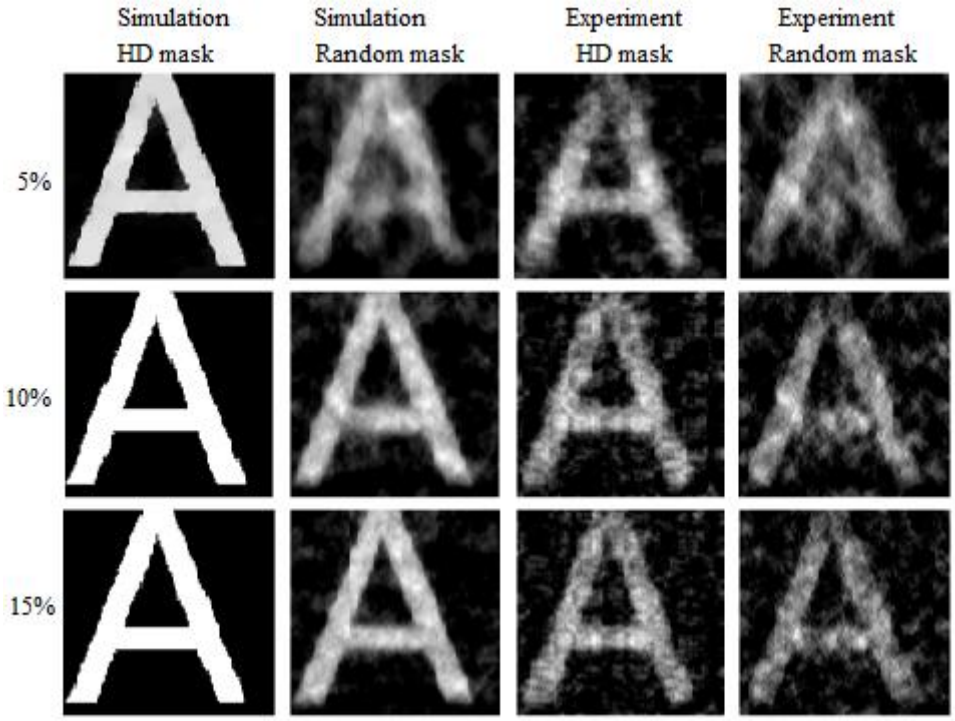

Figure.3.13 Comparison of imaging quality (simulation and experiment results) between HD masks and random masks in different sampling rates. All the images were 128 by 128 pixels.

The random masks used here were obtained from a full random matrix as discussed in Chapter 3.24. For any sampling rate show in Figure.3.13, the performance of HD masks was better than that of random masks. The reconstruction speed of HD masks

was much faster than that of random masks. The HD masks were more suitable for large scale CS imaging.

Table.3.7 Comparisons of quality evaluations of 128 by 128 pixels images reconstructed using random masks and HD masks according to different sampling rates as shown in Figure.3.13. Simu is for simulation results using HD masks, HD is for experiment results using HD masks and Random is for experiment results using random masks.

Sampling rate	5%			10%			15%		
	Simu	HD	Random	Simu	HD	Random	Simu	HD	Random
PSNR	20.56	11.08	9.22	46.59	11.18	9.93	52.19	11.31	9.87
SSIM	0.97	0.69	0.51	1.00	0.70	0.58	1.00	0.70	0.56
FSIM	0.89	0.40	0.40	1.00	0.35	0.36	1.00	0.36	0.35

256 by 256 pixels and 512 by 512 pixels: higher resolution

When the resolution get up to 256 by 256 pixels or 512 by 512 pixels, it was impossible to reconstruct using random masks since the computation complexity was far beyond the capacity of normal computer. While for HD masks, the resolution can get up to 512 by 512 pixels or even higher.

The simulation and experiment results of two 256 by 256 pixels images are shown in Figure.3.14. The numbers of measurements were 6500 which equals to a sampling rate of 10%.

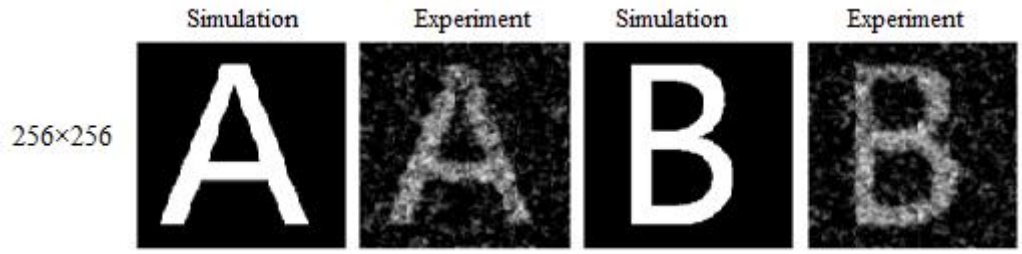

Figure.3.14 Simulation and experiment results of high resolution (256 by 256 pixels) measurements using HD masks. The sampling rate was 10% (6500 measurements).

Table.3.8 Quality evaluations of 256 by 256 pixels images reconstructed using HD masks as shown in Figure.3.14.

	A		B	
	Simulation	Experiment	Simulation	Experiment
PSNR	52.63	11.28	54.08	11.21
SSIM	1.00	0.60	1.00	0.63
FSIM	1.00	0.37	1.00	0.35

The simulation and experiments results of a 512 by 512 pixels pattern are shown in Figure.3.15. The sampling rate was 15% which equals to 40000 measurements. The size of the imaging window on the screen was 512 by 512 pixels. In previous experiments, several physical pixels on the screen added up to one pixel on the pattern depending on the pattern size. In this case, one physical pixel on the screen was corresponding to one pixel of the pattern.

Figure.3.15 Simulation and experiment results of 512 by 512 pixels measurements using HD masks. The original pattern was a letter 'A'. The sampling rate was 15% (40000 measurements).

The experiment result was not as good as simulation even at sampling rate of 15%. This might be caused by the low signal to noise ratio since the light from a single physical pixel on the screen was too weak. Using a computer screen which has a larger resolution might be an option to improve the quality of reconstruction images at high resolution (512 by 512 pixels or larger). The experiment result is really dark so using a brighter screen might be an option to increase the brightness.

Table.3.9 Quality evaluations of 512 by 512 pixels images reconstructed using HD masks as shown in Figure.3.15.

	PSNR	SSIM	FSIM
Simulation	45.38	1.00	1.00
Experiment	4.28	0.00	0.74

Nature patterns

A group of measurements have been done using HD masks to measure more nature patterns rather than letters. The original patterns together with the simulation and experiment results are shown in Figure.3.16. The image size was 128 by 128 pixels and the sampling rate was 15%.

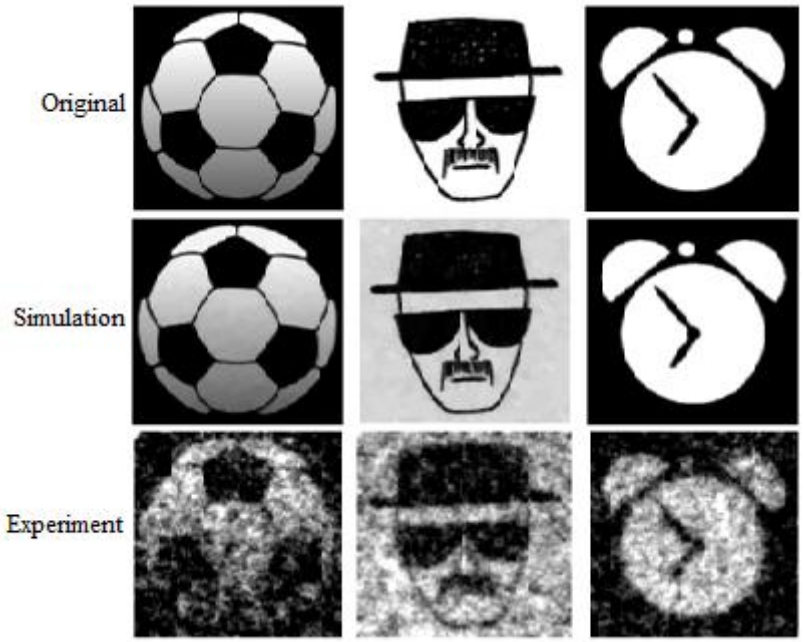

Figure.3.16 Simulation and experiment results of a group of common patterns. Each image had 128×128 pixels and was reconstructed using 2500 HD masks. The sampling rate was 15%.

Compared with images of same size and same sampling rate shown in Figure.3.13, the image quality of simulation results was about the same while for the experiment results, the image quality varied from different patterns. The quality of the reconstructed 'clock' was much better than the other two.

Table.3.10 Quality evaluation of 128×128 pixels more common images reconstructed using HD masks as shown in Figure.3.16.

	Ball		Man		Clock	
	Simulation	Experiment	Simulation	Experiment	Simulation	Experiment
PSNR	30.16	6.46	16.70	4.65	47.96	9.05
SSIM	1.00	0.02	0.96	0.24	1.00	0.61
FSIM	0.97	0.65	0.91	0.48	1.00	0.40

3.3. Projector based CS imaging set up

3.3.1 Experimental set up

A schematic diagram of the projector based compressive imaging system is shown in Figure.3.17. This system was evolved from the on screen based system. Instead of showing the masks and patterns on computer screen, the images of masks and patterns were projected on to a physical surface. The scattering light from the physical surface

was collected by a set of lens and focused onto a detector. The on screen system can be considered as half simulation half physical method for masks quality validation while this system can achieve full physical validation. The total physical pixel number of the imaging window was 512 by 512 pixels, which was the same as the on screen system.

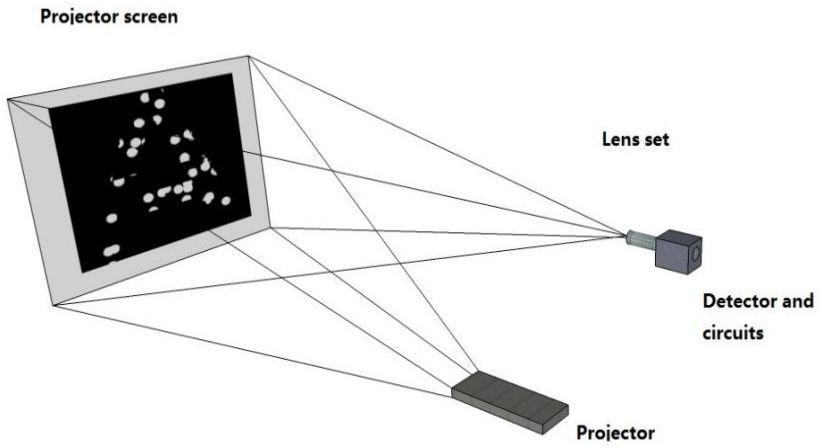

Figure.3.17 Projector based CS imaging system. The images of masks covered by a pattern were projected on to a white surface. The scattering light was collected by a set of lens and focused onto the photodiode detector. The detected data were amplified by a set of circuit.

Measurements have been done to develop the relation between the spatial distribution of luminance of the projector and the response of the detector. The effective projector area was divided into 24x24 (576) equal sized blocks. At the start, all the blocks were black. Each block lighted up in sequence and by the end, all the blocks were illuminated. The detector measured the whole lighting up procedure.

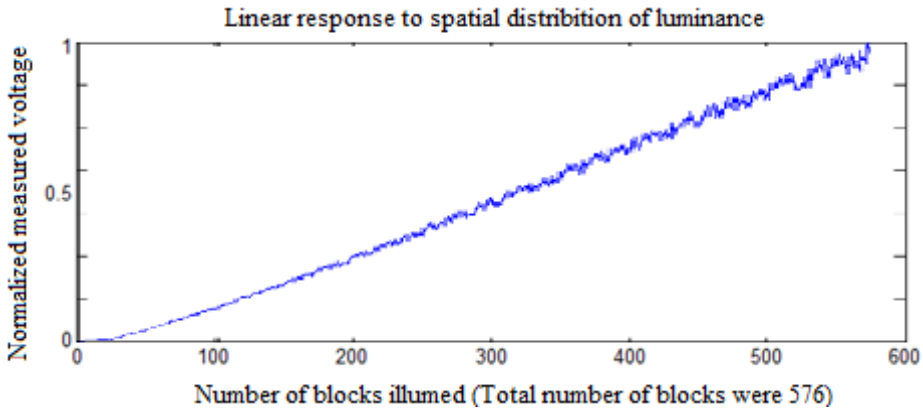

Figure.3.18 Response of the detector against spatial distribution of brightness of the projector. The x axis was the number of blocks that light up on the projector screen. The y axis was the corresponding response of the detector. The projector screen was divided into 24x24 (576) equal sized blocks in total.

The relationship can be assumed as linear which means each block of the effective projector area contributed equally to the value that the detector measured. A picture of the system is shown in Figure.3.19. As can be seen from the picture, the system was quite simple and compact. As long as the distance from the projector to the projection surface and angle between the projector and the lens set were fixed, details on the projection surface can be captured. This gives the system a potential to measure physical patterns by projecting the masks onto a physical subject.

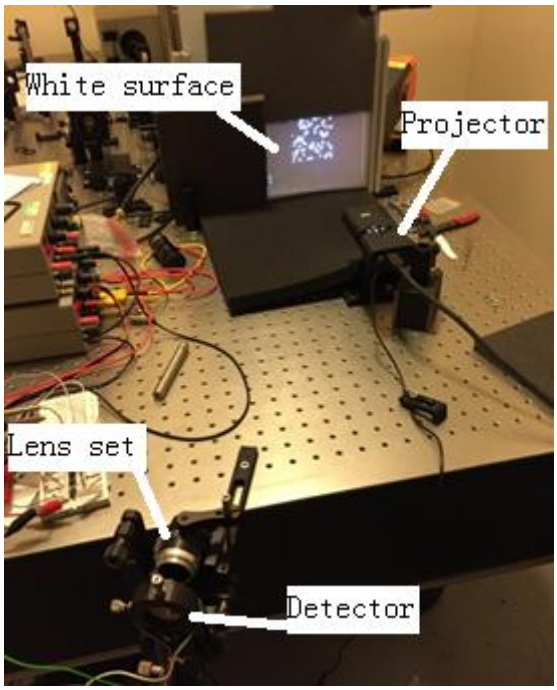

Figure.3.19 Photo of the projector based CS imaging system set up. The masks were projected onto a piece of white paper. The scattering light were collected by the lens set and focused onto the detector. The data the detector measured were used for reconstruction.

3.3.2 High definition CS experiment

Projector system VS on screen system

A group of measurements have been done using a projector system for the same patterns as shown in Figure.3.16. Part a) in Figure.3.20 shows the results obtained using the projector system. Part b) shows the results obtained using on screen system. The image size is 128 by 128 pixels and the sampling rate is 15%.

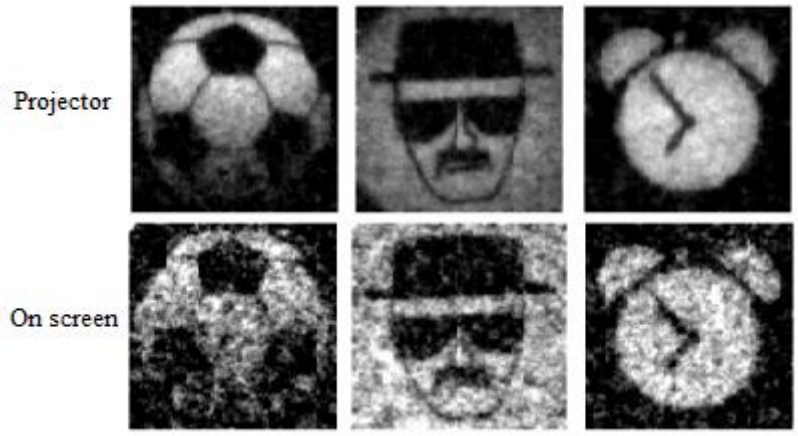

Figure.3.20 Comparison of imaging quality of on screen system and projector system (128×128 pixels images). Each image was reconstructed using 2500 HD masks corresponding to a sampling rate of 15%.

As can be seen from the figure, the performances of the projector based system were much better than the on screen system. The brightness of the projector was much stronger than that of a screen so the signal power was much stronger. For the same level of background noise, the projector system performs better in terms of SNR.

Table.3.11 Comparisons of quality evaluations of 128×128 pixels images reconstructed using HD masks measured with projector system and on screen system as shown in Figure.3.20. Projector is for results obtained using projector system and Screen is for experiments results obtained form on screen system.

	Ball		Man		Clock	
	Projector	Screen	Projector	Screen	Projector	Screen
PSNR	14.00	6.46	5.98	4.65	11.45	9.05
SSIM	0.82	0.02	0.41	0.24	0.79	0.61
FSIM	0.55	0.65	0.54	0.48	0.52	0.40

A group of measurements have been done using projector system for a 256 by 256 pixels pattern.

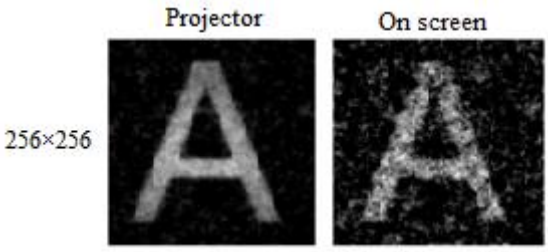

Figure.3.21 Comparison of imaging quality of on screen system and projector system (256×256 pixels images). Each image was reconstructed using 6500 HD masks corresponding to a sampling rate of 10%.

The quality of image reconstructed using data measured from projector system was much better than that from on screen system. The image obtained from the projector system was much cleaner and the edge of the pattern was much sharper.

Table.3.12 Comparisons of quality evaluations of 256×256 pixels images reconstructed using HD masks measured with projector system and on screen system as shown in Figure.3.21. Projector is for results obtained using projector system and Screen is for experiments results obtained form on screen system.

	PSNR	SSIM	FSIM
Projector	14.36	0.81	0.52
Screen	11.28	0.60	0.37

Physical patterns

As discussed before, the projector system has potential in measuring physical patterns. A comparison in imaging quality between physical pattern and projected pattern of different sampling rate is shown below in Figure.3.22. In the projected pattern part, the pattern 'A' was projected onto the white projector screen. While in the physical pattern part, the pattern was a physical one printed on a piece of paper and the masks were projected onto the paper. The resolutions of both patterns were 256 by 256 pixels.

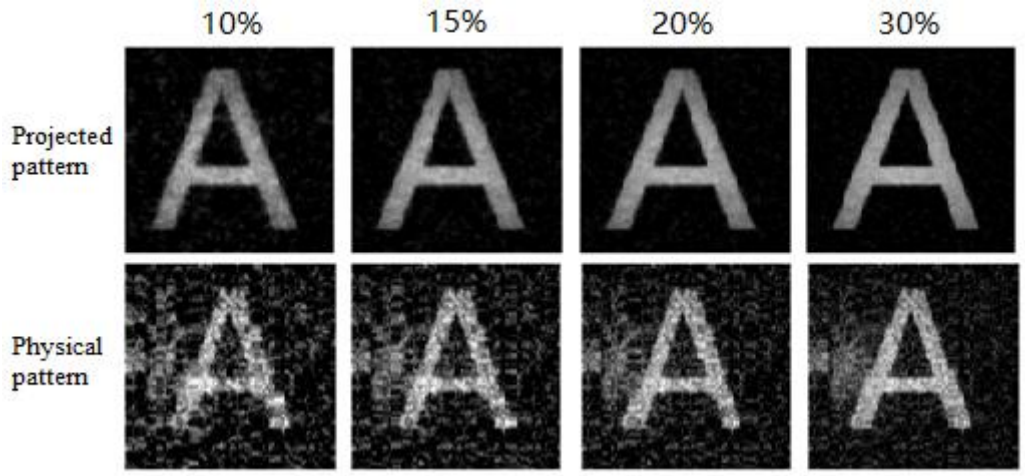

Figure.3.22 Comparison of imaging quality of projected pattern and physical pattern in different sampling rates. The projected pattern was a character 'A' projected on to a white paper and the physical pattern was a character 'A' printed on a piece of paper. All the reconstructed images were 256 x 256 pixels.

For the physical pattern, the letter ‘A’ was recognizable at 10% sampling rate while the images were not as clean as the projected ones even at 30% sampling rate. The physical pattern was in black/white printing and the black ink led to some reflections from the projection. The noise dots in the reconstructed image were mainly caused by the reflections from the black ink.

The masks were projected on to a pile of books to study the performance of the system on more physical subject rather than letters as shown in Figure.3.23. The reconstructed images of size 256 by 256 pixels at different sampling rate are shown in the rest part in Figure.3.23. At 30%, the quality of the reconstructed image was quite good.

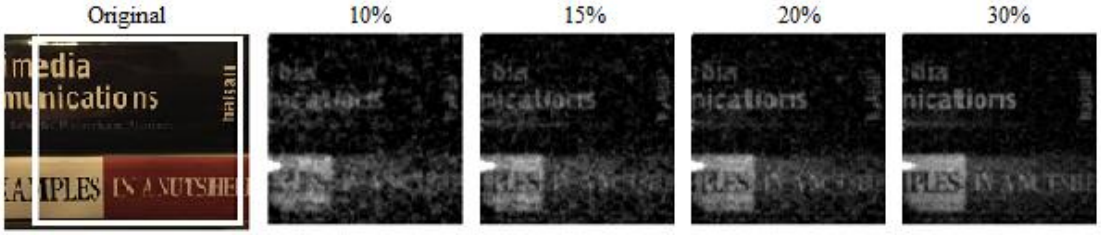

Figure.3.23 Images reconstructed according to different sampling rates using HD masks for a pile of books. The white box is the effective imaging area. All the reconstructed images were 256 x256 pixels.

A comparison of 512 by 512 pixels images obtained using projector system and on screen system is shown in Figure.3.24. The original pattern was a physical character ‘A’ cut out from a piece of black paper. The on screen one was the same as shown in Figure.3.15. Both images were obtained at15% sampling rate. The quality of the image obtained using projector based system was much better than the one obtained using on screen based system

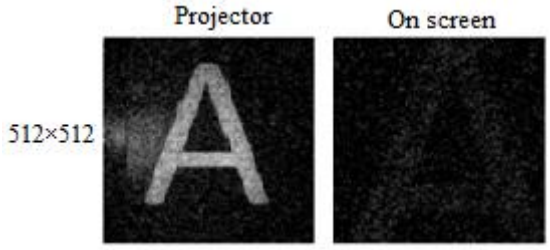

Figure.3.24 Comparison of imaging quality of on screen system and projector system (512×512 pixels images). Each image was reconstructed using 40000 HD masks corresponding to a sampling rate of 15%.

3.4. Noise analysis

The noises in the on screen CS system can be classified as electric noise and light noise. The electric noises in the measurement process were mainly from the amplifier circuit. The detector used was very raw and fundamental. All the amplifier circuit components were set up on a bread board which increased the electric noises. The other electric noises including noise from data acquisition device and the detector itself were minor. One source of the light noises was the environmental light. The detector was extremely sensitive. The effective wavelength of the photodiode covered both the infrared and visible range. Although the measurements were taken with the light switched off, any other light source nearby the detector, both visible and infrared ones (for example, light from computer or instrument screen, heat from instrument or human body), were added up to the noise. Another source of light noises was duo to the system itself. The light from the screen was collected by the lens directly. The light from the center part of the screen contributed more than the edge part to the measured intensity.

The projector CS system performed better against these noises. The detector used in the projector was a commercial one with built in amplifier circuit. This integrated circuit minimized the electric noise to an acceptable level. The light intensity from the projector was much stronger than that from a computer screen. The signal power measured by the detector was much stronger hence increase the optical signal to noise ratio. Instead of projected directly onto the detector, the scattering light from a projector screen was collected by the lens and detector. Every part of the effective projector area contributes equally to the value the detector measured.

3.5 Summary and Future work

To realize fast experimental validation for CS imaging sampling operator design, an on screen CS imaging system was set up. The system can be considered as an adapted version of the famous single pixel camera configuration. In the on screen based CS

system, there were no physical masks or samples so no need to fabricate the masks physically, which was time and cost effective. Also there was no limitation on speed of changing the masks.

In this chapter, some main criteria of CS imaging masks designing including imaging quality, sampling rate, resolution, implementation complexity and imaging speed were demonstrated by using the on screen CS imaging system. The computation complexity of reconstruction will be far beyond the capacity of a normal computer if the resolution is high (256 by 256 pixels). An idea of HD masks achieved by Golay sequence modulated Hadamard matrix was proposed and validated by using the on screen based CS imaging system.

There are several limits of this system as discussed in the noise analysis part. The projector based CS imaging system was evolved from the on screen one to improve against these limits. Compared with the on screen system, the resolution could get up to 512 by 512 pixels and the qualities of reconstructed images were still good by using the HD masks. Moreover, the masks were projected onto a physical subject and an image of the physical subject can be reconstructed.

The projector CS imaging system had shown good capability in fast masks designing validation for images up to 512 by 512 pixels (limited by the resolution of the projector). The system was very compact, cost effective and easy to configure so any group doing research on CS masks designing can use this set up to obtain proof-of-concept experimental results. The system can be considered as an active imaging system. The compact design and low storage requirements gives the system lots potential in real world imaging such as car registration recognition in traffic control or car park control, which suffers huge storage pressure for now.

Chapter 4

Spinning disk design for THz CS

4.1. Sampling operator design for spinning disk

In practical compressive imaging systems, the measurement matrixes are implemented by using a spatial light modulator (masks) to vary the amplitude of light waves based on mechanical or electro-optical methods. Practical applications find that mechanical methods are well suited for imaging at both optical and THz frequencies [217], [218]. In previous work of our group, a single pixel THz imaging idea was developed [18]. A spinning disk with a number of 1 mm diameter square holes was designed from nearly block Toeplitz matrix as masks. The disk was fixed on a motorized rotating stage and the measurements were taken automatically on a stop-measure-rotate routine. The stage rotated one step, one new mask was generated and the detector took one measurement. By using a spinning disk, the mask transition speed was highly increased; hence speed up the imaging procedure. Compared with other single pixel cameras [15, 17, 219, 220], this system performs better in imaging speed.

The spinning disk was made on a 0.5-mm-thick standard print circuit board (PCB) [221]. The PCB substrate material strongly absorbed THz radiations particularly at higher frequencies. In addition, the absorption and the dispersion caused by the PCB substrate wasn't uniform across the whole substrate. More importantly, the THz radiation spans a frequency range from 300 GHz to 10 THz (wavelength is from 1mm to 30um) [222]. Thus, when the pixel size of such masks was close to the wavelength of THz radiation, the scattering and the diffraction effects can no longer be negligible. The imaging performance of this system was limited since the scattering effect of THz radiation at the sharp corners will degrade the overall signal to noise rate. These all added noises to the imaging procedure and affected the encoding accuracy thus

weakening the quality of the reconstructed images. The spinning disk was applied in a typical THz pulse imaging system [223], the imaging quality was not very good and no time domain information could be measured.

In order to improve the overall signal to noise ratio, a new disk was designed using relatively larger circular holes of 2 mm diameter as masks and without substrate. A picture of the disk is shown in Figure.4.1. This spinning disk was made from a 0.28 mm thick steel plate. The diameter of the plate was 200 mm. A number of 2 mm diameter holes were chemically etched on this steel plate randomly. Each hole was 100% transparent to light while the stainless steel was 100% opaque to light.

Figure.4.1 A picture of the metal spinning disk. The disk was made on a 0.28mm thick steel plate. The diameter of the disk is 200mm. The cut through holes were of diameter 2mm.

This disk has no substrate so there was no absorption and dispersion caused by the substrate material. The size of the round holes on the disk was relatively larger than the square hole in the early designed disk so the performance against diffraction and scattering effects were better.

When spinning the disk step by step, a sequence of effective mask was obtained from the rectangular window in blue (as shown in Figure.4.2) with different binary patterns. One measurement was taken for each step corresponding to each mask. After certain steps, a set of effective masks and measured data can be obtained for reconstruction.

The maximum size of effective window which can be covered by the spatial modulation patterns on the disk was about 40mm by 40mm. The disk was designed for 2 inches optical system. In the practical system, the diameter of the parabolic mirrors was 2 inches so the maximum size of effective imaging window can be applied was 35 mm by 35 mm. In practical, to leave some margin, the imaging window size was 30mm by 30mm.

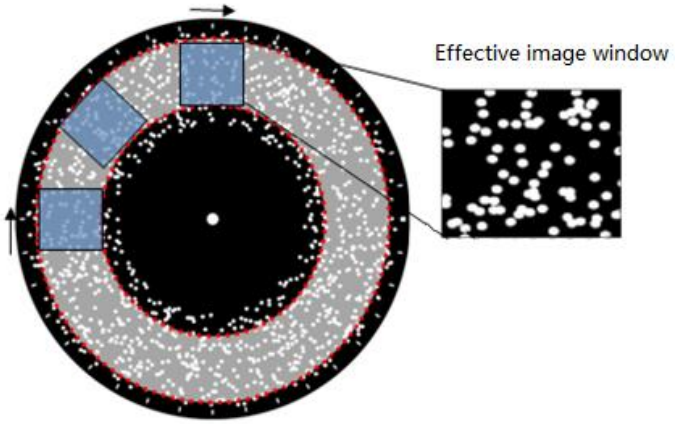

Figure.4.2 Diagram of imaging window and effective imaging area on the spinning disk. When spinning the disk, each effective mask was obtained from the rectangular window in blue with different binary patterns. Then, a set of effective masks were obtained for reconstruction. The effective imaging area was the ring area between two dashed red lines.

The sampling operator Φ on the disk could be considered as a Toeplitz block matrix [224-228]. Haupt [165] and Sebert [166] have shown that Toeplitz-structured matrix was memory efficient with fast implementation. The measurement matrix generated from the spinning disk from 500 measurements was illustrated in Figure.4.3.

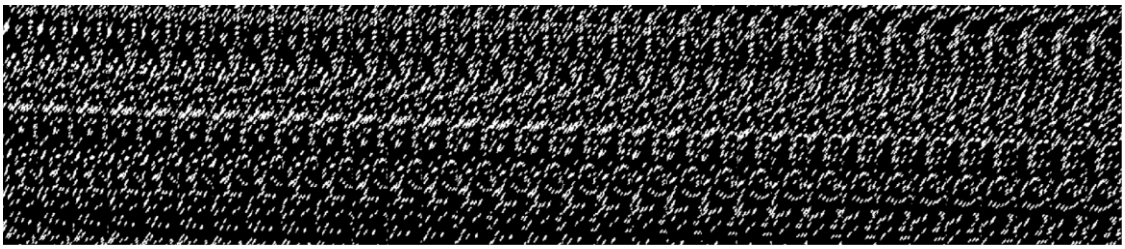

Figure.4.3 One set of Teoplitz-structured measurement matrix obtained from the disk.

In practical, the holes were not 100% randomly allocated since the part which was not etched off the metal plate must be continuous.

4.2. Imaging quality and resolution

Reconstruction quality

A set of comparative analysis on different measurement matrices were made and the corresponding results are shown in Figure.4.4. In this test, the parameters of the tested matrices were set to the same (including image size, sampling rate and reconstruction algorithm).The image size was 64×64 pixels. The size of each measurement matrix was $1200 \times 64 \times 64$ thus the sampling rate was around 30% which was sufficient for obtaining acceptable quality results.

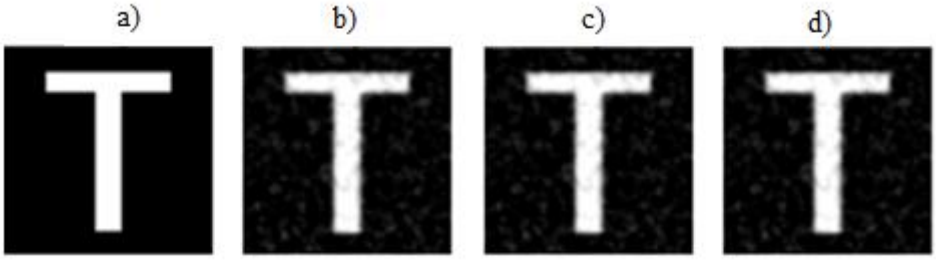

Figure.4.4 A comparison of reconstruction performance of different matrixes. a) Original image of letter 'T'. b) Reconstructed image using random matrix. c) Reconstructed image using partial Hadamard matrix. d) Reconstructed image using the Toeplitz-structured matrix obtained from the spinning disk.

The quantized comparisons of the reconstructed images obtaining by using random matrix, partial Hadamard matrix and the spin disk are shown in Table.4.1. The evaluation parameters used were Peak Signal-to-Noise Ratio (PSNR), Structural Similarity (SSIM) index and Feature Similarity (FSIM) index [223], [229].

Table.4.1 Quality evaluations of images reconstructed using different random masks, partial Hadmard masks and the spinning disk as shown in Figure.4.4.

Measurement matrix	PSNR	SSIM	FSIM
Random matrix	19.15	0.93	0.56
Partial Hadmard matrix	19.12	0.94	0.56
Spinning disk	19.00	0.93	0.57

Note that, the reconstruction quality achieved by using the spin disk measurement matrix (nearly block Toeplitz matrix) was close to the level of the well-proved CS matrices such as random matrix.

Resolution

The resolution performance of masks based on square patterns and circular patterns are shown in Figure.4. 5. The diameter of the circular pattern 'D' is twice of the width of the square pattern'd' (D=2d). When measuring a linear edge sample or an arc edge sample, the minimum sampling size 'L' is equal to the width of the square sampling pattern but only half of the diameter of the circular sampling pattern. The minimum size of the sample that can be captured was the same but the diameter of the circular pattern was larger than the square pattern. This make the circular pattern masks perform better against scattering and the diffraction effects, while the same capability of resolution remains.

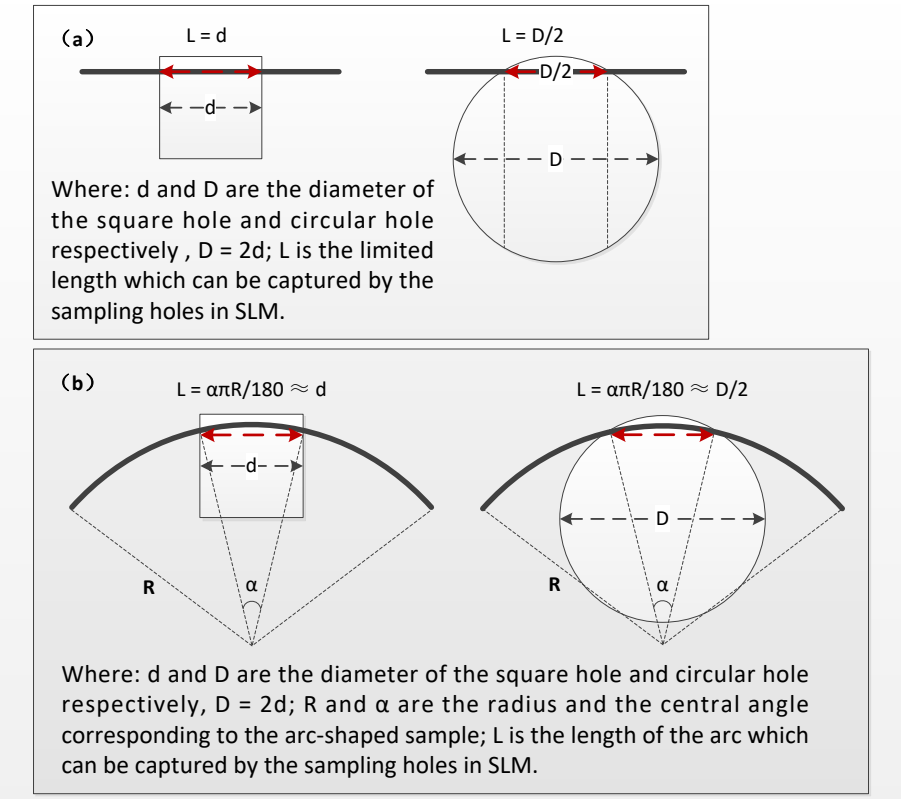

Figure.4.5 Resolution performance using square pattern based masks and circular pattern based masks on linear edge sample and arc edge sample.

A series of patterns were tested in simulations in order to analysis the resolution of the spinning disk. The widths of the white stripes of the test patterns were 6 mm, 3 mm and 2 mm, respectively in part a), b) and c) of Figure.4.6. A standard star pattern in d) was used to test the resolution. The white part represented 100% light transmission

and the black part represented 0% light transmission. The reconstructed images of these test patterns by using the 2 mm diameter circular pattern based masks are shown underneath.

The size of each image was 128×128 pixels and was reconstructed using 2000 measurements, corresponding to a sampling rate of 12%. A resolution of better than 2 mm had been achieved with the 2 mm diameter circular pattern masks. This was a significant result, especially for THz imaging where the wavelength is longer. The bigger the size of measurement patterns, the better performance against scattering and the diffraction effects.

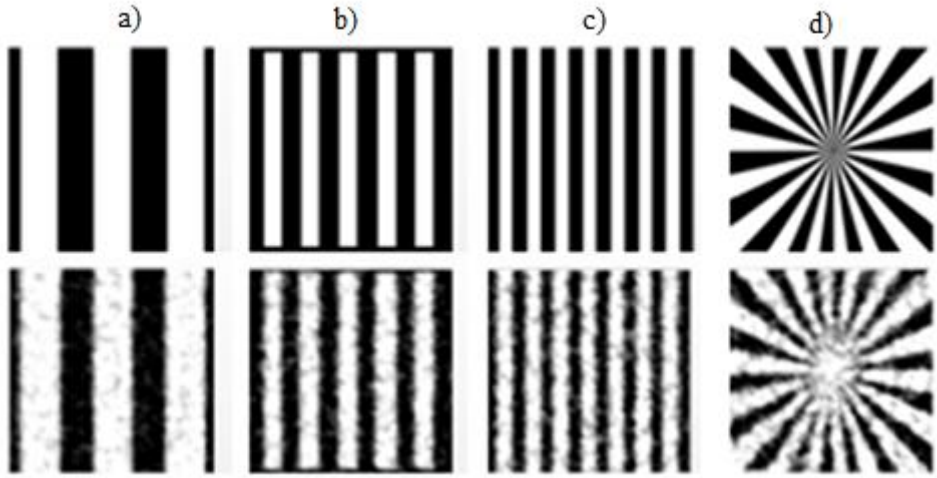

Figure.4.6 Resolution test of the spinning disk. The widths of the white strips are 6mm, 3mm, 2mm respectively in a), b) and c). A star pattern is shown in d). Corresponding reconstruction results using the spinning disk are shown underneath. All the images were 128×128pixels obtained from 2000 measurements (sampling rate: 12%).

4.3. Experiment on the projector based system

The disk worked on a stop-measure-rotate routine. One mask was obtained from each step. The stage rotated 0.25 degree for each step so after 360 degree, a sequence of 1440 masks were obtained. Several CS experiments have been done using this set of 1440 masks in the projector based system. The experiment procedure was the same as discussed in Chapter 3.3.1. The images of masks and patterns were projected on to a physical surface. The light reflected by the physical surface was collected by a set of lens and focused onto a detector.

A group of measurements have been done using the 1440 masks for a sample ‘A’ as shown in Figure.4.7 to verify the imaging quality of these masks. The resolution of reconstructed image was 9216 pixels (96 by 96 pixels). 1440 measurements were taken so the sampling rate was about 16%.

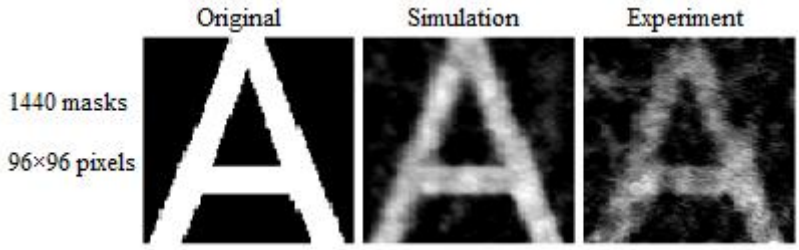

Figure.4.7 Simulation and experiment results using the set of 1440 masks captured from the spinning disk. The original pattern was a character 'A'. The two images were 96 by 96 pixels reconstructed from 1440 measurements.

The comparison of the 1440 measured data points and the simulation data points is shown below.

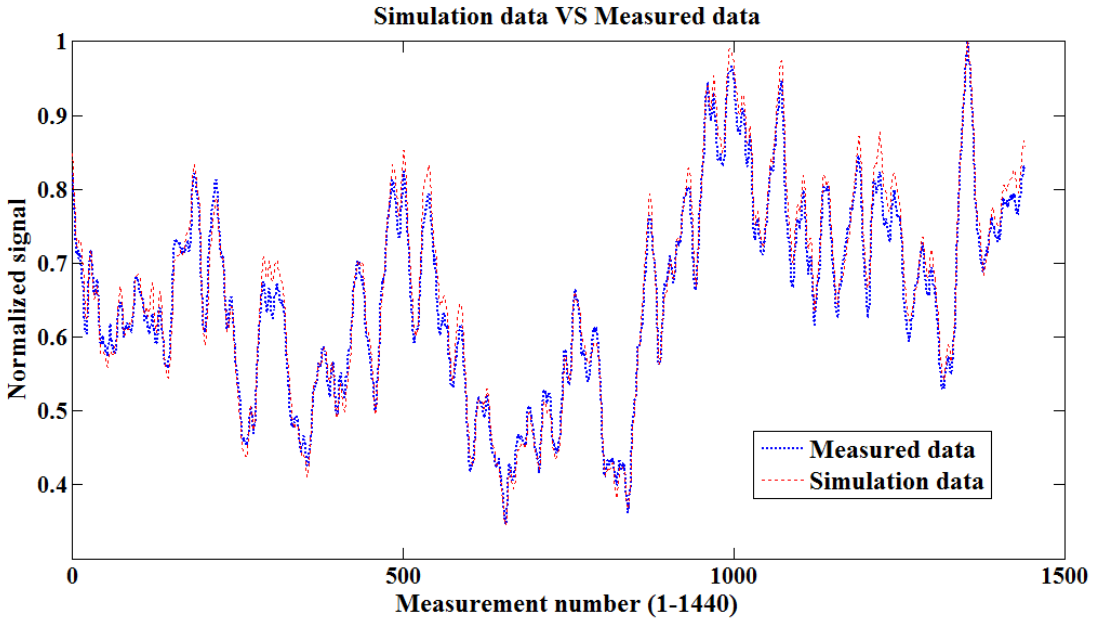

Figure.4.8 Comparison between the simulation data and measured data of the 1440 measurements used in Figure.4.7. The red points were the simulation data and the blue points were the measured data. Both of them were normalized.

Most parts of the measured data and simulation data were matched except several data points. The simulation and measured results can show fundamental characters of the original image. More quantified evaluations of these reconstructed images are shown in Table.4.2.

Table.4.2 Quality evaluations of 96 by 96 pixels images reconstructed using the spinning disk as shown in Figure.4.7.

	PSNR	SSIM	FSIM
Simulation	13.20	0.85	0.48
Experiment	9.21	0.55	0.36

Some experiments have been done using physical samples and the reconstructed images are shown in Figure.4.9. In contrast to the previous experiments, the set of 1440 masks were projected onto physical samples. These three samples were printed to black/white by a normal printer on a piece of paper. The scattering light form the samples was collected by the lenses and focused onto the detector. The light was assumed to be totally absorbed by the black part.

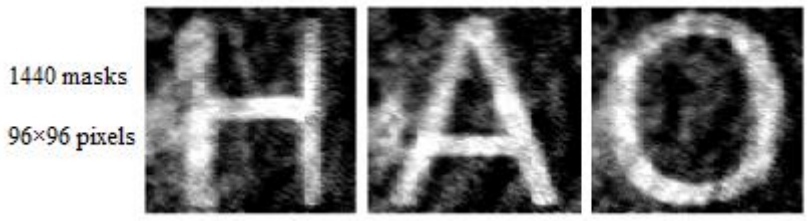

Figure.4.9 Several images reconstructed from 1440 measurements on physical samples. All the resolutions were 96 by 96 pixels.

The quality of these reconstructed images was acceptable but they all had a bright spot in the left middle part. This was due to the reflection from the black part of the samples. The lenses were designed to collect scattering light not reflected light. The black part of the samples which was black ink hadn't absorbed the light from the projector completely. The angle between the projector and the lenses made the reflection collected by the lenses resulted in the bright spot.

To get rid of the light spot on the left side of reconstructed images, a sample which was a letter 'T' cut through more gloss black paper was used. The gloss surface absorbed light better than normal paper therefore reducing the reflection. Picture of the sample used and comparisons of the experiment and simulation results are shown in Figure.4.10.

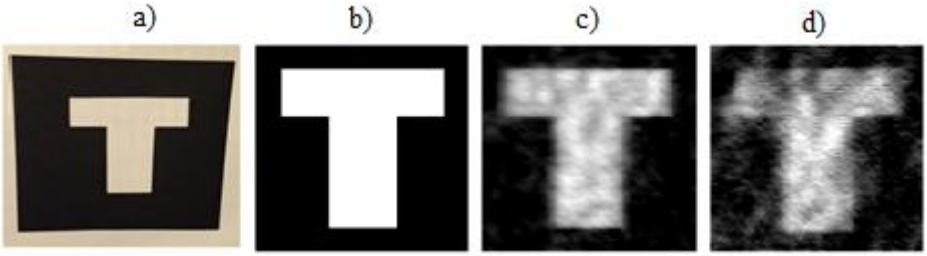

Figure.4.10 A physical pattern and its simulation and measurement results. a) shows a picture of the physical pattern 'T'. b) shows a binary version of the sample. c) shows the simulation results using the set of 1440 masks. d) shows the reconstructed image from 1440 measurements. The resolution is 96 by 96 pixels.

The light spot caused by the reflection from the sample disappeared as shown in d) of Figure.4.10. The image quality was as good as the one obtained from projected samples. The comparison of the 1440 measured data points and the simulation data points is shown below. More quantified evaluations of these reconstructed images are shown in Table.4.3.

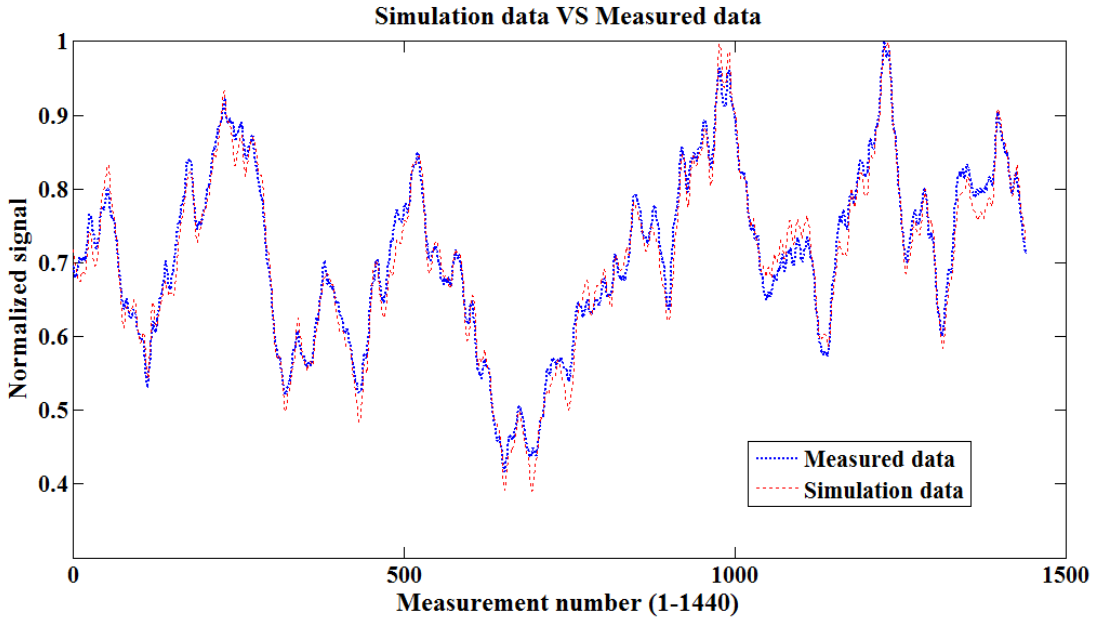

Figure.4.11 Comparison between the simulation data and measured data of the 1440 measurements used in Figure.4.10. The red points were the simulation data and the blue points were the measured data. Both of them were normalized.

Table.4.3 Quality evaluation of 96 by 96 pixels images reconstructed using the spinning disk from physical sample as shown in Figure.4.10.

	PSNR	SSIM	FSIM
Simulation	14.72	0.90	0.45
Experiment	10.71	0.67	0.37

Measurements on a pile of books as shown in Figure.4.12 have been done. The masks were projected onto the pile of books and the effect imaging area was the white rectangular window. The reconstructed image showed the basic structure of the original image. The resolution was 96 by 96 pixels and was reconstructed from 1440 measurements.

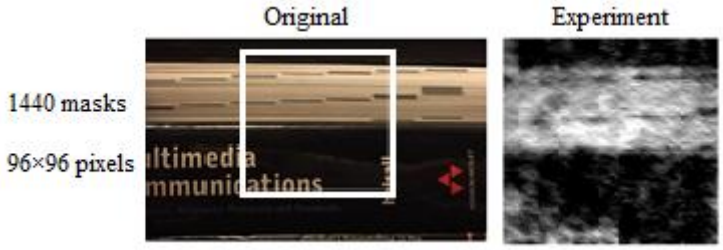

Figure.4.12 Images reconstructed according to 1440 measurements for a pile of books. The white box was the effective imaging area. The resolution was 96 by 96 pixels and sampling rate was 16%.

4.4. Experiment on an infrared system

The experiment set up of the infrared CS imaging system using spinning disk is shown in Figure.4.13. An infrared LED was used as light source and a photodiode was used as detector. The light from the LED was collected by a parabolic mirror and travelled through the sample and the disk. Then the light was focused onto the detector by another parabolic mirror. The system can be considered as an adaptation from the single pixel camera. The projections of the sample and masks were recorded to reconstruct a 2D image.

Before applying the spinning disk in THz system, the imaging quality of the spinning disk was checked using the infrared CS imaging system. The spinning disk was designed for 2-inches optical system. The parabolic mirrors, spinning disk and the samples used in the infrared system were the same as in a THz system so the results should be more convincing than using the projector system. Another benefit was the wavelength of infrared was closer to that of THz so the scattering and diffraction effects in the infrared system were more similar to those in a THz system.

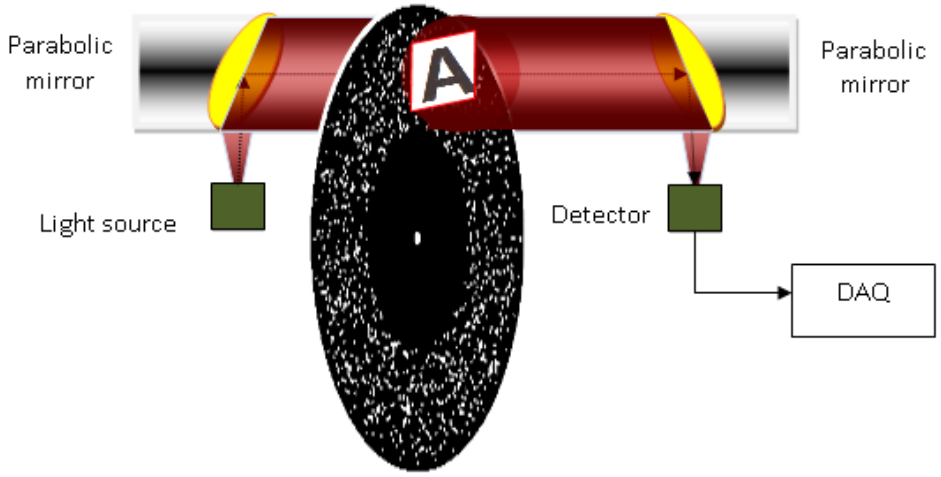

Figure.4.13 Spinning disk based CS imaging system. The light from a point light source was modulated to parallel wave by a parabolic mirror. The parallel wave transmits through the imaging area of the spin disk and the sample and then was collected by another parabolic mirror and focus on to a detector. (DAQ: data acquisition device)

A picture of the system is shown in Figure.4.14. The size of the effective image window was 33 mm × 33 mm. Every step the disk rotated 0.25 degree and the detector took a measurement. 1440 measurements were needed to reconstruct a 9216 pixels (96 by 96 pixels) image. Measurements on samples which were letter 'A' and 'B' have been done using the spinning disk. All the patterns were cut through on copper tapes. The sampling rate was about 16%. The reconstructed images are shown in Figure.4.15.

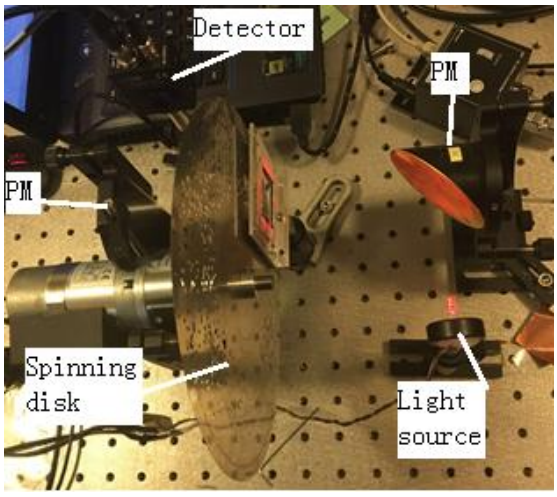

Figure.4.14 Picture of the spinning disk based CS imaging system. (PM: parabolic mirror)

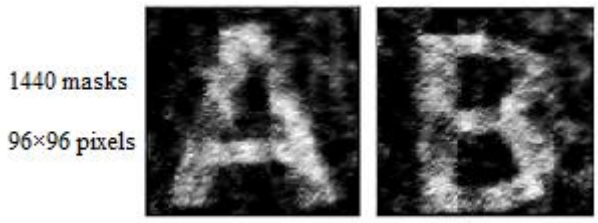

Figure.4.15 Reconstructed images from two sets of 1440 measurements using the spinning disk respectively. The original images were letter 'A' and 'B'. The size of these two images was 96×96 pixels.

The quality of the reconstructed images was about the same as those obtained using the projector system. A group of measurements have been done to study the performance of the spinning disk in terms of resolution. The four samples used are shown in Figure. 4.16. Pattern a) was four squares of size 1×1, 3×3, 5×5, and 7×7 pixels. Pattern b) was four straight lines whose widths are 1, 3, 5, and 7 pixels. Pattern c) was a 3-pixel-width line. Pattern d) was a 1-pixels-width line. Each pixel equals to 0.34 mm in practice. The resolutions of the reconstructed images were 96 by 96 pixels.

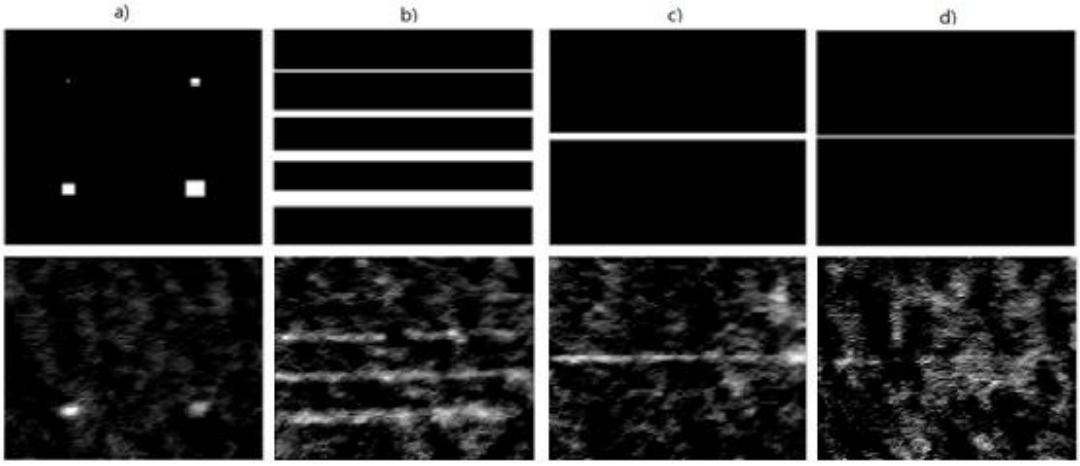

Figure.4.16 A group of patterns for resolution test of the spinning disk. Four samples from left to right: (a) Four squares of size 1×1, 3×3, 5×5, and 7×7 pixels. (b) Four straight lines whose widths are 1, 3, 5, and 7 pixels. (c) A straight line with 3-pixel-width. (d) A straight line with 1-pixels-width.

The full width at half maximum (FWHM) of the 1-mm-wide line pattern (showed in c) of Figure.4.16), after taking into consideration of the line spread function (LSF), was found to be 1.0 mm and 1.1 mm for the reconstructed image using the simulated and measured signals respectively (illustrated in Figure.4.17).

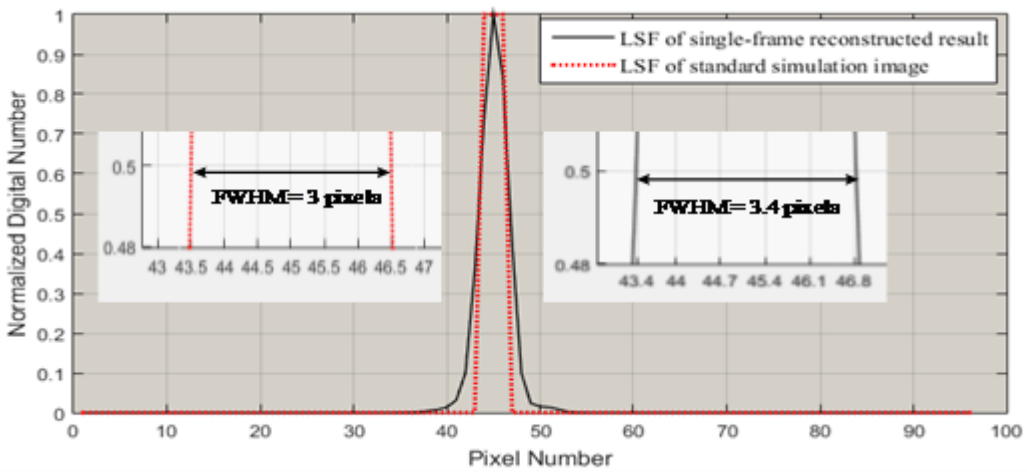

Figure.4.17 LSF curve and FWHM calculation of the 1-mm stripe sample.

The achieved resolution was 1.1 mm which was better than the 2 mm diameter of the circular pattern. As the physical holes cannot be fabricated too small (scattering and diffraction effects need to be considered), the spinning disk performed well in terms of resolution.

4.5. Video rate compressive sensing imaging system

4.5.1 Setup of Video Rate Compressed Imaging System

The schematic diagram of a video rate compressed imaging system is shown in Figure. 4.18. An infrared LED was used as the light source and a single point photodiode was used as the detector. The light from the LED was collected by a parabolic mirror and then travelling through the sample and the spinning disk. Then the light was focused onto the detector by another parabolic mirror. The parallel light can only travel through a fixed rectangular effective imaging window. The disk was mounted on a high speed electric motor and the samples were set on another slower rotating disk. The effective imaging window was 33 × 33mm. During the imaging process, the disk and the samples were rotated continuously and automatically. The samples were driven by a relatively slow motor with a rotating speed of 4 rounds per minute. In contrast, the spinning disk was driven by a high-speed electric motor with a rotation speed of up to 600 rounds per minute. In order to synchronize the spinning disk

position with the continuously data acquisition process, a pair of laser diode and photodiode were used. The light beam from the laser diode propagates through the square holes on the edge of the spinning disk which provides a precise mechanism for synchronization.

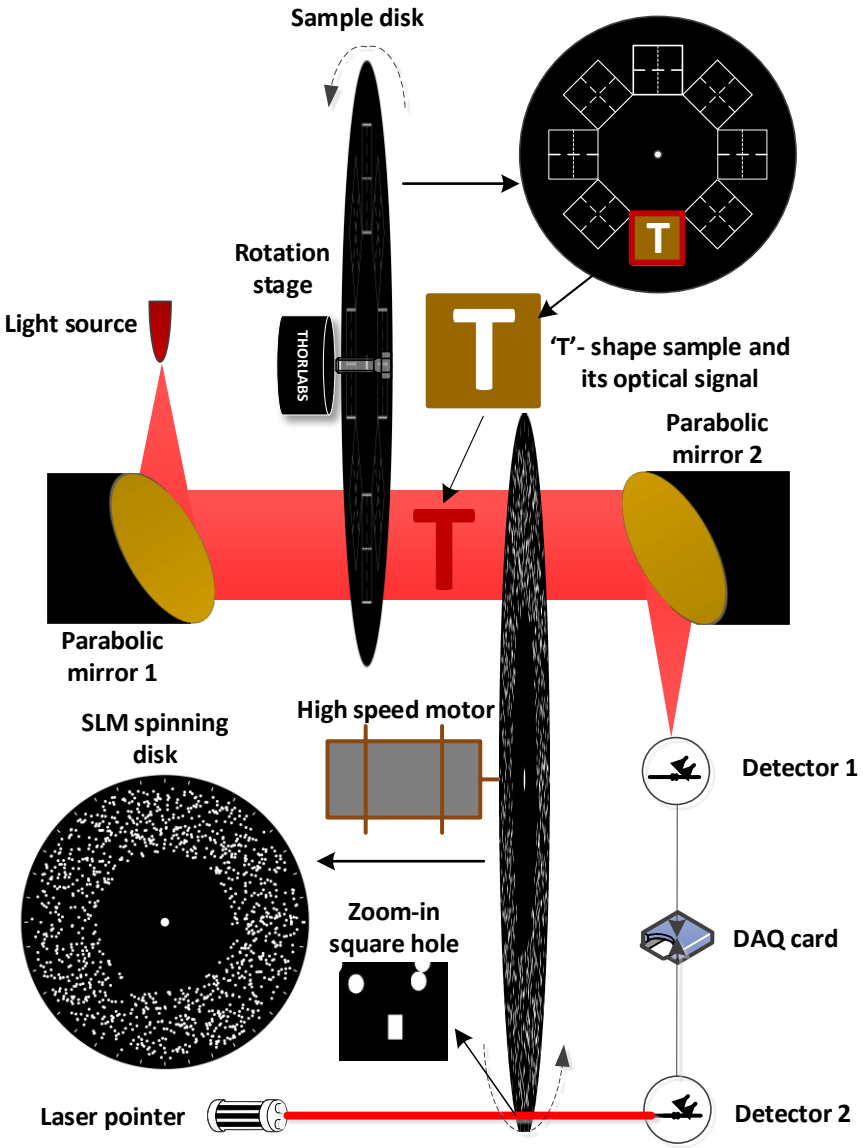

Figure.4.18. Video rate compressed imaging system using the spinning disk.

4.5.2 Experiments results

Unlike compressed imaging of single frame signal, the video rate compressed imaging increases the computational burden on reconstructing the image sequences so require more efficient processing strategy. The MMSE [176] was used as reconstruction

algorithm after balancing the reconstructed quality and time cost. Gaussain pyramid was used for re-sampling the digital masks from the spinning disk. Spline interpolation was used for obtaining the measurement signal from original sampling signal [230]. Wiener filter was applied to reduce the noise in the reconstructed images [231].

The tested samples were Chinese characters made by cut-through copper tape. The area occupied by the characters was 100% transparent to the light whilst all other areas were opaque to the light. The high-speed motor was set to rotate at its maximum rotation rate of 600 rounds per minute, corresponding to an image acquisition speed of about 10 frames per second. The resolution of these reconstructed images was 96 × 96 pixels and each image was reconstructed using 1200 measurements (e.g., a sampling rate of 13%). A group of images extracted from a video stream is shown in Figure.4.19. The moving samples were imaged and displayed in real time when they move across the sampling window, demonstrating the video rate imaging capability of the proposed system.

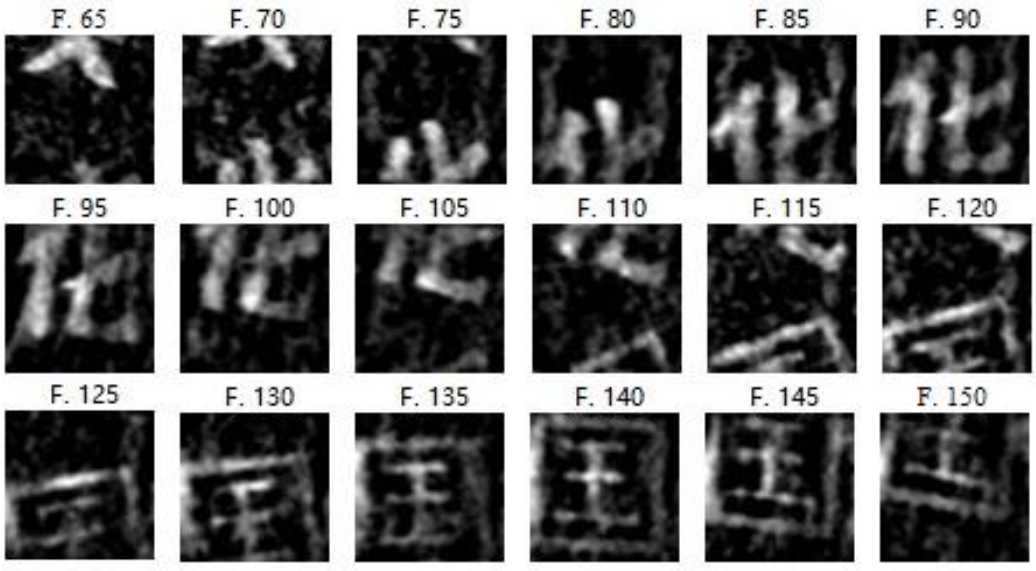

Figure.4.19 Reconstructed images of two moving samples which were two characters in Chinese. As an example, 18 frames were selected from 248 IR image sequences. Each image had 96×96 pixels and was reconstructed from 1200 measurements by using the spinning disk.

4.6. Summary

A spinning disk with circle pattern as sampling operator for CS THz imaging was proposed in this chapter. Compared with the existing one fabricated on a PCB board, the new spinning disk was fabricated on a piece of steel plate, so no substrate was needed. This not only increases the intensity of THz signal transmit through the disk but also minimizes the noise caused by the un-uniform THz absorption of the substrate.

THz radiation spans a frequency range from 300 GHz to 10 THz (wavelength is from 1mm to 30um). Thus, when the size of the sampling operators on the existing (1 mm diameter squares) disk was close to the wavelength of THz radiation, the scattering and the diffraction effects can no longer be negligible. The scattering effect of THz radiation at the sharp corners also degraded the overall signal to noise rate. These all added noise to the imaging procedure and affected the encoding accuracy thus weakening the quality of the reconstructed images. For the new designed spinning disk, a number of 2 mm diameter holes were chemically etched on this steel plate randomly. Each hole was 100% transparent to light while the stainless steel was 100% opaque to light. The size of the round holes on the disk was relatively larger than the square hole in the early designed disk so the performance against diffraction and scattering effects were better.

The sampling operators on the disk could be considered as a Toeplitz block matrix. The reconstruction quality achieved by using the spin disk measurement matrix (nearly block Toeplitz matrix) was close to the level of the well-proved CS matrices such as random matrix. A resolution of better than 2 mm had been achieved with the 2 mm diameter circular pattern masks.

Before applying the spinning disk in THz imaging system, the imaging quality of the spinning disk was validated using the infrared CS imaging system. The parabolic mirrors, spinning disk and the samples used in the infrared system were the same as in

a THz system so the results should be more convincing. Another benefit was the wavelength of infrared was closer to that of THz so the scattering and diffraction effects in the infrared system were more similar to those in a THz system. A video rate CS imaging system has been adapted using infrared CS set up and the spinning disk as well. An image acquisition speed of about 10 frames per second at 96 by 96 pixels resolution was achieved.

Chapter 5

Block based compressive sensing imaging using spinning disk

5.1. Motivation of block based CS imaging

For high resolution imaging, the number of measurements needed is large. This makes the imaging process slower since the measurement time is long. At present, the reconstruction process of CS suffers huge computational expense and large memory for storage, hence increasing the reconstruction time. To further increase the imaging speed, Dr Gan et al. [232] introduced the concept of block compressed sensing. In this chapter, block based CS will be demonstrated by applying the set of 1440 masks captured from the spinning disk.

The imaging speed could be increased by breaking the original image into blocks then measuring and reconstructing these blocks independently and in parallel. A group of simulations have been done to verify the capability of the set of 1440 masks in block based CS. The original pattern (a character 'A'.) and masks were divided into 4 equal size blocks. Each block of the image was measured and reconstructed using one block of the masks respectively. The reconstructed images according to different sampling rates are shown in Figure.5.1. The resolution of each block was 48 by 48 pixels so the resolution of each complete image was 96 by 96 pixels.

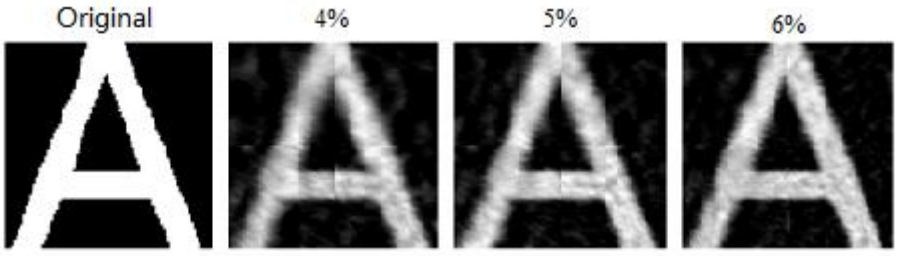

Figure.5.1 Simulation results of 4 blocks CS imaging according to sampling rates 4%, 5% and 6%. The original image was broke into 4 equal size blocks and each block was measured and reconstructed separately and simultaneously. The resolution of each block of the reconstructed images is 48 by 48 pixels. The total resolution of the reconstructed images is 96 by 96 pixels.

5.2. Analysis of block CS imaging using one set of data measured on the projector based system

To further validate the block based CS idea, a 4 block photodiode was applied in the existing projector CS system. The experiment set up is the same as the one showed in Figure. 3.17 except the detector used here was a four block detector array. The image projected was collected by a lens set and focused onto the detector. Each element of the detector works independently and in parallel (each detector senses one block of the original image).

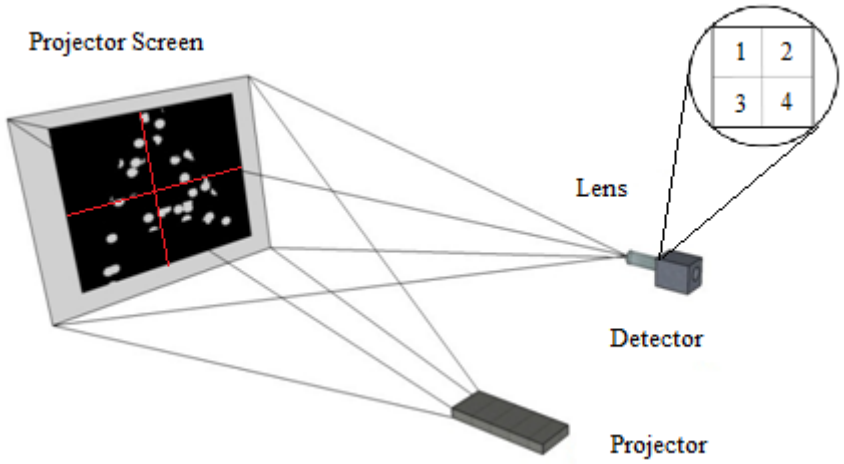

Figure.5.2 Four block projector CS imaging system. The images of a masks covered by a pattern "A" was projected onto the projector screen. The masks showed in sequence and the images were collected by a lens and focused onto the 4 block photodiode detector. The data from the detector were used for reconstruction.

One set of 1440 measurements were taken on the projector based system using the set of 1440 masks from the spinning disk discussed in Chapter 4. The experiment procedure was the same as discussed in Chapter 3.3. The original pattern measured was a character 'A'. The simulation and reconstructed images obtained using the first 360 data points (equals to 4% sampling rate) are shown in Figure.5.3. Each block of the image was measured and reconstructed independently and in parallel. The resolution of each block was 48 by 48 pixels so the complete image size was 96 by 96 pixels.

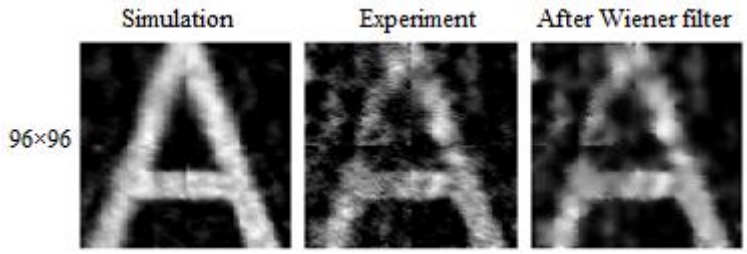

Figure.5.3 Simulation and experiment block CS imaging results of 96 by 96 pixels images using the 4 sets of 360 data points. The original image was broke into 4 blocks and each block was measured and reconstructed separately and simultaneously. Each block was 48 pixels by 48 pixels and was reconstructed from 360 measurements. Wiener filter was applied to enhance the imaging quality.

Wiener filter is suitable to reduce random noises and was introduced here to reduce the noise in the measurements. As can be seen from Figure.5.3, the quality of image processed by wiener filter was better. More quantified comparisons can be seen in Table.5.1. The comparison of the 360 measured data points and the simulation data points of each block in Figure.5.3 are shown below.

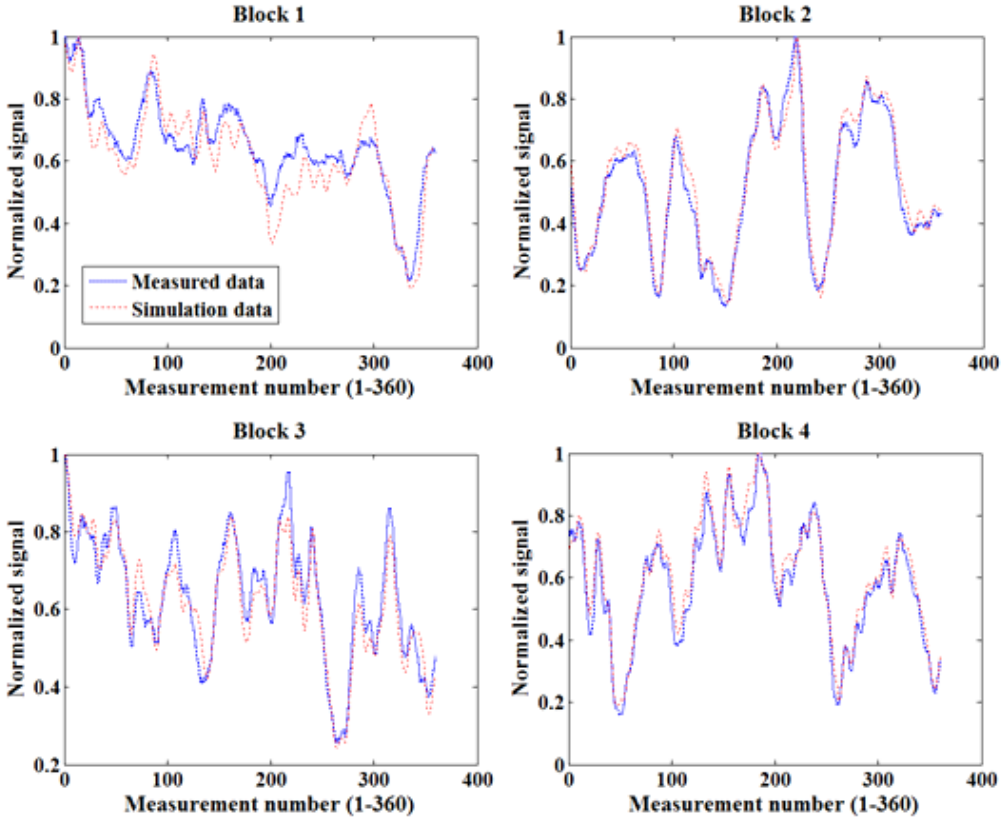

Figure.5.4 Comparison between simulation and measured data of the 4 blocks showed in Figure.5.3. The red ones were the simulation data and the blue ones were the measured data. 1440 measurements were taken and the first 360 data points were used to reconstruct the 4 blocks.

By using this block based method, the speeds of measurement and reconstruction process were significantly increased. Most parts of the measured data and simulation data were matched. The simulation and measured results could show fundamental characters of the original image. The noise in the measurement process was mainly from the electric circuit. The single point detector used before was a commercial one with built in amplifier circuit, while the detector array here was very basic. All the amplifier circuit components were set up on bread board which increased the electric noises. By applying wiener filter, most of these noises could be filtered out.

Another noise source was the environmental light noise. The detector was extremely sensitive. The effective wavelength of the photodiode covered both the infrared and visible range. Although the measurements were taken with light switched off, any other light source nearby the detector, both visible and infrared ones (such as light from a computer screen, heat from instrument or human body), were added to the noise.

Quantified evaluations of these reconstructed images are shown in Table.5.1. The evaluation parameters used were Peak Signal-to-Noise Ratio (PSNR), Structural Similarity (SSIM) index, Mean Structural Similarity (MSSIM) and Feature Similarity (FSIM) index.

Table.5.1 Quality evaluations of the three 96 by 96 pixels images reconstructed according to block CS using the spinning disk as shown in Figure.5.3.

	PSNR	SSIM	FSIM
Simulation	13.74	0.87	0.44
Experiment	9.35	0.58	0.33
Wiener filter	9.96	0.64	0.40

The set of 1440 96 by 96 pixels masks captured from the spinning disk were converted to 192 by 192 pixels mathematically. Images of size 192 by 192 pixels were reconstructed using these upgraded masks and the same sets of 1440 measurements data. The simulation and reconstructed images obtained using the 1440 data points (equals to 4% sampling rate) were shown in Figure.5.5. The resolution of each block was 96 by 96 pixels so the complete image size was 192 by 192 pixels.

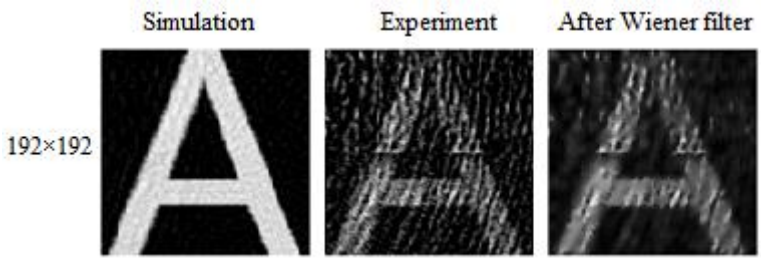

Figure.5.5 Simulation and experiment block CS imaging results of 192 pixels by 192 pixels images using the 4 sets of 1440 data points. The original image was broke into 4 blocks and each block was measured and reconstructed separately and simultaneously. Each block was 96 pixels by 96 pixels and was reconstructed from 1440 measurements. Wiener filter was applied to enhance the imaging quality.

Since the images were reconstructed from the same sets of 1440 measurements, the signal to noise ratio of the two different resolutions (96 by 96 pixels and 192 by 192 pixels) should be the same. However, the qualities of images showed in Figure.5.3 were better than that showed in Figure.5.5. More quantified evaluations of these reconstructed images are shown in Table.5.2. The comparison of the 1440 measured and the simulation data points of each block in Figure.5.5 are shown below.

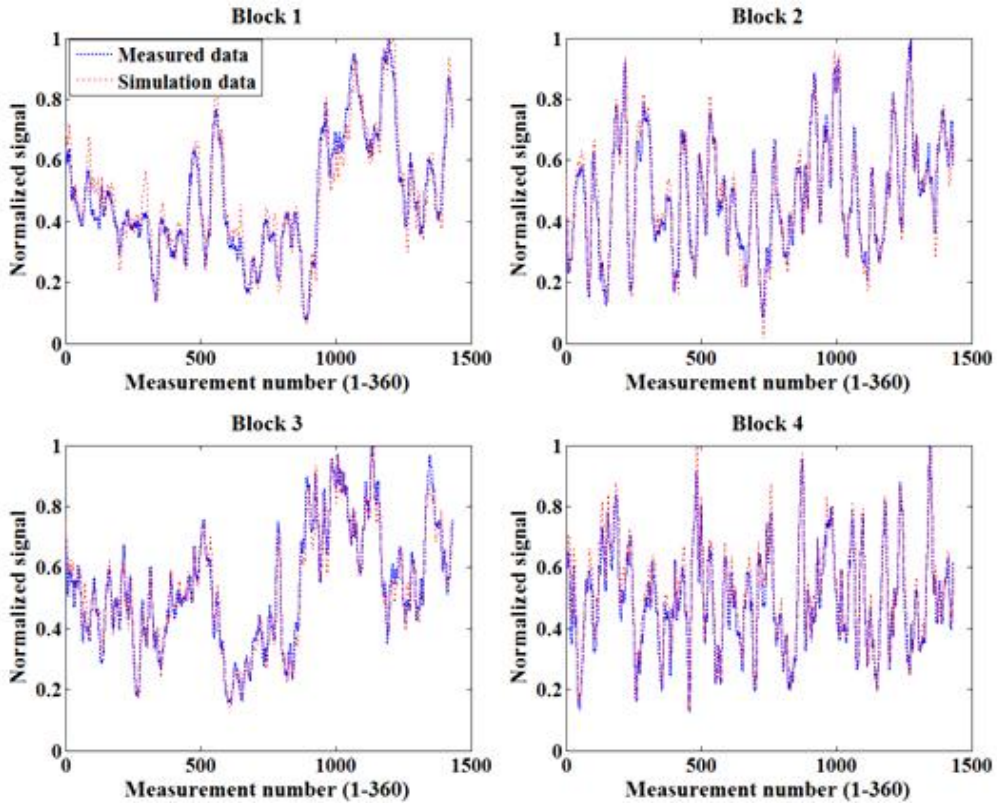

Figure.5.6 Comparison between simulation and measured data of the 4 blocks showed in Figure.5.5. The red ones were the simulation data and the blue ones were the measured data. 1440 measurements were used to reconstruct the 4 blocks.

Table.5.2 Quality evaluations of the three 192 by 192 pixels images reconstructed according to block CS using the spinning disk as shown in Figure.5.5.

	PSNR	SSIM	FSIM
Simulation	17.84	0.95	0.60
Experiment	7.39	0.32	0.26
Wiener filter	8.12	0.39	0.47

By adding the 4 sets of 1440 data from 4 blocks together as one set of data, a 96 by 96 pixels image was reconstructed as a complete image using the set of 1440 96 by 96 masks (equals to 15% sampling rate). The comparison of the 1440 measured data points and the simulation data points is shown below in Figure.5.7. The simulation and reconstructed results according to these data points were also shown in Figure.5.7.

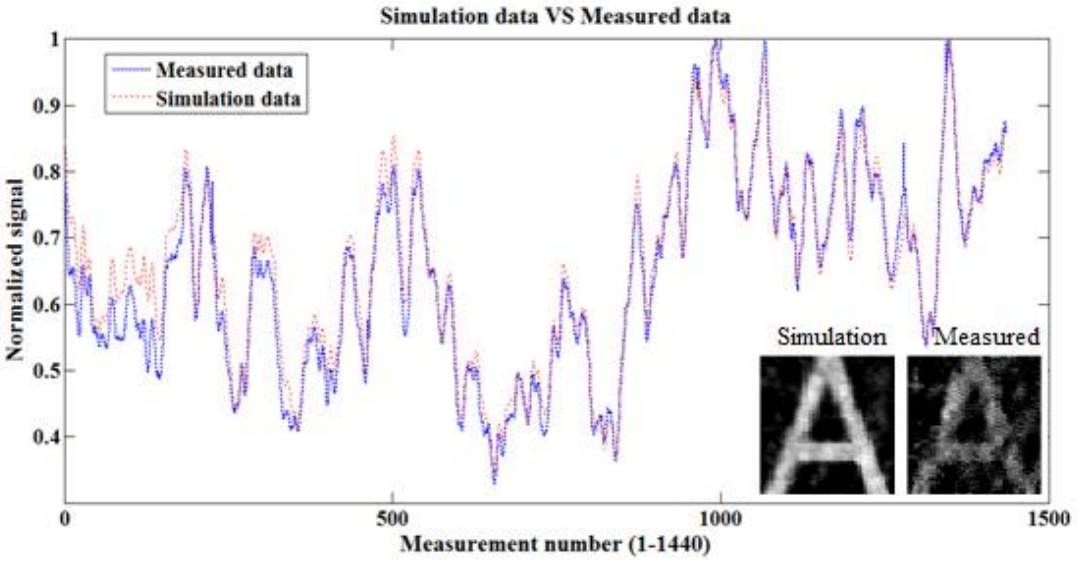

Figure.5.7 Comparison between the simulation and measured data after added up the 4 sets of 1440 data points to one set. The red ones were the simulation data and the blue ones were the measured data. Both of them were normalized. The two 96 by 96 pixels images were reconstructed according to simulation and measured data points.

The data points showed in Figure.5.7 were measured separately and then added up together. The image reconstruction according to these data points can be considered as normal CS approach and the qualities were still good. The images obtained from simulation and experiment using CS and block CS approaches were compared in Figure.5.8. The block CS parts were the same as shown in Figure.5.3 and the CS parts were the same as shown in Figure.5.7.

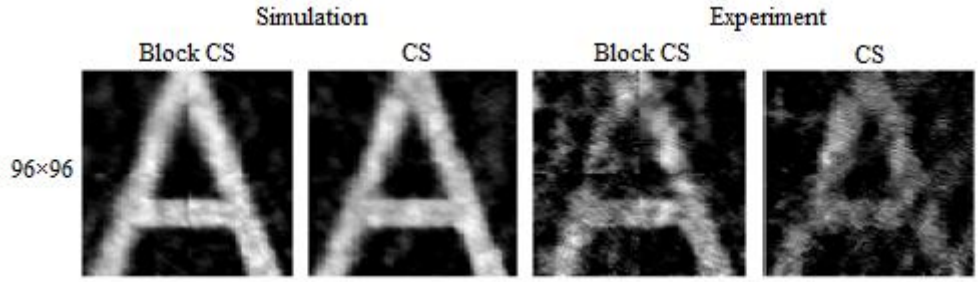

Figure.5.8 Comparisons of images reconstructed from same sets of measurements according to block CS and CS. In the block CS part, each block was 48 by 48 pixels and was reconstructed from 360 measurements separately. In the CS part, the data from the 4 blocks were added up and was reconstructed as a complete image from 1440 measurements. All the images were 96 by 96 pixels.

The imaging quality of CS and block CS were about the same while the sampling rate of block CS was much lower. Quantified evaluations of these reconstructed images were shown in Table.5.3. The image quality achieved using CS and block CS was about the same. The images using CS approach were reconstructed using 96 by 96 pixels masks. In the block CS approach, the images were reconstructed by breaking the same 96 by 96 pixels masks into 4 parts.

Table.5.3 Comparisons of quality evaluations of the four 96 by 96 pixels images reconstructed according to CS and block CS as shown in Figure.5.8.

	Simulation		Experiment	
	Block CS	CS	Block CS	CS
PSNR	13.74	13.19	9.35	8.05
SSIM	0.87	0.85	0.58	0.40
FSIM	0.44	0.48	0.33	0.35

The data used to reconstruct images showed in Figure.5.3, Figure.5.5 and Figure.5.7 were the same sets of 1440 data points. The noise in the measurement process was the same while the quality of these images was not the same due to different reconstruction approaches and resolutions. The simulation results for all resolutions were good but for experiment results, the qualities of 96 by 96 pixels images were much better than 192 by 192 pixels image. Reconstruction process for images of lower resolution was more tolerant to noises from the measurement process.

In practice, due to the computation ability of a PC, 1440 masks were the maximum number of masks can be obtained from one round of the spinning disk, so the

sampling rate can't be increased further here. A comparison of normal CS and block based CS in terms of number of measurements needed and reconstruction time was shown in the table below. The number of measurements and time for reconstruction needed was much less by block CS approach than normal CS imaging.

Table.5.4 Comparisons between CS and block based CS in terms of number of measurements needed and time of reconstruction process needed for the same size of image.

Image size	48 by 48 pixels		96 by 96 pixels		192 by 192 pixels	
	Number	Time	Number	Time	Number	Time
CS	360	1.5s	1440	28s	N/A	N/A
Block CS	86	0.6s	360	6s	1440	112s

5.3. Experiment using the spinning disk designed for THz imaging

The idea of block CS imaging using the spinning disk was developed for THz imaging. There was no sensitive THz detector array at present, so the experiment was carried out on the infrared system. Before applying in THz system, the imaging quality was always checked using the infrared CS imaging system because the parabolic mirrors, spinning disk and the samples used in the infrared system were the same as in a THz system so the results should be more convincing. Another benefit was the wavelength of infrared was closer to that of THz so the scattering and diffraction effects in the infrared system were more similar to those in a THz system.

The experiment set up was the same as the one shown in Figure. 4.13 except the detector used here was a four block detector array. The 2 x 2 detector array was the same as the one shows in Figure. 5.2. Each detector works independently and in parallel. The system worked in a rotate-stop-measure routine. Every step the disk rotates 0.25 degree and the detector takes a measurement. 1440 measurements were taken for one round in total.

The original pattern and the reconstructed images obtained using the first 720 data points from the 1440 measurements (equals to 8% sampling rate) were shown in Figure.5.9. Each block of the image was measured and reconstructed independently

and in parallel. The resolution of each block was 48 by 48 pixels so the complete image size was 96 by 96 pixels. The physical pattern was made from cutting through copper tape.

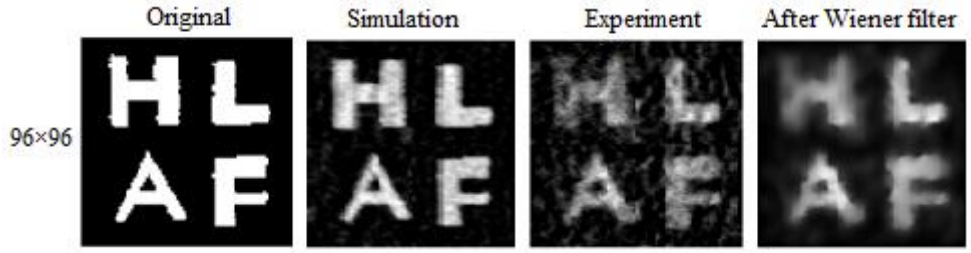

Figure.5.9 Simulation and experiment block CS imaging results of 96 pixels by 96 pixels images using data measured with the spinning disk. The original image was broke into 4 blocks and each block was measured and reconstructed separately and simultaneously. Each block was 48 pixels by 48 pixels and was reconstructed from 720 measurements. Wiener filter was applied to enhance the imaging quality. The effective window was 33 mm by 33 mm.

The comparison of the 720 measured data points and the simulation data points of each block in Figure.5.9 were shown below.

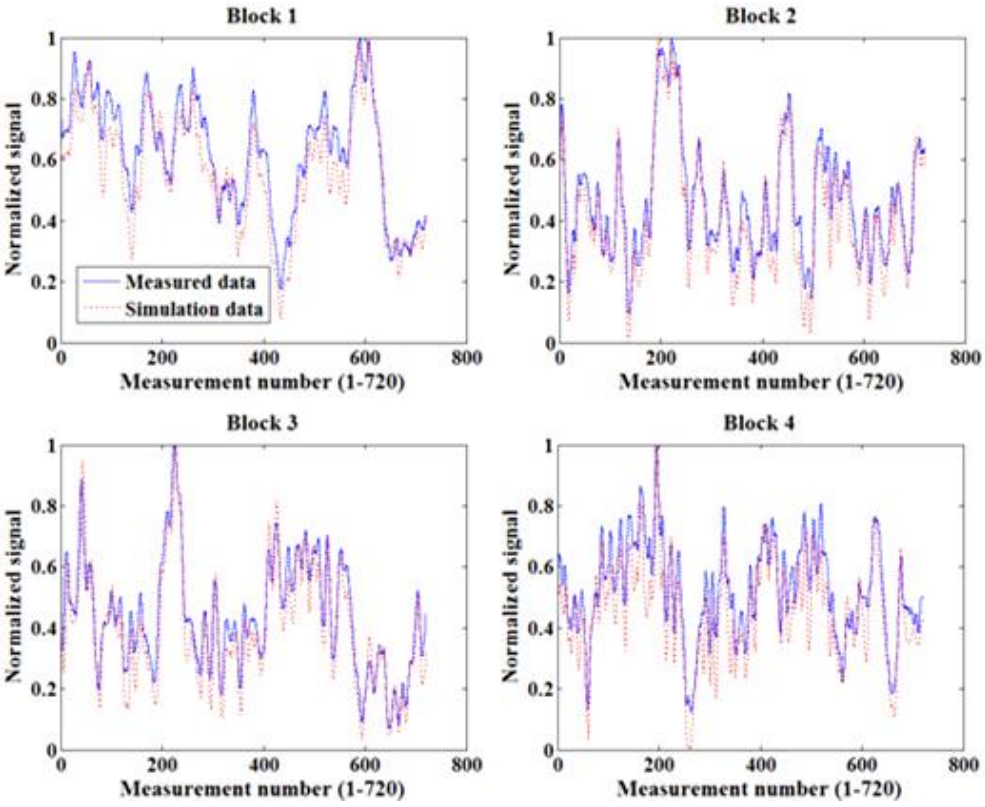

Figure.5.10 Comparison between simulation and measured data of the 4 blocks shown in Figure.5.9. The red ones were the simulation data and the blue ones were the measured data. 1440 measurements were taken and the first 720 data points were used to reconstruct the 4 blocks.

According to the simulation results, 360 measurements (equals to 4% sampling rate) should be enough to reconstruct a 96 by 96 pixels image. While in this case, 720 measurements (equals to 8% sampling rate) were needed due to the low signal to noise ratio. The sampling rate needed was still much lower than conventional CS. More quantified evaluations of these reconstructed images are shown in Table.5.5.

Table.5.5 Quality evaluation of the three 96 by 96 pixels images reconstructed according to block CS using the spinning disk as shown in Figure.5.9.

	PSNR	SSIM	FSIM
Simulation	16.58	0.91	0.56
Experiment	11.09	0.63	0.34
Wiener filter	11.71	0.69	0.52

5.4. Summary and Future work

The concept of block CS was demonstrated using the THz spinning disk and a 2x2 sensor array. For high resolution CS imaging, due to the high number of measurements needed and the huge computational expense and large memory for storage which the reconstruction process suffered, the imaging process was slow. The imaging speed was further increased by breaking the original image into blocks then measure and reconstruct these blocks independently and in parallel. In the experiment set up, each element in the sensor array worked in parallels thus both the data acquisition and image reconstruction speeds have been increased.

Until now there was no sensitive THz detector array so some experiments were carried out on the infrared system. The results showed that the spinning disk worked well with the block CS concept. This give the disk a potential in block THz CS imaging once suitable THz sensor array is fabricated in the future.

Chapter 6

Compressive sensing THz imaging

6.1. CS THz imaging using an ultra-strong THz beam on food samples

Darebury Lab is part of the Science and Technology Facilities Council (STFC), which provides a collaborative and innovative environment for scientists, researchers and industry to perform cutting-edge research. STFC is one of Europe's largest research organizations and keeps UK's science research, technology development and innovation at the top class of world. Daresbury Laboratory leads world scientific research in fields such as accelerator science, bio-medicine, physics, materials, engineering and computational science [233].

To study the imaging properties of THz beam penetrating food samples, some CS imaging experiments using the ultra-strong pulse THz beam from the particle accelerator in Daresbury Lab have been done. The power of THz radiation in normal labs is not strong enough to transmit through food samples. The picture below shows the particle accelerator hall.

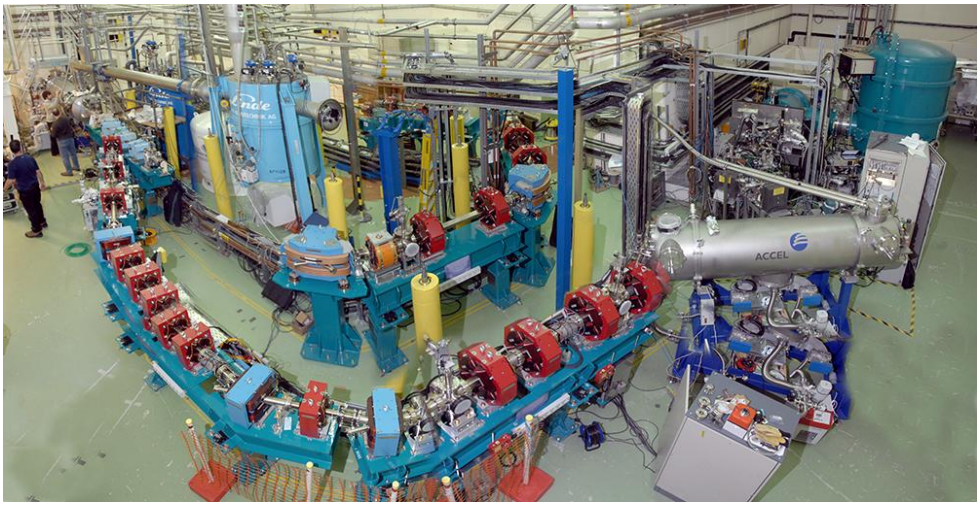

Figure.6.1 Picture of the particle accelerator hall. [234]

6.1.1 Experiment set up

Once the accelerator was switched on, the radiation in the accelerator was extremely strong; therefore nobody was allowed to enter the accelerator hall when it's switched on. In fact, there were strict searching rules to follow before switching the machine on to make sure nobody was inside the radiation area.

Since THz and IR radiations were less harmful to human body, they were guided out of the accelerator hall to a diagnose room. These two rooms were separated by very thick walls to avoid radiation hazards from other wavelengths. The THz and IR beams were distributed from the accelerator hall to the diagnose room in a metal tube of diameter 6 inches. Below is a schematic diagram shows how the THz beam was distributed. The red box illustrates the diagnose room and the green box illustrates the accelerator hall.

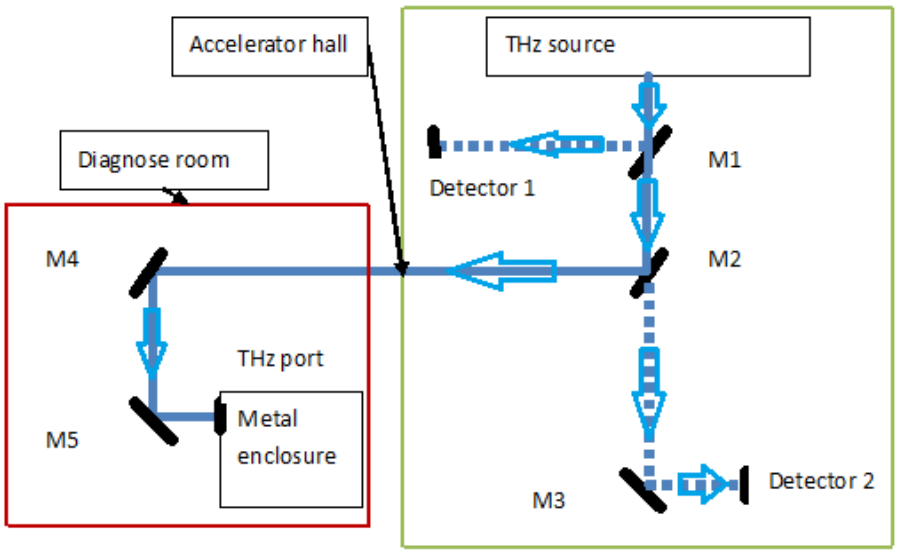

Figure.6.2 Schematic diagram show how the THz beam was distributed from the accelerator hall to the diafnose room. The blue solid lines are the THz beam and the blue dash lines shows the calibration routine. Detector 1 and 2 were used to calibrate the direction and strength of the THz beam. The red box illustrates the diagnose room and the green box illustrates the accelerator hall.

Mirror 1 and mirror 2 were on a moveable stage. When the diagnose room was working, mirror 1 should be moved away from the beam line and mirror 2 was moved in. The beam line was reflected twice by mirror 4 and mirror 5, and then came into the THz beam port in a metal enclosure.

When the power of the THz source needed to be optimized, mirror 1 was moved in to direct the beam to detector 1 to check the signal power. After that, mirror 1 was moved away from the beam line to distribute the THz beam to the diagnose room.

After a long time of operation, the direction of the beam from the source normally changed. So mirror 1 and mirror 2 need to be moved out from the beam line to let detector 2 checks the signal direction. By comparing the signal strength measured by detector 1 and detector 2, the direction of the beam line was optimized.

The THz beam travelling out of the port could be assumed as parallel wave since it had travelled a long way from the accelerator hall to the diagnose room. The repetitive rate of the THz pulses was 100Hz. The beam from the particle accelerator was quite strong so the beam was distributed into a metal enclosure as a way of protection. There was a shutter at the end of the distribution tube inside the metal enclosure. For safety reasons, once the door of the enclosure was opened, either for experiment operation or by accident, the shutter would close automatically to stop the beam.

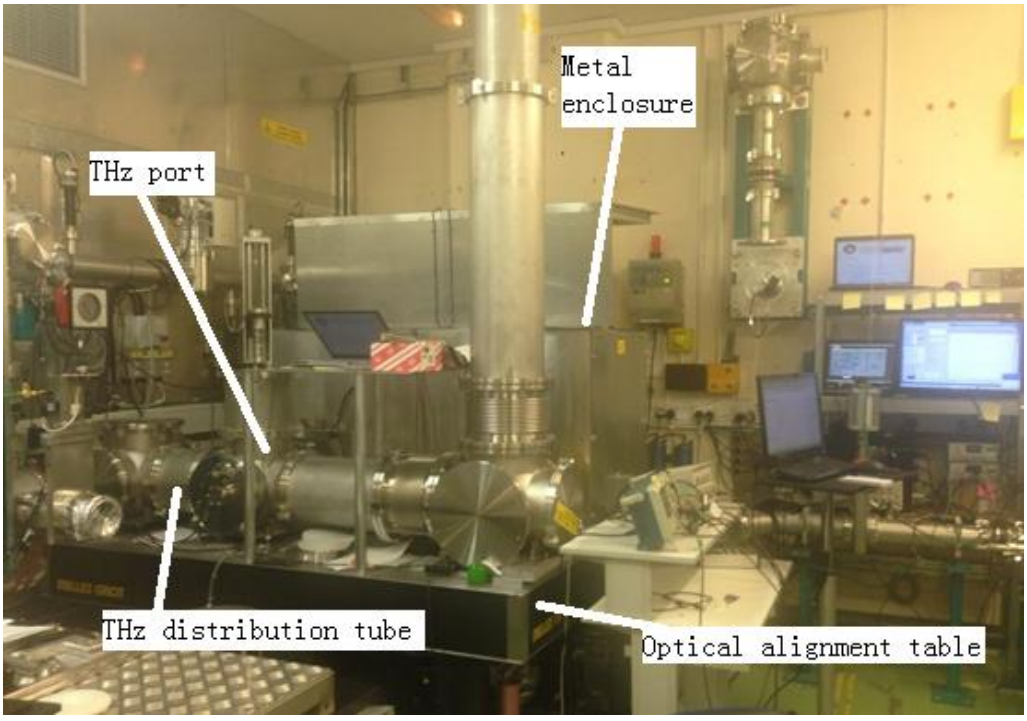

Figure.6.3 Picture of the diagnose room.

The Terahertz beam was focused onto a pyro electric detector by a parabolic mirror of diameter 6-inches. The power of the Terahertz beam was quantified by the voltage measured on the detector. The spectral distribution of the Terahertz power was measured by insertion of different band pass Terahertz filters on a suitable location between the parabolic mirror and detector. The results are shown in Table.6.1.

Table.6.1 The spectral distribution of THz power in terms of detector voltage. These data were measured by insertion of band-pass terahertz filters.

Pass frequency	All frequency	660GHz	345GHz	270GHz	150GHz	90GHz
Voltage (Volts)	2.2	0.093	0.097	0.187	0.115	0.110

A more clear view of the spectral distribution of the THz pulses can be seen in the bar chart below. The central wavelength was around 270GHz.

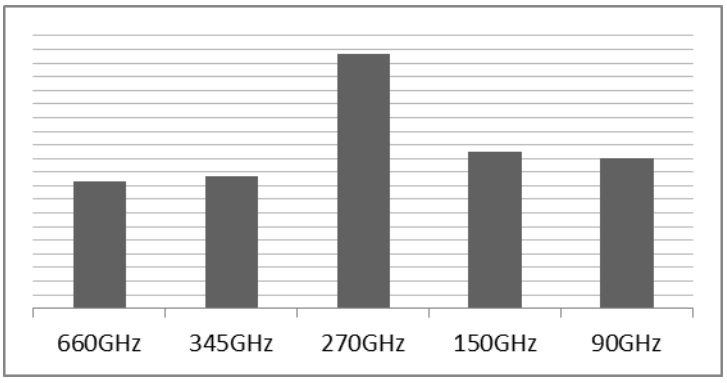

Figure.6.4 Spectral distribution of the THz pulse power in Daresbury Lab. The x axis indicates the band-pass frequencies. The y axis indicates the terahertz beam power.

6.1.2 Manual CS experiment using the set of 40 masks for food sample

In this section, the set of 40 optimized masks showed in Figure. 3.6 were used. All the masks were made by cutting through copper film, which was 100% opaque to THz beam. The masks and samples were inserted in a suitable location between the PM and the pyro electric detector. The size of the effective image window was 33 × 33 mm. For each measurement, the mask was changed manually. This process took about 3 minutes including a sequence of work: close the beam shutter, open the enclosure, change the mask, close the enclosure, and open the beam shutter and measure. The 40 measurements took about 2 hours to accomplish.

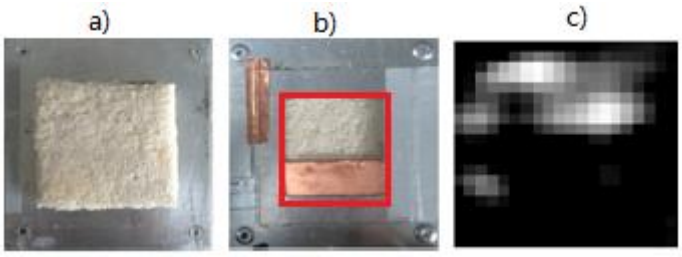

Figure.6.5 Photo of sample for manual THz CS imaging experiment and its reconstructed image. a) and b) were photos of the two sides of the sample. The simple copper pattern was used to block terahertz beam. The sample was a piece of bread. The red box shows the imaging window. c) was the reconstructed image from measurements using the 40 masks. The resolution was 20 by 20 pixels.

The comparison between the measured data and simulation data of samples in Figure.6.5 is shown below:

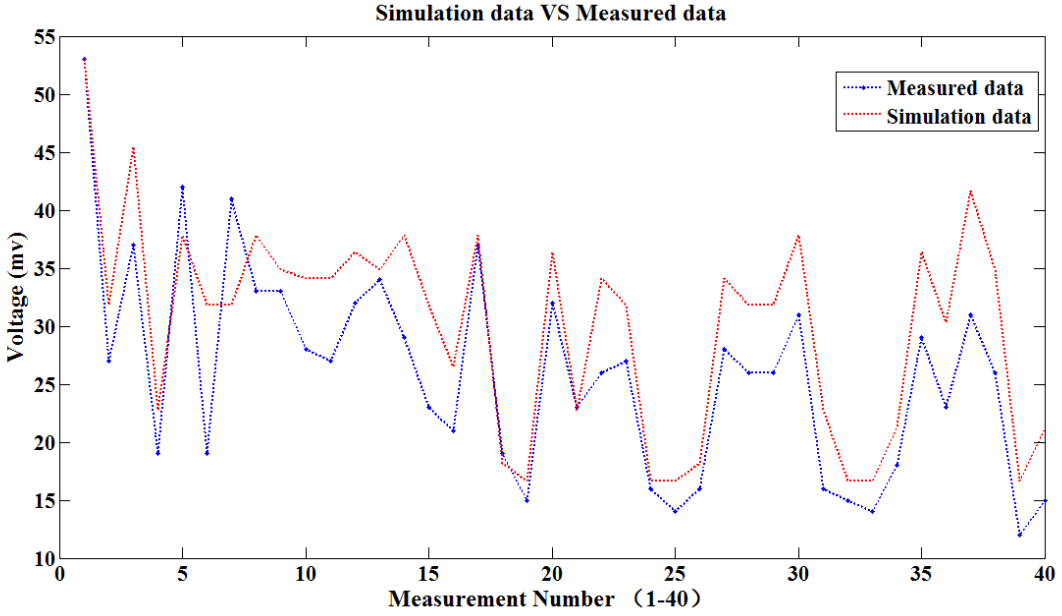

Figure.6.6 Comparison between the simulation data and measured data of the 40 measurements used in Figure.6.5. The red points were the simulation data and the blue points were the measured data. The x axis is the number of measurement. The y axis is the voltage measured by the detector.

The simulation data was calculated by assuming that the bread was 100% transparent and the copper tape was 100% opaque to the terahertz beam. This image was not good due to low signal to noise ratio. A long time drift of the beam power can be seen during the second half of the measurements. The average THz beam power dropped to about 30mv after insertion of the masks and sample, which was much smaller. This contributed to the low signal to noise ratio. Another reason might be the long term drift of the beam power during the long measurement time (2 hours).

6.1.3 Automatic CS experiments using the spinning disk for food sample

To increase the imaging speed, the spinning disk set up was introduced. The set up is shown in Figure.6.7. The THz beam travelling out from the THz port was collected by the 6 inches parabolic mirror and focused onto the pyro electric detector. The spinning disk and sample stage was inserted between the parabolic mirror and the detector. The distance between the sample stage and detector was calculated according to the size and focus length of the parabolic mirror, to make sure all the beam travel through the sampling window can be collected by the detector.

The spinning disk here was the same one discussed in Chapter 4. The system worked in a stop-measure-rotate routine. Every time the disk rotated 1 degree and the detector take measurement for 1 second. During this 1 second, 100 THz pulses were measured and added up. In total, 360 measurements were taken for each sample and 360 peak values were recorded. A 48 by 48 pixels image can be reconstructed from these 360 measurements. The size of the effective image window was 33 mm ×33 mm.

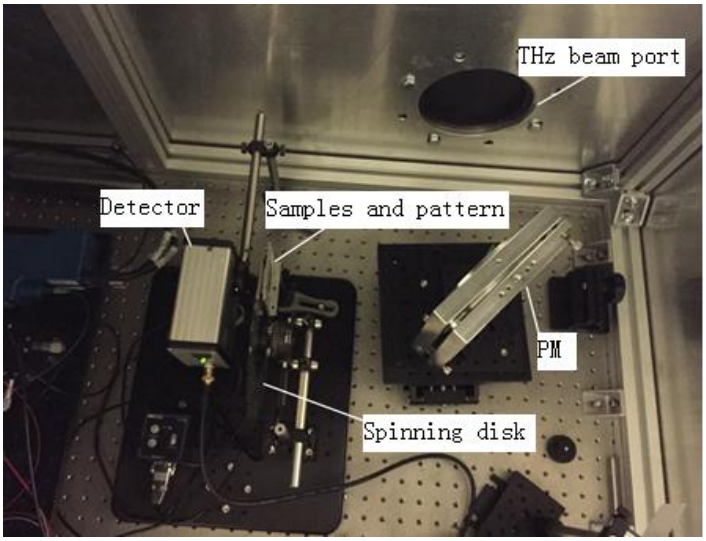

Figure.6.7 Picture of the CS imaging set up in the metal enclosure.

Two sets of data were measured when no patterns and samples were on the sample stage. The THz beam travelling through the effective sampling window the spinning disk was measured by the detector. The purpose was to check whether the beam was spatially distributed uniformly. The two sets of measurements matched well, which means the experiments were repeatable and convincing.

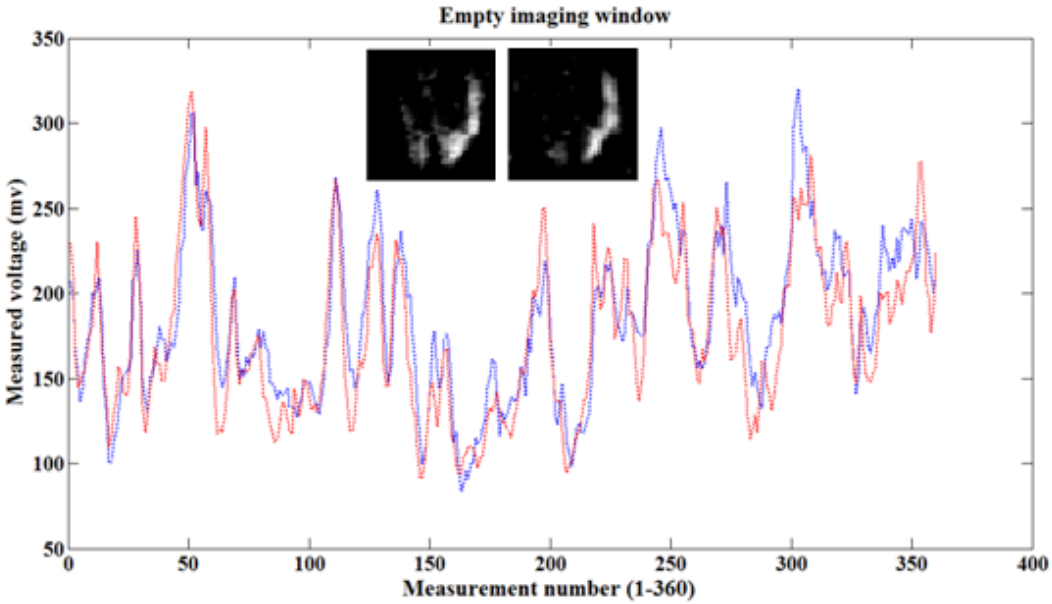

Figure.6.8 Two sets of data measured when there were no patterns and no samples in the imaging window. The two images showed were reconstructed from the two sets of 360 data points measured using the spinning disk respectively.The resolution of these two images were 48 by 48 pixels.

Two 48 by 48 pixels images were reconstructed according to the two sets of data respectively. The results show that the THz beam was not uniform. The beam strength in the center part was much stronger than the other part.

For CS imaging experiments, patterns can be chosen according to the spatial distribution of the light source to achieve better results. Two sets of measurements have been done using the pattern showed in of Figure 6.9. This pattern was chosen to utilize the stronger part of the THz beam to achieve better SNR. The silver part was made of aluminum film which blocks the THz beam and the yellow part was just paper that is transparent to THz beam. Two reconstructed images are shown below.

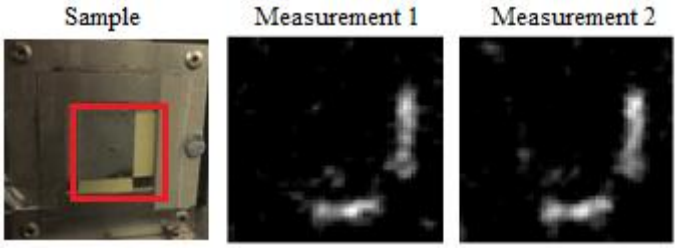

Figure.6.9 Picture of the sample and reconstructed THz images from two sets of measurements. The pattern was made from paper and aluminum film. The red box was the imaging window. The resolutions of the two images were 48 by 48 pixels and were reconstructed from two sets of 360 data points measured using the spinning disk.

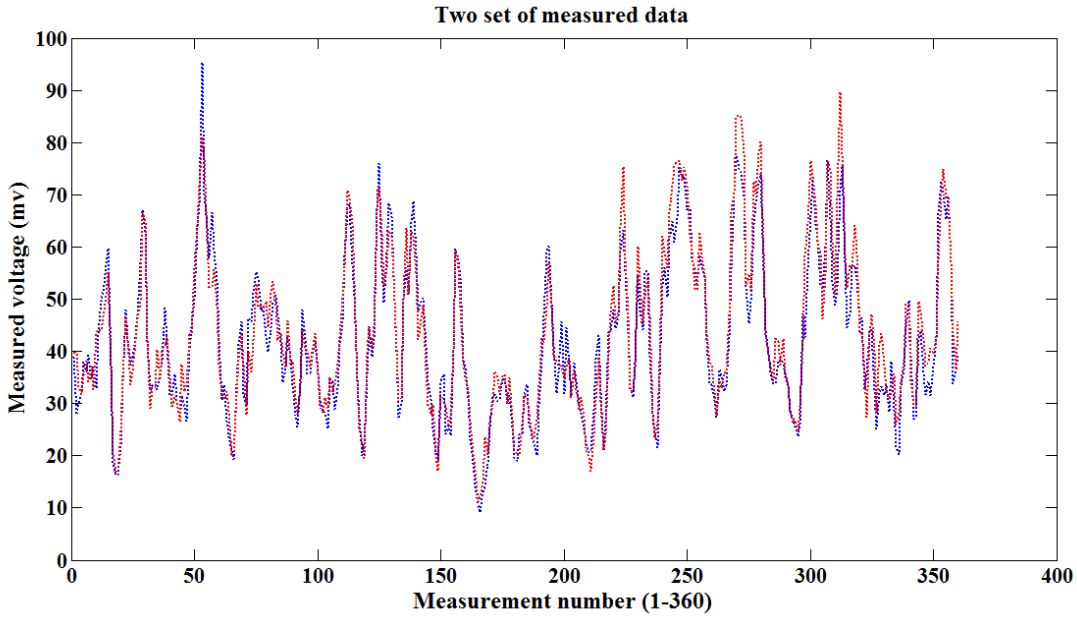

Figure.6.10 Two sets of 360 data points measured using the spinning disk for the sample showed in Figure.6.9.

The red and blue data points can be considered as matched which means the results were repeatable and convincing. The basic shape of the pattern could be reconstructed but the signal strength was too weak to apply food samples.

The direction and power of the THz source were optimized to achieve stronger beam for food samples. Another two sets of measurements had been done using different samples showed in Figure.6.11. The sample was made by cutting through copper tape. One set of measurements were taken using this sample only. The other set of measurements were taken using this sample covered by a piece of bread. The two reconstructed images using these two sets of data are shown in Figure.6.11 as well.

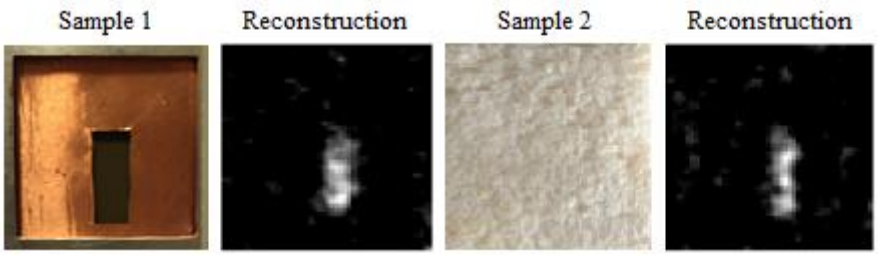

Figure.6.11 Picture of two samples and their corresponding reconstructed THz images. Sample 1 was a pattern made with copper film. Sample 2 was sample 1 covered by the piece of bread. The resolutions of the two images were 48 by 48 pixels and were reconstructed from two sets of 360 data points measured using the spinning disk.

The two sets of measured data points are shown in Figure.6.12. The shapes of the two sets of data points were about the same while the average measured voltages were different. The strength of the THz beam was decreased about 50% after insertion of the piece of bread. After insertion of the piece of bread, the signal strength decreased but the quality of reconstructed image remains. The spinning disk was capable for THz imaging even with bread samples.

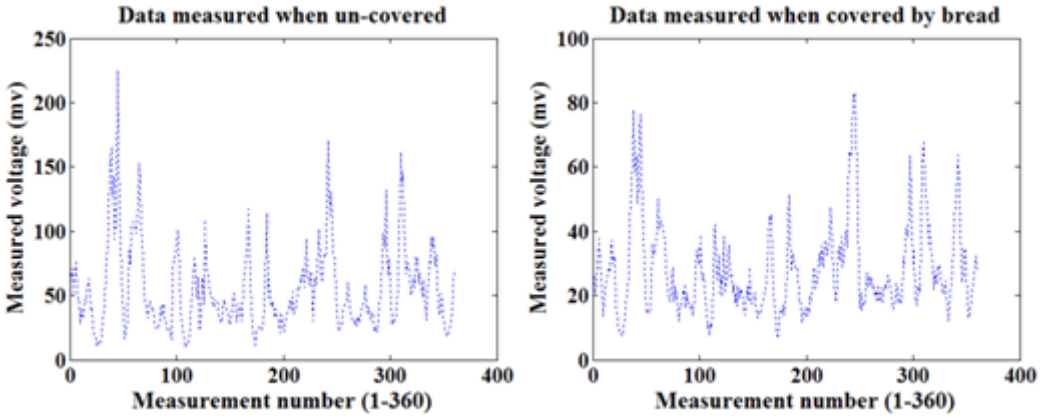

Figure.6.12 Two sets of 360 data points measured using the spinning disk for the sample 1 and sample 2 shown in Figure.6.11.

6.2. CS THz experiment on THz time-domain system

6.2.1 Experiment set up

A picture of the THz time-domain system built in our lab is shown in Figure.6.13. The THz emitter was a low-temperature-grown (LTG) GaAs photoconductive emitter with a bowtie shape antenna. The gap of the antenna was 10 um. The antenna was biased using an 11 kHz square wave of peak to peak amplitude 50 V. The THz receiver was a ZnTe electro-optic crystal [235]. The driving laser was a Ti:sapphire femtosecond laser. The whole system worked at room temperature. A schematic diagram of our system is shown in Figure.6.14.

The spinning disk configuration was applied in this typical THz time-domain system discussed in Chapter 2.13. For the CS THz imaging experiments showed in Chapter 6.2.2, the time delay stage was fixed to the peak position of the THz pulse and the

masks were changing the same way as in an infrared CS system. For the time domain CS THz experiments showed in Chapter 6.2.3, the time delay stage did a scan for each mask to measure the complete THz pulse waveform.

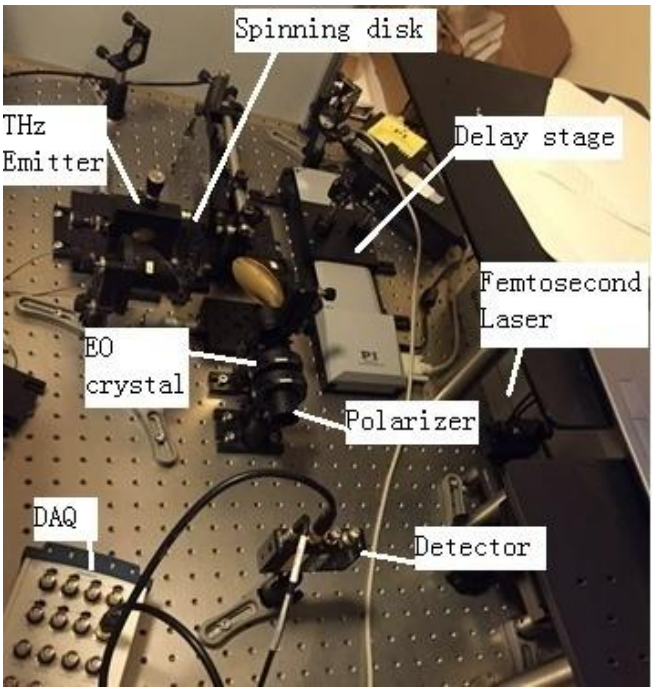

Figure.6.13 Picture of the THz time-domain spectroscopic system. A photoconductive emitter was used for THz generation and an EO crystal was used for THz detection.

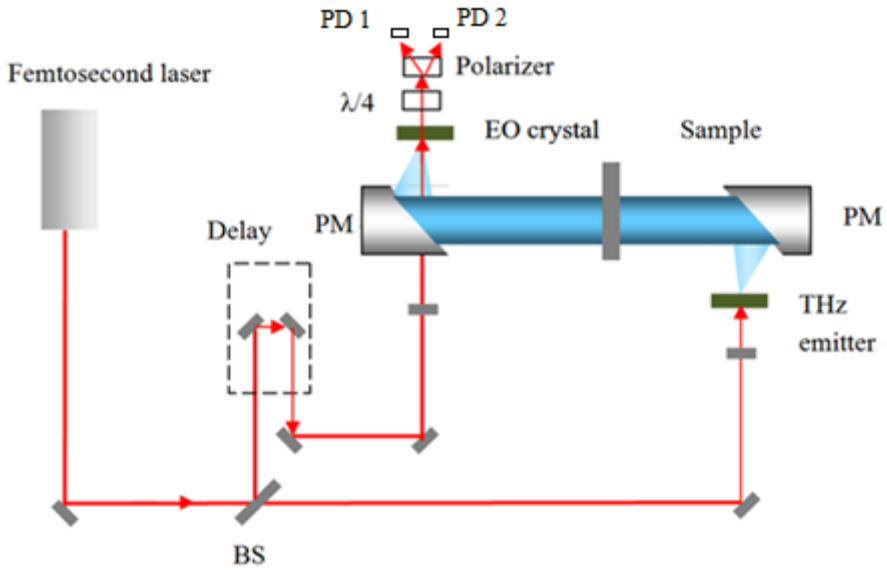

Figure.6.14 Schematic diagram of the THz-TDS system. A photoconductive emitter is used for THz generation and an EO crystal is used for THz detection. (PM: parabolic mirror, BS: beam splitter and EO: electro-optic).

6.2.2 CS THz imaging experiments using spinning disk

By scanning the time delay stage, a full THz time domain pulse and its frequency domain waveform can be obtained as shown in Figure.6.15. The THz waveform was recorded as a function of position of the time delay stage. The time delay scan distance was 6 mm and the scan speed was 0.1 mm/s. 8000 data points were measured during each scan. As can be seen from the frequency domain signal, the FWHM of the THz pulse was about 0.72 THz.

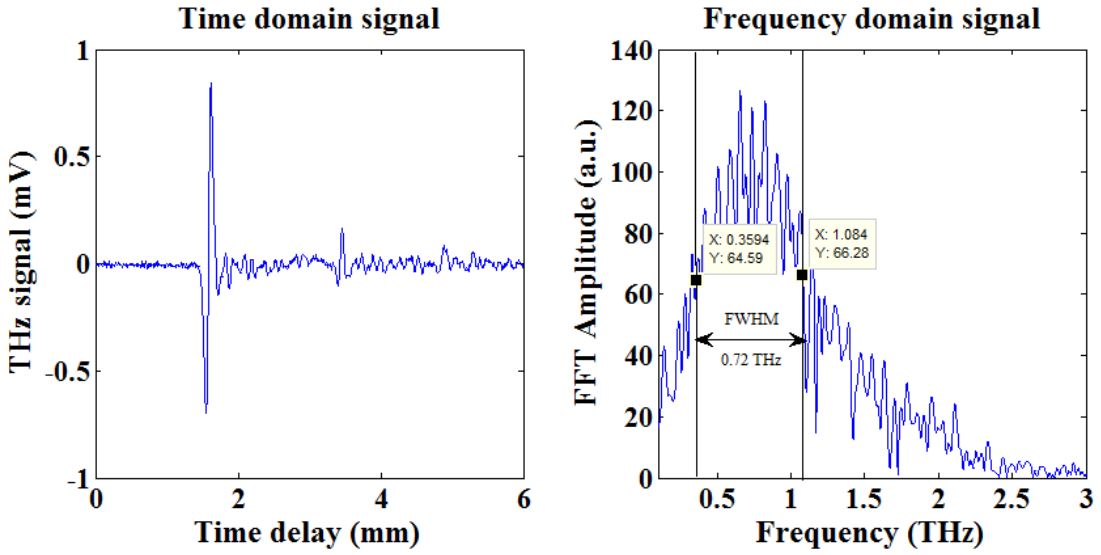

Figure.6.15 A time domain THz pulse measured from the THz TDS system and its waveform in frequency domain. The time delay scan distance was 6 mm and the scan speed was 0.1 mm/s. The FWHM of the system was about 0.72 THz.

The time delay stage was fixed at the location where the THz pulse has its maximum value. The spinning disk configuration was applied between the two PM showed in Figure 6.14. The system worked in a stop-measure-rotate routine. Every time the disk rotated 1 degree and the detector took a measurement for 1 second. A 48 by 48 pixels image could be reconstructed from 360 measurements. The effective imaging window had a dimension of 33 mm × 33 mm. A set of measurements were taken when no samples were placed on the imaging window. A 48 by 48 pixels image was reconstructed using this set of 360 measurements. The purpose of these measurements was to check the spatial distribution of the THz signal. The results are shown below in Figure.6.16.

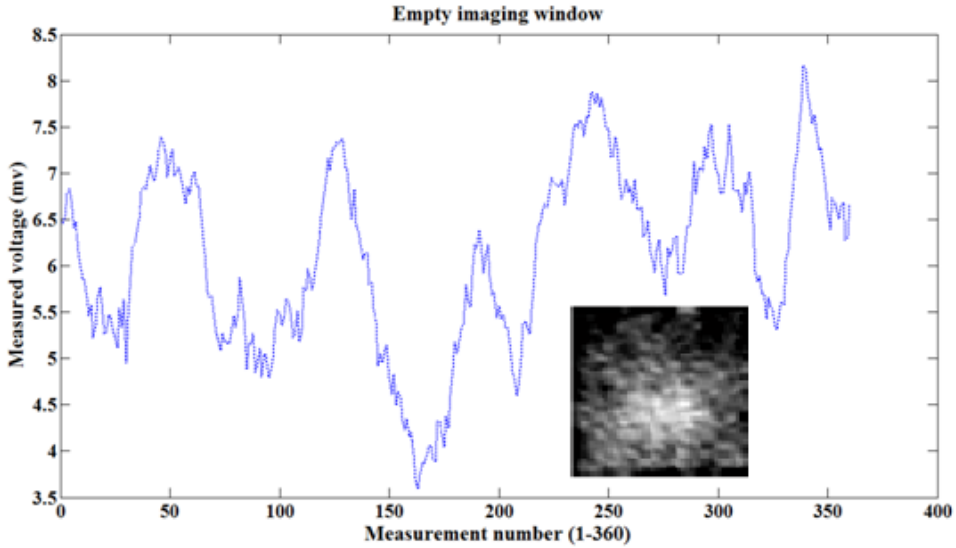

Figure.6.16 A set of data measured when there were no patterns and no samples in the imaging window. The delay line was fixed on the peak location of the THz pulse. The THz image was reconstructed from the 360 data points measured using the spinning disk and the resolution was 48 by 48 pixels.

The reconstructed image shows that the signal strength was not spatially uniform. The signal strength in the lower part of the imaging window was much stronger than the top part. By applying some samples which have more transparency in the lower part could help get a better imaging quality. Below are some patterns and their corresponding simulation and reconstructed images. All the images were reconstructed from 360 measurements and the resolution were 48 by 48 pixels.

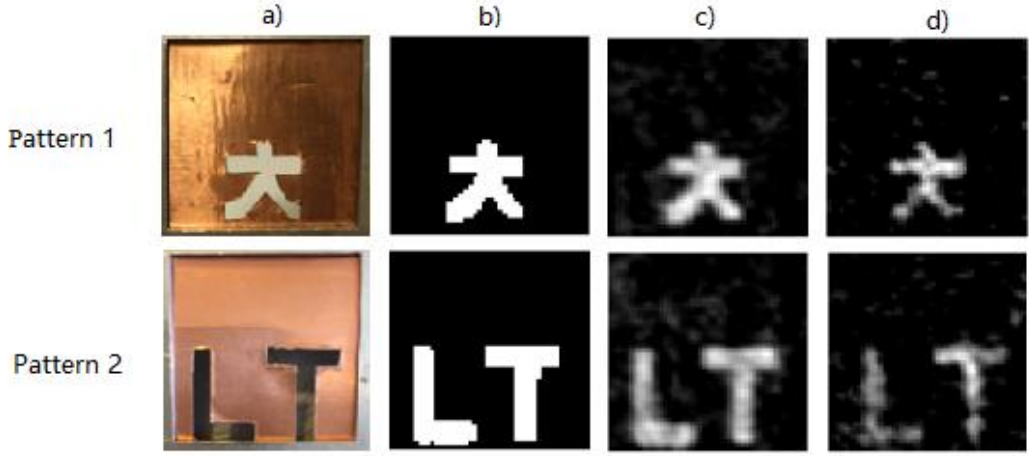

Figure.6.17 Picture of two samples and their corresponding simulation and reconstructed THz images. a) and b) were the physical and binary version of the sample. c) and d) were their corresponding simulation and experiments reconstruction THz images. The resolutions of the images were 48 by 48 pixels and were reconstructed from sets of 360 data points measured using the spinning disk.

Pattern 1 was a Chinese word and pattern 2 was two English letters ‘L’ and ‘T’. The copper tape was 100% opaque to THz beams and the cut-through part was 100% transparent to THz beam. The width of the cut-through parts of the patterns was 2-2.5 mm. It was set a little wider than the resolution of the spinning disk (1 mm) to get rid of the scattering and diffraction effects. All the patterns could be easily recognized from the reconstructed images. Comparisons of the two 360 measured data points and the simulation data points are shown below. Most points of the measured data and simulation data were matched.

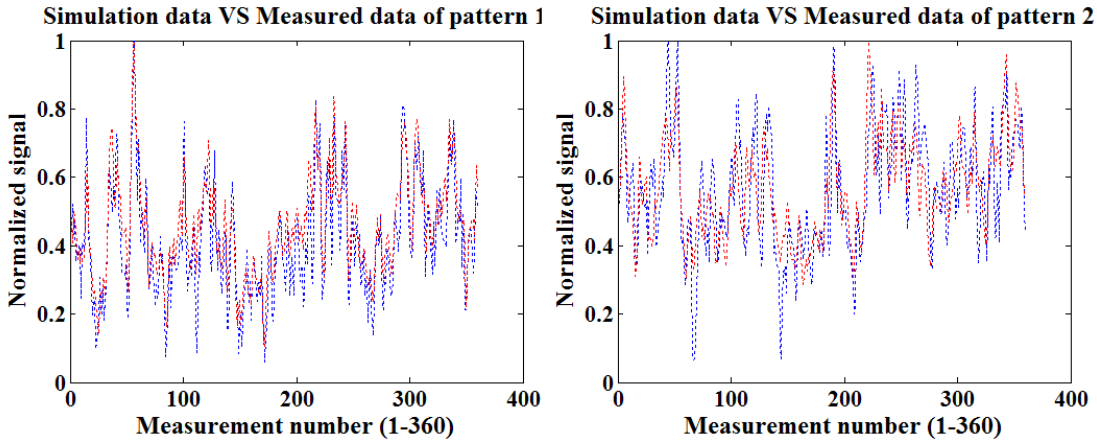

Figure.6.18 Comparisons between the simulation and measured data points of pattern 1 and pattern 2 showed in Figure.6.17 respectively. The red ones were the simulation data and the blue ones were the measured data. Both of them were normalized.

More quantified evaluations of these reconstructed images are shown in Table.6.2. The evaluation parameters used are Peak Signal-to-Noise Ratio (PSNR), Structural Similarity (SSIM) index, Mean Structural Similarity (MSSIM) and Feature Similarity (FSIM) index. The PSNRs of the two experiments results were still closed to the simulation results even the area of transparent was relatively small. Small transparent area on the samples means small THz signal power so the spinning disk performed well against noises.

Table.6.2 Quality evaluation of 48 by 48 pixels THz images reconstructed as shown in Figure.6.17.

	Pattern 1		Pattern 2	
	Simulation	Experiment	Simulation	Experiment
PSNR	18.92	14.95	15.20	10.39
SSIM	0.89	0.71	0.83	0.43
FSIM	0.60	0.36	0.53	0.34

Compared with Hao's results using the PCB substrate spinning disk [18], these reconstructed images were much better in quality, resolution and resolution. These were the benefits from the material and spatial light modular patterns of this new designed spinning disk. The new spinning disk didn't have any substrate so the noises caused by the absorption and diffraction of THz beam were much smaller.

6.2.3 Pulsed CS THz imaging

As introduced in the Chapter 2.1, the CS-THz time-domain (pulsed) spectroscopic imaging can obtain both spatial and spectral characteristics of a sample. One time delay scan was recorded for each measurement. The waveform of THz pulse contained both time domain and frequency domain information for one mask.

Since the scanning of time delay line was time costing (scan speed was 0.1mm/s and scan length was 5mm), the experiment period was longer than normal imaging experiments. The stability of the system needed to be checked before processing any measurement. The delay line was fixed at a random location of THz pulse and 100 measurements were taken to test the stability of the system. The time duration for each measurement was 10 seconds so the whole time duration tested was 1000 seconds. The intensity of the THz signal seems quite stable from Figure.6.19.

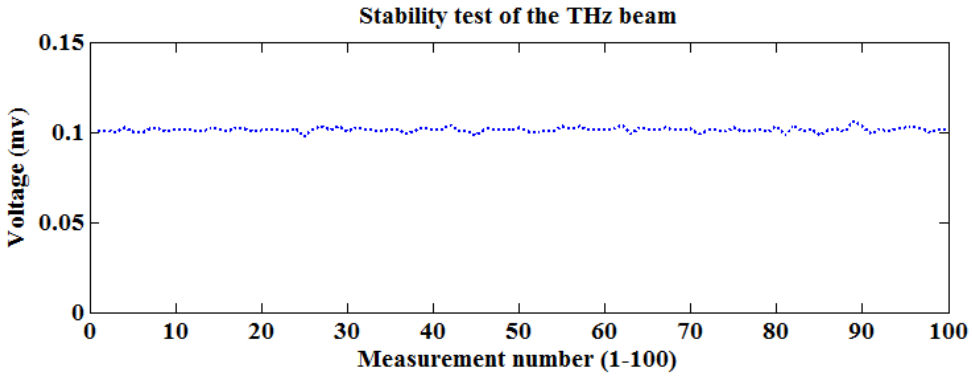

Figure.6.19 Stability test of the THz TDS system. These 100 data points were measured when the delay line stage was fixed in a location. The duration for each measurement was 10 second and the measured data was averaged. In total, the duration of the stability was 1000 seconds. The x axis was the number of measurements. The y axis was the measured voltage.

6.2.3.1 Manual measurements

A group of time domain scans had been done for samples which were different layers of seller tape. For each scan, the sample was inserted between the two parabolic mirrors showed in Figure.6.14 and the THz waveform was recorded as a function of position of the time delay stage. The scan distance was 5mm and the scan speed was 0.1m/s. 8000 data points were measured during each scan. The THz pulses and their corresponding waveform in frequency domain are shown below.

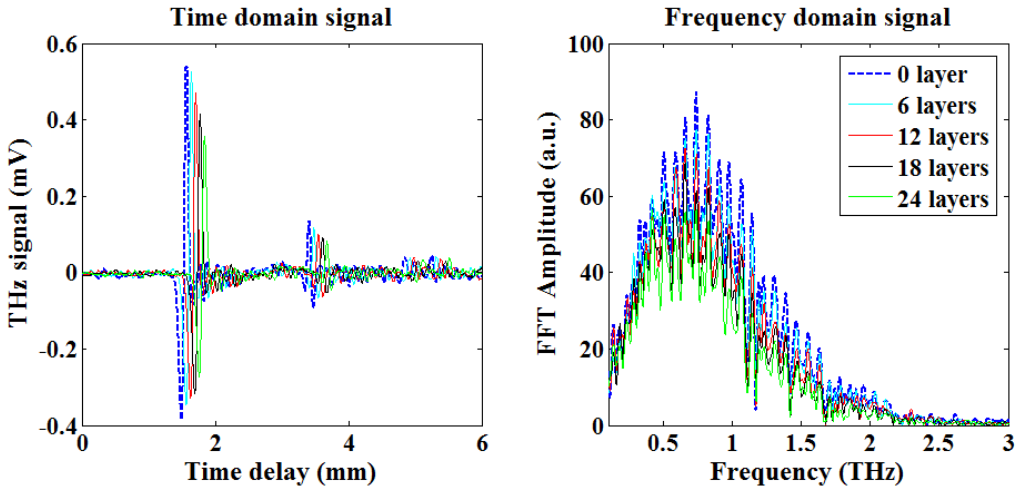

Figure.6.20 Time domain and frequency domain waveform of time delay scan for a group of samples which were different layers of seller tapes.

The time domain signal showed that as the number of layers went larger, the peaks of THz pulses went smaller and the location of the peaks of THz pulse were delayed more to the right. The thickness of the samples could be calculated from the distance between the positive and negative THz pulses. The frequency domain waveforms showed that the more layers the sample the more absorption, and the main absorption frequency was around 0.6 THz.

To further develop the spectral and spatial information from pulsed THz CS imaging, a group of measurements had been done using the 40 masks on a sample showed in Figure.6.21. The sample was made of copper tape and seller tape. The upper part of the pattern was made of copper tape which blocks the THz signal. The left bottom part was made of 6 layers of seller tape and the right bottom part was made of 15 layers of seller tape.

A time delay scanning had been done for the sample. The scanning distance was 5 mm and the scan speed was 0.1 m/s. 8000 data points were measured during the scan. The results are shown below together with the results obtained when there were no samples. The blue points were the signal for the sample and the black points were the reference signal. The two pulses of the blue signal in the time domain were corresponding to the two part of different thickness in the bottom of the sample. The frequency domain signal shows that the main absorption frequency was around 0.63 THz.

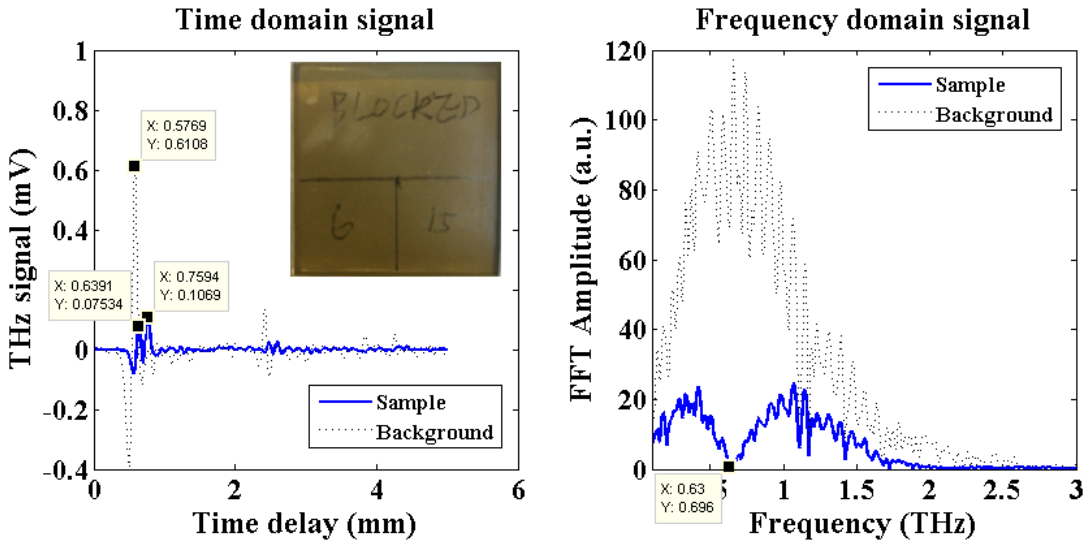

Figure.6.21 Picture of a multi layers seller tape sample and its THz time domain scanning results. The top part of the sample was blocked by copper tape. The left part of bottom half were 6 layers of seller tapes and right part of bottom half were 15 layers of seller tape. The blue data points were the signal for the sample and the black data points were the reference signal.

The set of 40 masks showed in Figure. 3.6 were applied to the time-domain spectroscopy system showed in Figure. 6.14. For each mask, the THz signal was measured as a function of time delay. For every measurement, the delay line stage was moved over a distance of 5mm at a speed of 0.1mm/s. In total, 40 time domain scanning were taken.

The groups of 40 THz time domain pulses measured are showed in Figure.6.22. The two images were reconstructed according to the two pulse peaks respectively. The resolution of the two images was 20 by 20 pixels.

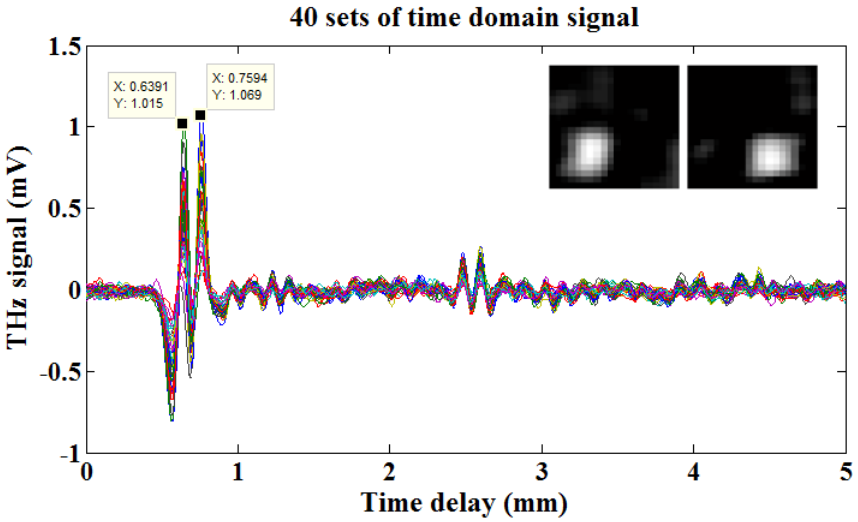

Figure.6.22 Group of 40 time domain THz pulses measured using the 40 masks. The x-axis referred to the scan distance. The y axis was the measured voltages. The peaks around 0.64mm and 0.76mm referred to the 15 and 6 layers of seller tape separately. The resolution of the two images reconstructed corresponding to data points at the two pulse peaks was 20 by 20 pixels.

The bright parts in the two reconstructed images represent the two parts of different thicknesses in the bottom half of the sample. The square shape of the two bright parts match the original shapes of those two parts in the sample. The frequency domain waveforms of the 40 measured THz pulses are shown in Figure.6.23. The main absorption frequency was around 0.6THz as shown in the figure. A 20 by 20 pixels image can be reconstructed at any of those frequencies.

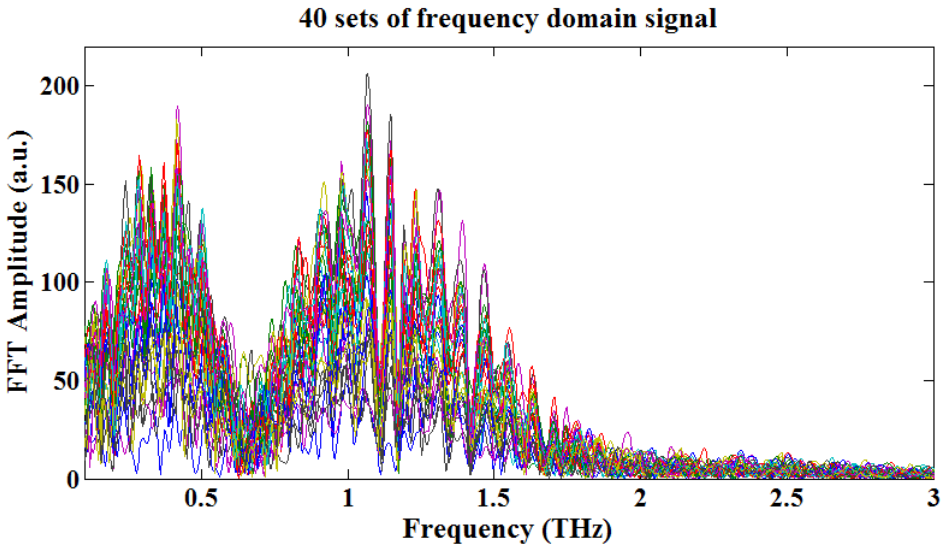

Figure.6.23 Group of 40 frequency domain waveforms of the 40 time domain THz pulses measured as shown in Figure.6.22.

A major advantage of THz-TDS is that the THz pulse is measured as a function of time so it can be transferred to frequency domain. This makes it available to obtain THz images at any single frequency or frequency ranges. Some images reconstructed according to data points at different frequencies or frequency ranges are shown below.

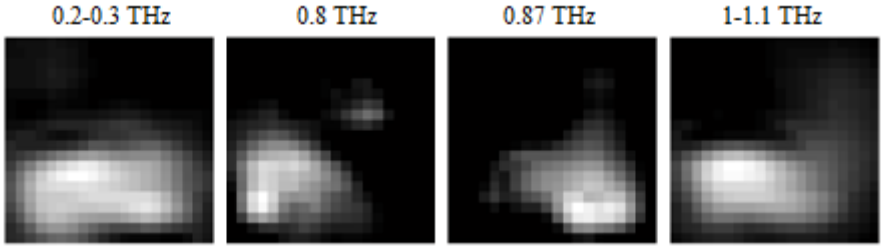

Figure.6.24 Images reconstructed according to data points at different frequencies or frequency ranges showed in Figure.6.23. The resolutions of these images were 20 by 20 pixels.

The resolution of these reconstructed images was 20 by 20 pixels. At 0.2 – 0.3 THz, the average absorption of both sides were about the same. The reconstructed image showed that the top half was blocked and the bottom half was transparent to THz beams, which was in accordance with the sample. At 0.8 THz the right side (6 layers) absorbed more THz beam than the left side (15 layers) so the left bottom part was bright and the right bottom was dark. At 0.87 THz the left side absorbed more THz beam than the right side so the left bottom part was dark and the right bottom was bright. The average absorption of the two sides went back to the same at 1 – 1.1 THz so the reconstructed image was like the one at 0.2-0.3 THz again. The two images reconstructed at 0.8 THz and 0.87 THz were in accordance with the two images reconstructed according to the time domain signals.

6.2.3.2 Automatic measurements using spinning disk

Time domain scanning had been taken on two samples using the spinning disk as shown below. The experiment procedure was about the same as the experiments done using the 40 masks except in this part, the masks were changed automatically using the spinning disk. For each mask, the THz signal was measured as a function of time delay. For every measurement, the delay line stage was moved over a distance of 5mm at a speed of 0.1mm/s. In total, 360 time domain scanning were taken.

Sample 1

The sample showed in Figure.6.25 was made of copper tape and organic glass. The upper part of the pattern was made of copper tape which blocks the THz signal. The bottom part was a piece of 2 mm thick organic glass with a drilled circle hole. A time delay scan had been done for the sample. The scan distance was 5mm and the scan speed was 0.1m/s. 8000 data points were measured during each scan. The results are shown below together with the results obtained when there were no samples. The blue points were the signal for the sample and the black points were the reference signal. The two pulses of the blue signal in the time domain were corresponding to the organic glass part and the drilled hole in the bottom of the sample. The frequency domain signal shows that the main absorption frequency was around 0.59 – 0.78 THz.

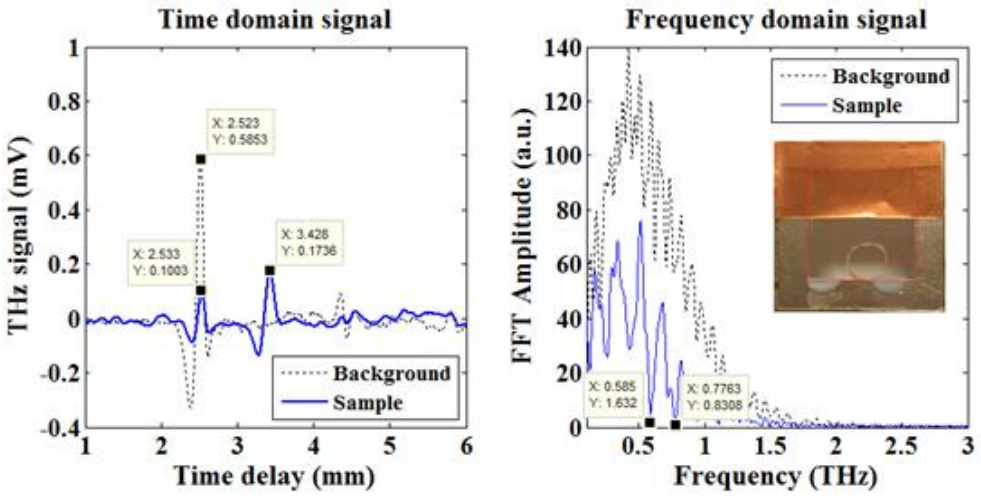

Figure.6.25 Picture of sample 1 and its THz scanning results. The top part of the sample was blocked by copper tape. The bottom part was a piece of 2mm thick organic glass with a drilled circle hole. The blue ones are the signal for the sample and the black ones are the reference signals.

The groups of 360 THz time domain pulses measured are shown in Figure.6.26. The two pulses in the time domain were corresponding to the THz beam transmitted through the organic glass and the drilled hole respectively. The two images were reconstructed according to the two pulse peaks respectively. The resolution of the two images was 48 by 48 pixels.

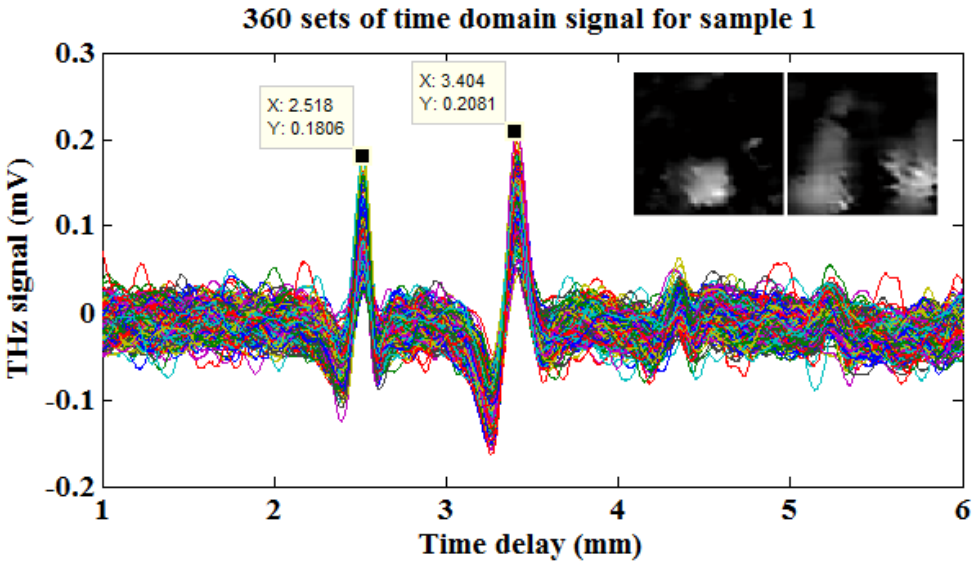

Figure.6.26 Group of 360 time domain THz pulse measured using the spinning disk for sample 1. The x-axis referred to the scan distance. The y axis was the measured voltages. The peaks around 2.53 mm and 3.43 mm referred to the THz beam transmitted through the organic glass and the hole separately. The two images were reconstructed corresponding to data points at the two pulse peaks and the resolutions were 48 by 48 pixels.

The bright parts in the first reconstructed image represented the drilled hole in the sample. The circle shape of the bright part match the original shapes of the drilled hole in the sample. The bright parts in the second reconstructed image represented the organic glass in the sample. There was some noise in the top part of the reconstructed image and the circle shape was not perfectly reconstructed.

The frequency domain waveforms of the 360 measured THz pulses are shown in Figure.6.27. Two images were reconstructed according to the data points at 0.87 THz and 0.31-0.5 THz respectively. The resolution of these reconstructed images was 48 by 48 pixels. At 0.87 THz, the organic glass absorbed more THz beam than the drilled hole so the circle hole was much brighter than the organic glass part and the shape of the bright part was in accordance with the sample. At 0.31 – 0.5 THz, the average absorption of the organic glass was much weaker so the circle part in the middle was much darker.

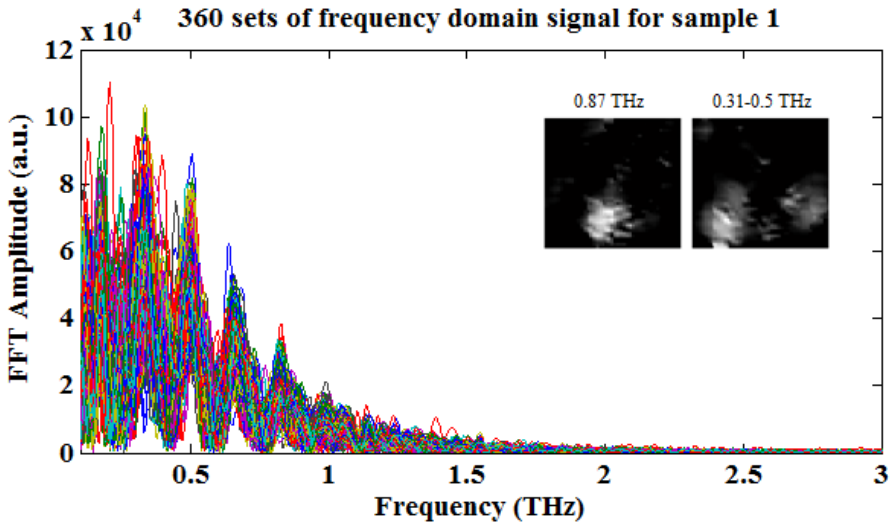

Figure.6.27 Group of 360 frequency domain waveforms of the 360 time domain THz pulses measured for sample 1 as shown in Figure.6.26. The two images were reconstructed according to data points at 0.87 THz and 0.31 – 0.5 THz. The resolutions of these images were 48 by 48 pixels.

Sample 2

The sample showed in Figure.6.28 was made of copper tape and plastic board. The upper part of the pattern was made of copper tape which blocks the THz signal. The bottom part was a piece of 0.2 mm thick plastic board with cut through pattern.

The frequency domain waveforms of the 360 measured THz pulses are shown in Figure.6.27. An image was reconstructed according to the data points at 0.92-1 THz. The resolution of the reconstructed image was 48 by 48 pixels.

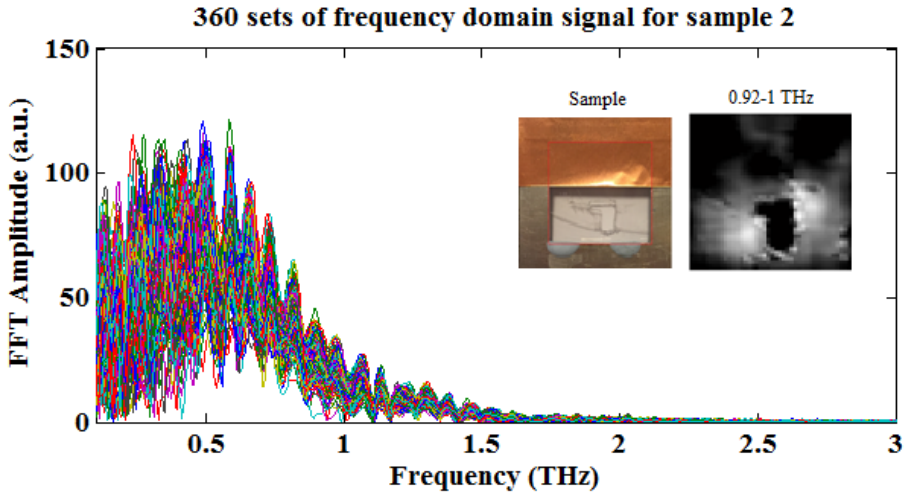

Figure.6.28 Picture of sample 2 and 360 frequency domain waveforms of the 360 time domain THz pulses measured for sample 2. The top part of the sample was blocked by copper tape. The bottom part was a piece of 0.2 mm thick plastic board with a cut through pattern. The image was reconstructed according to data points at 0.92 – 1 THz. The resolution of this image was 48 by 48 pixels.

At 0.92 – 1 THz, the absorption of the plastic board was much weaker than the pattern part. The edge of the pattern could be clearly recognized from the reconstructed image and the shape was in accordance with the sample.

The groups of 360 THz time domain pulses measured are shown in Figure.6.29. The two pulses in the time domain were corresponding to the THz beam transmitted through the plastic board and the pattern respectively. The two images were reconstructed according to the two pulse peaks respectively. The resolution of the two images was 48 by 48 pixels. The dark part in the bottom part of reconstructed image represented the cut through pattern in the sample. The shape of the dark part matched the original shape in the sample.

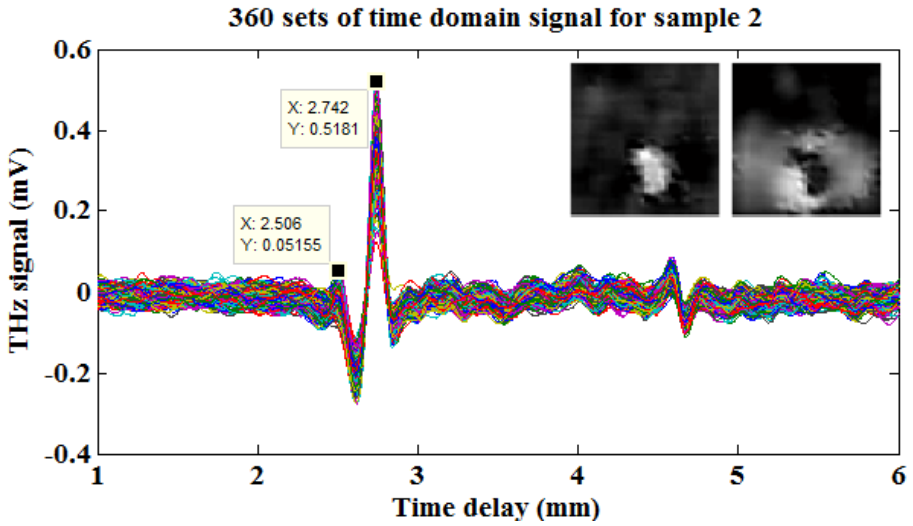

Figure.6.29 Group of 360 time domain THz pulse measured using the spinning disk for sample 2. The x-axis referred to the scan distance. The y axis was the measured voltages. The peaks around 2.50 mm and 2.74 mm referred to the THz beam transmitted through the organic glass and the hole separately. The two images were reconstructed corresponding to data points at the two pulse peaks and the resolutions were 48 by 48 pixels.

6.3 Noise analysis

Drift of the direction and power of the THz beam after a period of operation was the main source of noise in the measurements. The drift of power can be balanced off but adding another reference detector with beam splitter. Although the areas of the detector and parabolic mirror were quite big, which provided some margin for the movement of the focus point of the THz beam, the geometry distortion resulted from

the parabolic mirror can’t be removed.

Another noise source was the inaccuracy of the parabolic mirror fabricated from stainless steel. Normally a parabolic mirror is a precise optical instrument with gold coating on the surface to provide accurate reflection while the PM here was just fabricated using stainless steel. Since the size of the PM needed was too big (6 inches diameter) so there was no precise commercial one available.

The reflections caused by the surface of metal enclosure also contributed to the noises. During the measurements, the metal enclosure was a closed space. Multiple reflections happened inside the box between the metal surfaces of the box and other instruments.

The noises in the THz time domain system can be classified as electric noise and light noise. The detector used in the projector was a commercial one with a built in amplifier circuit. This integrated circuit minimized the electric noise to an acceptable level. The other electric noise including noise from data acquisition devices and the cables were minor. The use of a lock-in amplifier only amplified signal in the same phase with the reference signal so most electric noise was removed.

The light noise including diffraction and scattering effects caused by the masks and samples, absorption of THz radiation by vapor, mechanical vibration of the laser source and optical system, geometry distortion caused by the two parabolic mirrors and phase error caused by optical components in the system. The size of the circle patterns on the disk was close to the wavelength of THz radiation so there were scattering and the diffraction effects caused by the circle patterns. The scattering effect of THz radiation at the sharp corners of the samples also contributed to the light noise. The wide band of THz pulses made the phase error resulted from optical component in the system can no longer be negligible. The mechanical vibration in or nearby the lab may cause the movements of the optical components or the laser source hence increase the light noise.

6.4 Summary and Future work

Some CS imaging experiments using the spinning disk in Daresbury Lab to study the imaging properties of THz beam transmit through food samples. The power of THz radiation in normal labs is not strong enough to transmit through food samples while in the particle accelerator lab the THz beam was ultra strong. The output of the particle accelerator was more stable after several hours' operation so in future, the lab could operate in two shifts to cover 24 hours a day to get more stable output signal. The video rate CS imaging system discussed in Chapter 4 could be installed in Daresbury lab to further increase imaging speed. The inner surface of the metal enclosure should be covered by material which strongly absorbs THz radiation to reduce reflections.

On the THz time domain system based on a photoconductive antenna emitter and an EO crystal receiver, CS imaging measurements have been done using the new spinning disk. Images were reconstructed from time domain signals and frequency domain signals. The imaging quality was outstanding and both spatial and spectral results can be obtained from the same measurements. For the future, more meaningful samples should be measured and the video rate CS imaging system could be used to further increase imaging speed.

Chapter 7

Conclusions and Future work

7.1. Conclusion

To realize fast experimental validation for CS imaging sampling operator design, a projector based CS imaging system was developed in this work. The system can be considered as an adapted version of the famous single pixel camera configuration. In the projector based CS system, there were no physical masks or samples therefore no need to fabricate the masks physically, which was time and cost effective. Also there was no limitation on speed of changing the masks.

The main criteria of CS imaging masks design including imaging quality, sampling rate, resolution, implementation complexity and imaging speed were investigated. The computation complexity of reconstruction will be far beyond the capacity of a normal computer if the resolution is high (256 by 256 pixels). An idea of HD masks achieved by Golay sequence modulated Hadamard matrix was proposed and validated by using the projector based CS imaging system.

A spinning disk with circle pattern as sampling operator for CS THz imaging was proposed and validated using the projector based CS imaging system. The sampling operators on the disk could be considered as a Toeplitz block matrix. The reconstruction quality achieved by using the spin disk measurement matrix (nearly block Toeplitz matrix) was close to the level of the well-proved CS matrices such as random matrix. A resolution of better than 2 mm had been achieved with the 2 mm diameter circular pattern masks.

For the new designed spinning disk, a number of 2 mm diameter holes were chemically etched on this steel plate randomly. Each hole was 100% transparent to light while the stainless steel was 100% opaque to light. The size of the round holes

on the disk was relatively larger than the square pattern (1 mm diameter) in the early designed disk so the performance against diffraction and scattering effects were better. There was no substrate material so the intensity of THz signal transmit through the disk was increases and the noise caused by the un-uniform THz absorption of the substrate was minimized.

Before applying the spinning disk in THz imaging system, the imaging quality of the spinning disk was also validated using the infrared CS imaging system. The parabolic mirrors, spinning disk and the samples used in the infrared system were the same as in a THz system so the results should be more convincible. Another benefit of infrared was that the wavelength was closer to that of THz so the scattering and diffraction effects in the infrared system were more similar to those in a THz system. To further increase the imaging speed, a video rate CS imaging system has been adapted using infrared CS set up and the spinning disk. An image acquisition speed of about 10 frames per second at 96 by 96 pixels resolution was achieved.

The idea of increasing the number of detectors in CS imaging experiments showed up along with the developments of CS sampling operators. The concept of block CS was demonstrated using the THz spinning disk and a 2x2 sensor array. The imaging speed was further increased by breaking the original image into blocks then measure and reconstruct these blocks independently and in parallel. In the experiment set up, each element in the sensor array worked in parallel thus both the data acquisition and image reconstruction speeds have been improved.

Some CS imaging experiments using the spinning disk in Daresbury Lab to study the imaging properties of THz beam transmit through food samples. The power of THz radiation in normal labs is not strong enough to transmit through food samples while in the particle accelerator lab the THz beam was ultra strong. Images of THz beam transmitting through a piece have been reconstructed.

On the THz time domain system based on a photoconductive antenna emitter and an EO crystal receiver, CS imaging measurements have been done using the new

spinning disk. Images were reconstructed from time domain signals and frequency domain signals. The imaging quality was outstanding and both spatial and spectral results can be obtained from the same measurements.

7.2. Future work

The projector CS imaging system showed good capability in fast masks designing validation for images up to 512 by 512 pixels (limited by the resolution of the projector). The system was very compact, cost effective and easy to configure so any group doing research on CS masks designing can use this set up to obtain proof-of-concept experimental results.

During imaging process, the masks were projected onto a physical subject and an image of the physical subject can be reconstructed so the system can be considered as an active imaging system. The compact design and low storage requirements gives the system great potential in real world imaging such as car registration recognition in traffic control or car park control, which suffers huge storage pressure presently.

Currently, there is no sensitive THz detector array so some experiments were carried out on the infrared system. The results showed that the spinning disk worked well with the block CS concept. This give the disk a potential in block THz CS imaging once suitable THz sensor array is fabricated in future.

The THz time domain system together with the spinning disk can be used to obtain both the spatial distribution and the spectral characteristics of a sample. Instead of using a step motor for the spinning disk, a continuous high speed motor can be applied here to achieve video rate THz imaging.

The output of the particle accelerator was more stable after several hours' operation, therefore in future, the lab could operate in two shifts to cover 24 hours a day to get more stable output signal. The video rate CS imaging system discussed in Chapter 4 could be installed in Daresbury lab to further increase imaging speed.

For the photoconductive antenna and EO crystal based THz time domain system, the direction and power of the THz beam could be optimized by adjusting the parabolic mirror in the system. A reflection THz time domain CS imaging system could be set up to measure more meaningful samples. The video rate CS imaging system could be used to further increase imaging speed.

References

[1] M. Walther, B. Fischer, M. Schall, H. Helm, and P. U. Jepsen, " Far-infrared vibrational spectra of all-trans, 9-cis and 13-cis retinal measured by THz time-domain spectroscopy," *Chem. Phys. Lett*. vol. 332, no. 3-4, pp. 389-395, 2000.

[2] Y. C. Shen, P. C. Upadhya, E. H. Linfield, H. E. Beere, and A. G. Davies, "Temperature-dependent low-frequency vibrational spectra of purine and adenine," *Appl. Phys. Lett.*, vol. 82, no. 12, pp. 2350-2352, 2003.

[3] A. G. Davies, A. D. Burnett, W. Fan, E. H. Linfield, and J. E. Cunningham, "Terahertz spectroscopy of explosives and drugs," *Mater. Today*, vol. 11, no. 3, pp. 18-26, 2008.

[4] B. B. Hu and M. C. Nuss, "Imaging with terahertz waves," *Opt. Lett*. vol. 20, no. 16, pp. 1716-1718, 1995.

[5] E. Pickwell, B. E. Cole, A. J. Fitzgerald, M. Pepper and V. P. Wallace, " In vivo study of human skin using pulsed terahertz radiation," *Phys. Med. Biol*. vol. 49, no. 9, pp. 1595-1607 , 2004.

[6] K. Kawase, Y. Ogawa, Y. Watanabe, and H. Inoue, "Non-destructive terahertz imaging of illicit drugs using spectral fingerprints," *Opt. Express*, vol. 11, no. 20, pp. 2549-2554, 2003.

[7] Y. C. Shen and P. F. Taday, " Development and application of terahertz pulsed imaging for non-destructive inspection of pharmaceutical tablet," *IEEE J. Sel. Top. Quantum Electron*.vol. 14, no. 2, pp. 407-415, 2008.

[8] A. W. M. Lee, Q. Qin, S. Kumar, B. S. Williams, Q. Hu, and J. L. Reno, "Real-time terahertz imaging over a standoff distance (>25 meters)," *Appl. Phys. Lett.*, vol. 89, no. 14, 141125, 2006.

[9] Z. Jiang and X. C. Zhang, "Terahertz imaging via electrooptic effect," *IEEE Trans. Microwave Th. Tech.*, vol. 47, no. 12, pp. 2644-2650, 1999.

[10] J. Pearce, H. H. Choi, D. M. Mittleman, J. White, and D. Zimdars, "Terahertz wide aperture reflection tomography," *Opt. Lett.*, vol. 30, no. 13, pp. 1653-1655, 2005.

[11] S. Wang and X. Zhang, "Pulsed terahertz tomography," *J. Phys. D: Appl. Phys.*, vol. 37, no. 4, pp. 964 (R31-R36), 2004.

[12] A. Bandyopadhyay, A. Stepanov, B. Schulkin, M. D. Federici, A. Sengupta, D. Gary, J. F. Federici, R. Barat, Z. H. Michalopoulou, and D. Zimdars, "Terahertz interferometric and synthetic aperture imaging," *J. Opt. Soc. Am. A*, vol. 23, no. 5, pp. 1168-1178, 2006.

[13] D. L. Donoho, "Compressed sensing," *IEEE Trans. Inf. Theory*, vol. 52, no. 4, pp. 1289-1306, 2006.

[14] E. J. Candès, J. Romberg, and T. Tao, "Robust uncertainty principles: Exact signal reconstruction from highly incomplete frequency information," *IEEE Trans. Inf. Theory*, vol. 52, no. 2, pp. 489-509, 2006.

[15] W. L. Chan, K. Charan, D. Takhar, K. F. Kelly, R. G. Baraniuk, and D. M.

Mittleman, "A single-pixel terahertz imaging system based on compressed sensing," *Appl. Phys. Lett.*, vol. 93, no. 12, 121105, 2008.

[16] W. L. Chan, M. L. Moravec, R. G. Baraniuk, and D. M. Mittleman, "Terahertz imaging with compressed sensing and phase retrieval," *Opt. Lett*.vol. 33, no. 9, pp. 974-976, 2008.

[17] Y. C. Shen, L. Gan, M. Stringer, A. Burnett, K. Tych, H. Shen, J. E. Cunningham, E. P. J. Parrott, J. A. Zeitler, L. F. Gladden, E. H. Linfield, and A. G. Davies, "Terahertz pulsed spectroscopic imaging using optimized binary masks," *Appl. Phys. Lett.*, 95, no. 23, 231112, 2009.

[18] H. Shen, L. Gan, N. Newman, Y. Dong, C. Li, Y. Huang and Y. C. Shen, "Spinning disk for compressive imaging," *Opt. Lett.*, vol. 37, no. 1, pp. 46-48, 2012.

[19] Lu Gan, Lin Liu and Yaochun Shen, “Golay sequence for parital Fourier and Hadamard compressive imaging,” Acoustics, Speech and Signal Processing (ICASSP), 2013 IEEE International Conference, May 26-31, 2013, Vancouver, BC

[20] Lin Liu, Lu Gan, Yi Huang and Yaochun Shen, “Terahertz imaging via block-based compressive sensing,” IET Colloquium on Millimetre-wave and Terahertz Engineering & Technology, March 6 2014, Liverpool, UK.

[21] D. H. Auston and K. P. Cheung, "Coherent time-domain far-infrared spectroscopy," *J. Opt. Soc. Am. B*, vol. 2, no. 4, pp. 606-612, 1985.

[22] P. R. Smith, D. H. Auston, and M. C. Nuss, "Subpicosecond photoconducting dipole antennas," *IEEE J. Quant. Elec.*, vol. 24, no. 2, pp. 255-260, 1988.

[23] C. Fattinger and D. Grischkowsky, "Terahertz beams," *Appl. Phys. Lett.*, vol. 54, no. 6, pp. 490, 1989.

[24] M. V. Exter, C. Fattinger, and D. Grischkowsky, "Terahertz time-domain spectroscopy of water vapor," *Opt. Letts.*, vol. 14, no. 20, pp. 1128-1130, 1989.

[25] D. M. Mittleman, R. H. Jacobsen, and M. C. Nuss, "T-ray imaging," *IEEE Set Top. Quant. Elec*, vol. 2, pp. 679-692, 1996.

[26] J. D. Kafka, M. L. Watts, and J. W. J. Pieterse, "Picosecond and femtosecond pulse generation in a regeneratively mode-locked Ti:sapphire laser," *IEEE J. Quantum Electronics*, vol. 28, no. 10, pp. 2151-2162, 1992.

[27] G. P. Gallerano and S. Biedron, "Overview of terahertz radiation sources," *26th International Free Electron Laser (FEL) Conference*, Trieste, Italy, 2004.

[28] P. U. Jepsen, D. G. Cooke, and M. Koch, "Terahertz spectroscopy and imaging - Modern techniques and applications," *Laser Photonics*, vol. 5, no. 1, pp. 124-166, 2010.

[29] D. H. Auston, "Picosecond optoelectronic switching and gating in silicon," *Appl. Phys. Lett.*, vol. 26, no. 3, pp. 101-103, 1975.

[30] Y. C. Shen, "Terahertz pulsed spectroscopy and imaging for pharmaceutical applications: A review," *Int. J. Pharm.*, vol. 417, no. 1-2, pp. 48-60, 2011.

[31] P. U. Jepsen, R. H. Jacobsen, and S. R. Keiding, "Generation and detection of terahertz pulses from biased semiconductor antennas," *J. Opt. Soc. Am. B*, vol. 13, no. 11, pp. 2424-2436, 1996.

[32] D. W. Faries, K. A. Gehring, P. L. Richards, and Y. R. Sheen,"Tunable Far-Infrared Radiation Generated from the Difference Frequency between Two Ruby Lasers," *Phys. Rev.*, vol. 180, no.2, pp. 363-365, 1969.

[33] L. Xu, X. C. Zhang, and D. H. Auston, "Terahertz beam generation by femtosecond optical pulses in electro-optic materials," *Appl. Phys. Lett.*, vol. 61, no. 15, pp. 1784-1786, 1992.

[34] Q. Wu and X. C. Zhang, "Free-space electro-optic sampling of terahertz beams," *Appl. Phys. Lett.*, vol. 67, no. 24, pp. 3523-3525, 1995.

[35] Q. Wu and X. C. Zhang, "Ultrafast electro-optic field sensors," *Appl. Phys. Lett.*, vol. 68, no. 12, pp. 1604-1606, 1996.

[36] G. Gallot, J. Q. Zhang, R.W. McGowan, T. I. Jeon, and D. Grischkowsky, "Measurements of the THz absorption and dispersion of ZnTe and their relevance to the electro-optic detection of THz radiation," *Appl. Phys. Lett.*, vol. 74, no. 23, pp. 3450, 1999.

[37] Q. Wu and X. C. Zhang, "7 terahertz broadband GaP electro-optic sensor," *Appl. Phys. Lett.*, vol. 70, no. 14, pp. 1784-1786, 1997.

[38] P. Y. Han and X. C. Zhang, "Coherent, broadband midinfrared terahertz beam sensors," *Appl. Phys. Lett.*, vol. 73, no. 21, pp. 3049-3051, 1998.

[39] R. Huber, A. Brodschelm, F. Tauser, and A. Leitenstorfer, "Generation and field-resolved detection of femtosecond electromagnetic pulses tunable up to 41 THz," *Appl. Phys. Lett.*, vol. 76, no. 22, pp. 3191-3193, 2000.

[40] C. Kübler, R. Huber, S. Tubel, and A. Leitenstorfer, "Ultrabroadband detection of multi-terahertz field transients with GaSe electro-optic sensors: Approaching the near infrared," *Appl. Phys. Lett.*, vol. 85, no. 16, pp. 3360-3362, 2004.

[41] D. J. Cook and R. M. Hochstrasser, "Intense terahertz pulses by four-wave rectification in air," *Opt. Lett.*, vol. 25, no. 16, pp. 1210-1212, 2000.

[42] T. Löffler, F. Jacob, and H. G. Roskos, "Generation of terahertz pulses by photoionization of electrically biased air," *Appl. Phys. Lett.*, vol. 77, no. 3, pp. 453-455, 2000.

[43] J. Dai, X. Xie, and X. C. Zhang, "Detection of Broadband Terahertz Waves with a Laser-Induced Plasma in Gases," *Phys. Rev. Lett.*, vol. 97, no. 10, 103903, 2006.

[44] I. S. Gregory, C. Baker, W. R. Tribe, I. V. Bradley, M. J. Evans, E. H. Linfield, A. G. Daives, and M. Missous, "Optimization of photomixers and antennas for continuous-wave terahertz emission," *IEEE J. Quantum Electronics*, vol. 41, no. 5, pp. 717-728, 2005.

[45] S. Verghese, K. A. McIntosh, S. Calawa, W. F. Dinatale, E. K. Duerr, and K. A. Molvar, "Generation and detection of coherent terahertz waves using two photomixers," Appl. Phys. Lett., vol. 73, no. 26, pp. 3824-3826, 1998.

[46] M. Tani, S. Matsuura, K. Sakai, and M. Hangyo, "Multiple-frequency generation of sub-terahertz radiation by multimode ld excitation of photoconductive antenna," *IEEE Microwave Guided Wave Lett.*, vol. 7, no. 9, pp. 282-284, 1997.

[47] E. R. Brown, K. A. McIntosh, K. B. Nichols, and C. L. Dennis, "Photomixing

up to 3.8 THz in low-temperature-grown GaAs," *Appl. Phys. Lett.*, vol. 66, no. 3, pp. 285-287, 1995.

[48] R. Wilk, F. Breitfeld, M. Mikulics, and M. Koch, "Continuous wave terahertz spectrometer as a noncontact thickness measuring device," *Appl. Opt.*, vol. 47, no. 16, pp. 3023-3026, 2008.

[49] A. Dobroiu, M. Yamashita, Y. N. Ohshima, Y. Morita, C. Otani, and K. Kawase, "Terahertz imaging system based on a backward-wave oscillator," *Appl. Opt.*, vol. 43, no. 30, pp. 5637-5646, 2004.

[50] B. Ferguson and X. C. Zhang, "Materials for terahertz science and technology," *Nature Materials*, vol. 1, no. 1, pp. 26-33, 2002.

[51] R. Kohler, A. Tredicucci, F. Beltram, H. E. Beere, E. H. Linfield, A. G. Davis, D. A. Davis, D. A. Ritchie, R. C. Lotti, and F. Rossi, "Terahertz semiconductor-heterostructure laser," *Nature*, vol. 417, no. 6885, pp. 156-159, 2002.

[52] A. Wade, G. Fedorov, D. Smirnov, S. Kumar, B. S. Williams, Q. Hu, and J. L. Reno, "Magnetic-field-assisted terahertz quantum cascade laser operating up to 225K," *Nature Photonics*, vol. 3, no. 1, pp. 41-45, 2009.

[53] N. Jukam, S. S. Dhillon, D. Oustinov, J. Madeo, C. Manquest, S. Barbieri, C. Sirtori, S. P. Khanna, E. H. Linfield, A. G. Davies, and J. Tignon, "Terahertz amplifier based on gain switching in a quantum cascade laser," *Nature Photonics*, vol. 3, no. 12, pp. 715-719, 2009.

[54] G. P. Williams, "Far-IR/THz radiation from the Jefferson Laboratory, energy recovered linac, free eletron laser," *Rev. Sci. Instrum.*, vol. 73, no. 3, pp. 1461-1463, 2002.

[55] A. C. Warren, J. M. Woodall, J. L. Freeouf, D. Grischkowsky, D. T. McInturff, M. R. Melloch, and N. Otsuka, "Arsenic precipitates and the semi-insulating properties of GaAs buffer layers grown by low-temperature molecular beam epitaxy," *Appl. Phys. Lett.*, vol. 57, no. 13, 1331-1333, 1990.

[56] S. Gupta, M. Y. Frankel, J. A. Valdmanis, J. F. Whitaker, G. A. Mourou, F. W. Smith, and A. R. Calawa, "Subpicosecond carrier lifetime in GaAs grown by molecular beam epitaxy at low temperatures," *Appl. Phys. Lett.*, vol. 59, no. 25, pp. 3276-3278, 1991.

[57] S. Gupta, J. F. Whitaker, and G. A. Mourou, "Ultrafast carrier dynamics in III-V semiconductors grown by molecular-beam epitaxy at very low substrate temperatures," *IEEE J. Quantum Electronics*.vol. 28, no. 10, pp. 2464-2472, 1992.

[58] I. S. Gregory, C. Baker, W.R. Tribe, M. J. Evans, H. E. Beere, E. H. Linfield, A. G. Davies, and M. Missous, "High resistivity annealed low-temperature GaAs with 100 fs lifetimes," *Appl. Phys. Lett.*, vol. 83, no. 20, pp. 4199-2401, 2003.

[59] J. Sigmund, C. Sydlo, H. L. Hartnagel, N. Benker, H. Fuess, F. Rutz, T. Kleine-Ostmann, and M. Koch, "Structure investigation of low-temperature-grown GaAsSb, a material for photoconductive terahertz antennas," *Appl. Phys. Lett.*, vol. 87, no. 25, 252103, 2005.

[60] C. Baker, I. S. Gregory, W. R. Tribe, I. V. Bradley, M. J. Evans, E. H. Linfield,

and M. Missous, "Highly resistive annealed low-temperature-grown InGaAs with sub-500 fs carrier lifetimes," *Appl. Phys. Lett.*, vol. 85, no. 21, pp. 4965-4967, 2004.

[61] B. Sartorius, H. Roehle, H. Künzel, J. Böttcher, M. Schlak, D. Stanze, H. Venghaus, and M. Schell, "All-fiber terahertz time-domain spectrometer operating at 1.5 μm telecom wavelengths," *Opt. Express*, vol. 16, no. 13, pp. 9565-9570, 2008.

[62] H. Roehle, R. J. B. Dietz, H. J. Hensel, J. Böttcher, H. Künzel, D. Stanze, M. Schell, and B. Sartorius, "Next generation 1.5 μm terahertz antennas: mesa-structuring of InGaAs/InAlAs photoconductive layers," *Opt. Express*, vol. 18, no. 3, pp. 2296-2301, 2010.

[63] M. Suzuki and M. Tonouchi, "Fe-implanted InGaAs photoconductive terahertz detectors triggered by 1.56 μm femtosecond optical pulses," *Appl. Phys. Lett.*, vol. 86, no. 16, 163504, 2005.

[64] M. Suzuki and M. Tonouchi, "Fe-implanted InGaAs terahertz emitters for 1.56 μm wavelength excitation," *Appl. Phys. Lett.*, vol. 86, no. 5, 051104, 2005.

[65] N. Chimot, J. Mangeney, L. Joulaud, P. Crozat, H. Bernas, K. Blary, and J. F. Lampin, "Terahertz radiation from heavy-ion-irradiated $In_{0.53}Ga_{0.47}As$ photoconductive antenna excited at 1.55 μm," *Appl. Phys. Lett.*, vol. 87, no. 19, 193510, 2005.

[66] F. Sizov and A. Rogalski, "THz detectors," *Prog.Quant. Elec.*, vol. 34, no. 5, pp. 278-347, 2010.

[67] B. S. Karasik, D. Olaya, J. Wei, S. Pereverzev, M. E. Gershenson, J. H. Kawamura, W. R. McGrath, and A. V. Sergeev, "Record-low NEP in hot-eletron titaium nanobolometers," *IEEE Trans. Appl. Supercond.*, vol. 17, no. 2, pp. 293-297, 2007.

[68] E. H. Putley, "Thermal detectors," in: R.J. Keyes (Ed.), Optical and Infrared Detectors, Springer, Berlin, Germany, 1977.

[69] M. C. Gaidis, H. M. Pickett, C. D. Smith, S. C. Martin, R. P. Smith, and P. H. Siegel, "A 2.5 THz receiver front-end for spaceborne applications," *IEEE Trans. Microwave Theory Technol.*, vol. 48, no. 4, pp. 733-739, 2000.

[70] G. J. Dolan, T. G. Phillips, and D. P. Woody, "Low-noise 115-GHz mixing in superconducting oxide-barrier tunnel junctions, " *Appl. Phys. Lett.*, vol. 34, no. 5, pp. 347-349, 1979.

[71] J. E. Carlstrom, and J. Zmuidzinas, "Reviews of Radio Science," in: W. R. Stone (Ed), Oxford Univ. Press, Oxford, UK, 1996.

[72] D. Mittleman, "Sensing with Terahertz Radiation," Springer Series in Optical Sciences, Heidelberg, Springer, 2002.

[73] M. V. Exter, and D. R. Grischkowsky, "Characterization of an optoelectronic terahertz beam system," *IEEE Trans. Microw.Theory Tech.*, vol. 38, no. 11, pp. 1684-1691, 1990.

[74] P. U. Jepsen, R. H. Jacobsen, and S. R. Keiding, "Generation and detection of terahertz pulses from biased semiconductor antennas," *J. Opt. Soc. Am. B*, vol. 13, no. 11, pp. 2424-2436, 1996.

[75] P. Y. Han and X. C. Zhang, "Free-space coherent broadband terahertz time-domain spectroscopy," *Meas. Sci. Technol.*, vol. 12, no. 11, pp. 1747-1756, 2001.
[76] W. L. Chan, J. Deibel, and D. M. Mittleman, "Imaging with terahertz radiation," *Rep. Prog.Phys.*, vol. 70, no. 8, pp. 1325-1379, 2007.
[77] T. I. Jeon and D. Grischkowsky, "Characterization of optically dense, doped semiconductors by reflection THz time domain spectroscopy," *Appl. Phys. Lett.*, vol. 72, no. 23, pp. 3032-3034, 1998.
[78] L. Thrane, R. H. Jacobsen, P. U. Jepsen, and S. R. Keiding, "THz reflection spectroscopy of liquid water," *Chem. Phys. Lett.*, vol. 240, no. 4, pp. 330-333, 1995.
[79] M. Nagai, H. Yada, T. Arikawa, and K. Tanaka, "Terahertz time-domain attenuated total reflection spectroscopy in water and biological solution," *Int. J. Infrared Millim.Waves.*, vol. 27, no. 4, pp. 505-515, 2006.
[80] H. Hirori, K. Yamashita, M. Nagai, and K. Tanaka, "Attenuated Total Reflection Spectroscopy in Time Domain Using Terahertz Coherent Pulses," *Jpn. J. Appl. Phys. 2, Lett.*, vol. 43, no. 10A, pp. L1287-L1289, 2004.
[81] D. A. Newnham, P. F. Taday, "Pulsed terahertz attenuated total reflection spectroscopy," *Appl. Spectro.*, vol. 62, no. 4, pp. 394-398, 2008.
[82] H. Hirori, M. Nagai, and K. Tanaka, "Destructive interference effect on surface plasmon resonance in terahertz attenuated total reflection," *Opt. Express*, vol. 13, no. 26, pp. 10801-10814, 2005.
[83] H. Yada, M. Nagai, and K. Tanaka, "The intermolecular stretching vibration mode in water isotopes investigated with broadband terahertz time-domain spectroscopy," *Chem. Phys. Lett.*, vol. 473, no. 4-6, pp. 279-283, 2009.
[84] H. Yada, M. Nagai, and K. Tanaka, "Origin of the fast relaxation component of water and heavy water revealed by terahertz time-domain attenuated total reflection spectroscopy," *Chem. Phys. Lett.*, vol. 464, no. 4-6, pp. 166-170, 2008.
[85] T. Arikawa, M. Nagai, and K. Tanaka, "Hydration structures of 2-butoxyethanol monomer and micelle in solution," *Chem. Phys. Lett.*, vol. 477, no. 1-3, pp. 95-101, 2009.
[86] D. Grischkowsky, S. Keiding, M. V. Exter, and C. Fattinger, "Far-infrared time-domain spectroscopy with terahertz beams of dielectrics and semiconductors," *J. Opt. Soc. Am. B*, vol. 7, no. 10, pp. 2006-2015, 1990.
[87] L. Duvillaret, F. Garet, and J. L. Coutaz, "A reliable method for extraction of material parameters in terahertz time-domain spectroscopy," *IEEE J. Sel. Top. Quantum Electron.*, vol. 2, no. 3, pp. 739-746, 1996.
[88] L. Duvillaret, F. Garet, and J. L. Coutaz, "Highly precise determination of optical constants and sample thickness in terahertz time-domain spectroscopy," *Appl. Optics.*, vol. 38, no. 2, pp. 409-415, 1999.
[89] P. Y. Han, M. Tani, M. Usami, S. Kono, R. Kersting and X. C. Zhang, "A direct comparison between terahertz time-domain spectroscopy and far-infrared Fourier transform spectroscopy," *J. Applied Physics*, vol. 89, no. 4, pp.

2357-2359, 2001.

[90] P. U. Jepsen and B. M. Fischer, "Dynamic range in terahertz time-domain transmission and reflection spectroscopy," *Opt. Lett.*, vol. 30, no. 1, pp. 29-31, 2005.

[91] V. P. Wallace, E. MacPherson, J. A. Zeitler, and C. Reid, "Three-dimensional imaging of optically opaque materials using nonionizing terahertz radiation," *J. Opti. Soc. Am. Aopti. Img. Sci. Vis.*, vol. 25, no. 12, pp. 3120-3133, 2008.

[92] R. P. Cogdill, R. N. Forcht, Y. C. Shen, P. F. Taday, J. R. Creekmore, C. A. Anderson, and J. K. Drennen III, "Comparison of terahertz pulse imaging and near-infrared spectroscopy for rapid non-destructive analysis of tablet coating thickness and uniformity," *J. Pharm. Innov.*, vol. 2, no. 1-2, pp. 29-36, 2007.

[93] Y. C. Shen, S. Y. Zhang, and Y. S. Jiang, "Angular resonance absorption spectra of Langmuir-Blodgett films studied by the photoacoustic techinique," *Thin Solid Films*, vol. 248, no. 1, pp. 36-40, 1994.

[94] W. T. Silfvast, "Laser fundamentals," 2nd ed. Cambridge Univ. Press. pp. 9-39, Cambridge, U.K., 2004.

[95] D. M. Mittleman, M. Gupta, R. Neelamani, R. G. Barniuk, J. V. Rudd, and M. Koch, "Recent advances in terahertz imaging," *Appl. Phys. B.*, vol. 68, no. 6, pp. 1085-1094, 1999.

[96] Z. P. Jiang and X. C. Zhang, "Single-shot spatiotemporal terahertz field imaging," *Opt. Lett.*, vol. 23, no. 14, pp. 1114-1116, 1998.

[97] A. Nahata, J. T. Yardley, and T. F. Heinz, "Free-space electro-optic detection of continuous-wave terahertz radiation," *Appl. Phys. Lett.*, vol. 75, no. 17.pp. 2524-2526, 1999.

[98] A. Nahata, J. T. Yardley, and T. F. Heinz, "Two-dimensional imaging of continuous-wave terahertz radiation using electro-optic detection," *Appl. Phys. Lett.*, vol. 81, no. 6, pp. 963-965, 2002.

[99] T. Kleine-Ostmann, P. Knobloch, M. Koch, S. Hoffmann, M. Breede, M. Hofmann, G. Hein, K. Pierz, M. Sperling, and K. Donhuijsen, "Continuous-wave THz imaging," *Electron.Lett.*, vol. 37, no. 24, pp. 1461-1463, 2001.

[100] Y. C. Shen, T. Lo, P. F. Taday, B. E. Cole, W. R. TYibe, and M. C. Kemp, "Detection and identification of explosives using terahertz pulsed spectroscopic imaging," *Appl. Phys. Lett.*, vol. 86, no. 24, 241116, 2005.

[101] H. B. Liu, Y. Chen, G. J. Bastiaans, and X. C. Zhang, "Detection and identification of explosive RDX by THz diffuse reflection spectroscopy," *Opt. Express*, vol. 14, no. 1, pp. 415-423, 2006.

[102] N. Karpowicz, H. Zhong, C. Zhang, K. I. Lin, J. S. Hwang, J. Xu, and X. C. Zhang, "Compact continuous-wave subterahertz system for inspection applications," *Appl. Phys. Lett.*, vol. 86, no. 5, 054105, 2005.

[103] D. Zimdars, J. S. White, G. Stuk, A. Chernovsky, G. Fichter, and S. Williamson, "Large area terahertz imaging and non-destructive evaluation application," *Insight*, vol. 48, no. 9, pp.537-539, 2006.

[104] S. Wietzke, C. Jansen, F. Rutz, D. M. Mittleman, and M. Koch, "Determination

of additive content in polymeric compounds with terahertz time-domain spectroscopy," *Polym.Testing*, vol. 26, no. 5, pp. 614-618, 2007.

[105] N. Krumbholz, T. Hochrein, N. Vieweg, T. Hasek, K. Kretschmer, M. Bastian, M. Mikulics, and M. Koch, "Monitoring polymeric compounding processes inline with THz time-domain spectroscopy," *Polym. Testing*, vol. 28, no. 1, pp. 30-35, 2009.

[106] S. Wietzke, C. Jordens, N. Krumbholz, M. Koch, B. Baudrit, and M. Bastian, "Terahertz imaging: a new non-destructive technique for the quality control of plastic weld joints," *J. Eur. Opt. Soc. Rapid Public*, vol. 2, pp. 07013, 2007.

[107] C. Jansen, S. Wietzke, O. Peters, M. Scheller, N. Vieweg, M. Salhi, N. Krumbholz, C. Jordens, T. Hochrein, and M. Koch, "Terahertz imaging: applications and perspectives," *Appl. Opt.*, vol. 49, no. 19, pp. E48-E57, 2010.

[108] F. Rutz, M. Koch, S. Khare, M. Moneke, H. Richter, and U. Ewert, "Terahertz quality control of polymeric products," *Int. J. Infrared Millim.Waves*, vol. 27, no. 4, pp. 547-556, 2006.

[109] P. F. Taday, "Applications of terahertz spectroscopy to pharmaceutical sciences," *Philos. Trans. R. Soc. Lond.A, Math.Phys. Eng. Sci.*, vol. 362, no. 1815, pp. 351-362, 2004.

[110] P. F. Taday, I. V. Bradley, D. D. Arnone, and M. Pepper, "Using terahertz pulse spectroscopy to study the crystalline structure of a drug: A case study of the polymorphs of ranitidine hydrochloride," *J. Pharma. Sci.*, vol. 92, no. 4, pp. 831-838, 2003.

[111] J. A. Zeitler, K. Kogermann, J. Rantanen, T. Rades, P. F. Taday, M. Pepper, J. Aaltonen, and C. J. Strachan, "Drug hydrate systems and dehydration processes studied by terahertz pulsed spectroscopy," *Int. J. Pharm.*, vol. 334, no. 1-2, pp. 78-84, 2007.

[112] A. J. Fitzgerald, B. E. Cole, and P. F. Taday, "Nondestructive analysis of tablet coating thicknesses using terahertz pulsed imaging," *J. Pharma. Sci.*, vol. 94, no. 1, pp. 177-183, 2005.

[113] J. A. Spencer, Z. Gao, T. Moore, L. F. Buhse, P. F. Taday, D. A. Newnham, Y. Shen, A. Portieri, and A. Husain, "Delayed release tablet dissolution related to coating thickness by terahertz pulsed image mapping," *J. Pharma. Sci.*, vol. 97, no. 4, pp. 1543-1550, 2008.

[114] W. Kohler, M. Panzner, U. Klotzbach, E. Beyer, S. Winnerl, M. Helm, F. Rutz, C. Jordens, M. Koch, and H. Leitner, "Non-destructive investigation of paintings with THz-radiation," *Proceedings of the European Conference of Non-Destructive Testing*, Berlin, Germany, 2006.

[115] J. B. Jackson, M. Mourou, J. F. Whitaker, I. N. Duling III, S. L. Williamson, M. Menu, and G. A. Mourou, "Terahertz imaging for non-destructive evaluation of mural paintings," *Opt. Coram.*, vol. 281, no. 4, pp. 527-532, 2008.

[116] K. Fukunaga and Y. Ogawa, S. I. Hayashi, and I. Hosako, "Terahertz spectroscopy for art conservation," *IEICE Electron.Exp.*, vol. 4, no. 8, pp. 258-263, 2007.

[117] K. Fukunaga and Y. Ogawa, S. I. Hayashi, and I. Hosako, "Application of

terahertz spectroscopy for character recognition in a medieval manuscript," *IEICE Electron.Exp.*, vol. 5, no. 7, pp. 223-228, 2008.

[118] A. J. L. Adam, P. C. M. Planken, S. Meloni, and J. Dik, "TeraHertz imaging of hidden paint layers on canvas," *Opt. Express*, vol. 17, no. 5, pp. 3407-3414, 2009.

[119]E. J. Candès and T. Tao, "Near optimal signal recovery from random projections: Universal encoding strategies?," *IEEE Trans. Inf. Theory*, vol. 52, no. 12, pp. 5406-5425, 2006.

[120] R. G. Baraniuk, "Compressive sensing," *IEEE Signal Proc. Mag.*, vol. 24, no. 4, pp. 118-120, 2007.

[121] E. J. Candès, "Compressive sampling," *in Int. Congress of Mathematicians*, Madrid, Spain, vol. 3, pp. 1433-1452, 2006.

[122] E. J. Candès and M. B. Wakin, "An introduction to compressive sampling," IEEE Signal Proc. Mag., vol. 25, no. 2, pp. 21-30, 2008.

[123] J. Romberg, "Imaging via compressive sampling," *IEEE Signal Proc. Mag.*, vol. 25, no. 2, pp. 14-20, 2008.

[124] R. G. Baraniuk, "More Is less: Signal processing and the data deluge," *Science*, vol. 331, no. 6018, pp. 717-719, 2011.

[125] M. Fornasier and H. Rauhut, "Compressive sensing," *Chapter in Part 2 of the Handbook of Mathematical Methods in Imaging* (O. Scherzer Ed.), 2011.

[126] M. A. Davenport, M. F. Duarte, Y. C. Eldar, and G. Kutyniok, "Introduction to compressed sensing," *Chapter in Compressed Sensing: Theory and Applications, Cambridge University Press*, 2012.

[127] M. F. Duarte and Y. C. Eldar, "Structured compressed sensing: Theory and applications," *IEEE Trans. on Signal Proc.*, vol. 59, no. 9, pp. 4053-4085, 2011.

[128] R. M. Willett, R. F. Marcia, and J. M. Nichols, "Compressed sensing for practical optical imaging systems: a tutorial," *Opt. Eng.*, vol. 50, no. 7, pp. 072601, 2011.

[129] http://dsp.rice.edu/cs

[130] H. Nyquist, "Certain topics in telegraph transmission theory," *Trans. AIEE*, vol. 47, pp. 617-644, Apr. 1928 Reprint as classic paper in: *Proc. IEEE*, vol. 90, no. 2, 2002.

[131] C. E. Shannon, "Communication in the presence of noise," *Proc. Institute of Radio Engineers*, vol. 37, no.1, pp. 10-21, 1949. Reprint as classic paper in: *Proc. IEEE*, vol. 86, no. 2, 1998.

[132] M. Unser, "Sampling-50 years after Shannon," *Proc. IEEE*, vol. 88, no. 4, pp. 569-587, 2000.

[133] Y. C. Eldar and T. Michaeli, "Beyond bandlimited sampling," *IEEE Signal Proc. Mag.*, vol. 26, no. 3, pp. 48-68, 2009.

[134] J. Ke and M. A. Neifeld, "Optical architectures for compressive imaging," *Applied Optics*, vol. 46, no. 22, 5293-5303, 2007.

[135] M. F. Duarte, M. A. Davenport, D. Takhar, J. N. Laska, T. Sun, K. F. Kelly, and R. G. Baraniuk, "Single-pixel imaging via compressive sampling," *IEEE Signal Proc. Mag.*, vol. 25, no. 2, pp.83-91, 2008.

[136] J. Haupt, W. U. Bajwa, M. Rabbat, and R. Nowak, "Compressed sensing for networked data," *IEEE Signal Proc. Mag*., vol. 25, no. 2, pp. 92-101, 2008.
[137] K. Gedalyahu and Y. C. Eldar, " Time-delay estimation from low-rate samples: A union of subspaces approach," *IEEE Trans. Signal Proc*., vol. 58, no. 6, pp. 3017-3031, 2010.
[138] M. Mishali and Y. C. Eldar. "Blind multi-band signal reconstruction: Compressed sensing for analog signals," *IEEE Trans. Signal Proc*., vol. 57, no. 3, pp. 993-1009, 2009.
[139] K. Gedalyahu, R. Tur, and Y. C. Eldar, "Multichannel sampling of pulse streams at the rate of innovation," *IEEE Trans. Signal Proc*., vol. 59, no. 4, pp. 1491-1504, 2011.
[140] R. G. Baraniuk, V. Cevher and M. B. Wakin, "Low-dimensional models for dimensionality reduction and signal recovery: A geometric perspective," *Proc. IEEE*, vol. 98, no. 6, pp. 959-971, 2010.
[141] R. A. DeVore, "Nonlinear approximation," *Acta Numerica*, vol. 7, pp.51-150, 1998.
[142] A. M. Bruckstein, D. L. Donoho, and M. Elad, "From sparse solutions of systems of equations to sparse modeling of signals and images," *SIAM Rev*., vol. 51, no. 1, pp. 34-81, 2009.
[143] W. B. Pennebaker, J. L. Mitchell, "JPEG still image data compression standard," *Van Nostrand Reinhold*, 1993. *Eighth printing by Kulwer Academic Publishers*, U. S. A., 2004.
[144] D. Taubman, M. Marcellin, "JPEG2000: Image compression fundamentals, standards and practice," *Kluwer Academic Publishers*, U. S. A., 2001.
[145] D. L. Donoho, "De-noising by soft-thresholding," *IEEE Trans. Inf. Theory*, vol. 41, no. 3, pp. 613-627, 1995.
[146] I. F. Gorodnitsky and B. D. Rao, "Sparse signal reconstruction from limited data using FOCUSS: A re-weighted minimum norm algorithm," *IEEE Trans. Signal Proc*., vol. 45, no. 3, pp. 600-616, 1997.
[147] S. S. Chen, D. L. Donoho, and M. A. Saunders, "Atomic decomposition by basis pursuit," *SIAM J. Sci. Computing*, vol. 20, no. 1, pp. 33-61, 1998.
[148] R. Rubinstein, A. M. Bruckstein, and M. Elad, "Dictionaries for sparse representation modeling," *IEEE proceeding*, vol. 98, no. 6, pp. 1045-1057, 2010.
[149] E. J. Candès and D. L. Donoho, "Curvelets - surprisingly effective nonadaptive representation for objects with edges," *Curves and Surfaces*, 1999.
[150] E. J. Candès, L. Demanet, D. L. Donoho, and L. Ying, "Fast descrete curvelet transforms," *Multiscale Modeling & Simulation*, vol. 5, no. 3, pp. 861-899, 2006.
[151] M. N. Do and M. Vetterli, "Contourlets: A directional multiresolution image representation," *Int. conf. image process.*, vol. 1, pp. 357-360, 2002.
[152] M. N. Do and M. Vetterli, "The contourlet transform: an efficient directional multiresolution image representation, " *IEEE Trans. image process.*, vol. 14, no. 12, pp. 2091-2106, 2005.

[153] E. LePennec and S. Mallat, "Sparse geometric image representations with bandelets," *IEEE Trans. Image Process.*, vol. 14, no. 4, pp. 423-438, 2005.
[154] G. Peyre and S. Mallat, "Surface compression with geometric bandelets," ACM Trans. Graph., vol. 24, no. 3, pp. 601-608, 2005.
[155] E. J. Candès, J. Romberg, and T. Tao, "Stable signal recovery from incomplete and inaccurate measurements," *Comm. Pure Appl. Math.*, vol. 59, no. 8, pp. 1207-1223, 2006.
[156] E. J Candès and T. Tao, "Decoding by linear programming," *IEEE Trans. Inf. Theory*, vol. 51, no. 12, pp. 4203-4215, 2005.
[157] M. A. Davenport, J. N. Laska, P. T. Boufouons, and R. G. Baraniuk, "A simple proof that random matrices are democratic," Technical Report TREE 0906, Rice Univ., ECE Dept., 2009.
[158] J. N. Laska, P. T. Boufounos, M. A. Davenport, and R. G. Baraniuk, "Democracy in action: Quantization, saturation, and compressive sensing," *Appl. Comput. Harmon. Anal.*, vol. 31, no. 3, pp. 429-443, 2011.
[159] J. A. Tropp, J. N. Laska, M. F. Duarte, J. K. Romberg, and R. G. Baraniuk, "Beyond Nyquist: Efficient sampling of sparse, bandlimited signals," *IEEE Trans. Inf. Theory*, vol. 56, no. 1, pp. 520-544, 2010.
[160] J. A. Tropp, M. B. Wakin, M. F. Duarte, D. Baron, and R. G. Baraniuk, "Random filters for compressive sampling and reconstruction," *In 31st IEEE International Conference on Acoustics, Speech, and Signal Processing (ICASSP)*, Toulouse, France, 2006.
[161] M. Mishali and Y. C. Eldar, "From theory to practice: Sub-Nyquist sampling of sparse wideband analog signals," *IEEE J. Select. Top. Signal Processing*, vol. 4, no. 2, pp. 375-391, 2010.
[162] J. Romberg, "Compressive sensing by random convolution," *SIAM J. Imag.Sci.*, vol. 2, no. 4, pp. 1098-1128, 2009.
[163] J. P. Slavinsky, J. N. Laska, M. A. Davenport, and R. G. Baraniuk, "The compressive mutliplexer for multi-channel compressive sensing," *In 36th IEEE International Conference on Acoustics, Speech, and Signal Processing (ICASSP)*, Prague, Czech Republic, 2011.
[164] W. U, Bajwa, J. D. Haupt, G. M. Raz, S. J. Wright, and R. D. Nowak, "Toeplitz-structured compressed sensing matrices," *In Proc. IEEE Workshop on Statistical Signal Processing*, pp. 294-298, Washington D. C., USA, 2007.
[165] J. D. Haupt, W. U. Bajwa, G. M. Raz, and R. D. Nowak, "Toeplitz compressed sensing matrices with applications to sparse channel estimation," *IEEE Trans. Inf. Theory*, vol. 56, no. 11, pp. 5862-5875, 2010.
[166] F. Sebert, Y. M. Zou, L. Ying, "Toeplitz block matrices in compressed sensing and their applications in imaging," *in 5th International Conference on Information Technology and Application and Biomedicine*, pp. 47-50, Shenzhen, P. R. C., 2008.
[167] H. Rauhut, "Compressive sensing and structured random matrices," *Theoretical Foundations and Numerical Methods for Sparse Recovery*, vol. 9 of Radon Series Comp. Appl. Math., pp. 1-92. M. Fornasier, ed., deGruyter, 2010.

[168] W. Yin, S. P. Morgan, J. Yang, and Y. Zhang, "Practical compressive sensing with Toeplitz and circulant matrices," Rice University CAAM Technical Report TR10-01, 2010.
[169] M. Herman and T. Strohmer, "High-resolution radar via compressed sensing," *IEEE Trans. Signal Processing*, vol. 57, no. 6, pp. 2275-2284, 2009.
[170] D. L. Donoho, "For most large underdetermined systems of linear equations, the minimal l_1 norm solution is also the sparsest solution," *Comm. Pure Appl. Math.*, vol. 59, no. 6, pp. 797-829, 2006.
[171] D. L. Donoho, "For most large underdetermined systems of linear equations, the minimal l_1 norm near-solution approximates the sparsest near-solution," *Comm. Pure Appl. Math.*, vol. 59, no. 7, pp. 907-934, 2006.
[172] Y. Tsaig, D. L. Donoho, "Extensions of compressed sensing," *Signal Processing*, vol. 86, no. 3,pp. 549-571, 2006.
[173] H. Fang, Q. B. Zhang and S. Wei, "A method of image reconstruction based on sub-gaussian random projection," *J. Computer Research and Development*, vol. 45, no. 8, pp. 1402-1407, 2008.
[174] T. T. Do, T. D. Trany and L. Gan, "Fast compressive sampling with structurally random matrices," *in 33rd IEEE International Conference on Acoustics, Speech and Signal Processing*, pp. 3369-3372, Las Vegas, NV, 2008.
[175] J. Ke and M. A. Neifeld, "Optical architectures for compressive imaging," *Applied Optics*, vol. 46, no. 22, pp. 5293-5303, 2007.
[176] L. Gan, "Block compressed sensing of natural images," *in 15th International Conference on Digital Signal Processing*, IEEE, pp. 403–406, Cardiff, UK, 2007.
[177] B. Logan, "Properties of high-pass signals," PhD thesis, Columbia University, 1965.
[178] D. L. Donoho, M. Elad and V. Temlyakov, "Stable recovery of sparse overcomplete representations in the presence of noise," *IEEE Trans. Inf. Theory*, vol. 52, no. 1, pp. 6-18, 2006.
[179] K. Koh, S. J. Kim and S. Boyd, "An interior-point method for large-scale l_1 regularized least squares," *Journal of machine learning research*, vol. 8, pp. 1519-1555, 2007.
[180] M. A. T. Fiqueiredo, R. D. Nowak and S. J. Wright, "Gradient projection for sparse reconstruction: Application to compressed sensing and other inverse problems," *IEEE Journal of Selected Topics in Signal Processing*, vol. 1, no. 4, pp. 586-598, 2007.
[181] D. L. Donoho and Y. Tsaig, "Fast solution of l_1-norm minimization problems when the solution may be sparse," *Technical Report, Department of Statistics , Stanford University*, USA, 2008.
[182] E. J. Candès, N. Braun and M. B. Wakin, "Sparse signal and image recovery from compressive samples," *In 4th IEEE International Symposium on Biomedical Imaging: From Nano to Macro*, vol. 1-3, pp. 976-979, Arlington, VA, 2007.
[183] D. Needell and J. A. Tropp, "CoSaMP: Iterative signal recovery from

incomplete and inaccurate samples," *Appl. Comput. Harmon. Anal.*, vol. 26, no. 3, pp. 301-321, 2009.
[184] T. Blumensath and M. E. Davies, "Iterative hard thresholding for compressive sensing," *Appl. Comput. Harmon. Anal.*, vol. 27, no. 3, pp. 265-274, 2009.
[185] W. Dai and O. Milenkovic, "Subspace pursuit for compressive sensing signal reconstruction," *IEEE Trans. Inform. Theory*, vol. 55, no. 5, pp. 2230-2249, 2009.
[186] I. Daubechies, M. Defrise, and C. D. Mol, "An iterative thresholding algorithm for linear inverse problems with a sparsity constraint," *Comm. Pure Appl. Math.*, vol. 57, no. 11, pp. 1413-1457, 2004.
[187] M. A. Davenport and M. B. Wakin, "Analysis of orthogonal matching pursuit using the restricted isometry property," *IEEE Trans. Inform. Theory*, vol. 56, no. 9, pp. 4395-4401, 2010.
[188] D. L. Donoho, Y. Tsaig, I. Drori, and J. L. Stark, "Sparse solution of underdetermined linear equations by stagewise orthogonal matching pursuit," submitted for publication, 2007.
[189] S. G. Mallat and Z. F. Zhang. "Matching pursuits with time-frequency dictionaries," *IEEE Trans. Signal Processing*, vol. 41, no. 12, pp. 3397-3415, 1993.
[190] D. Needell and R. Vershynin, "Uniform uncertainty principle and signal recovery via regularized orthogonal matching pursuit," *Found. Comput.Math.*, vol. 9, no. 3, pp. 317-334, 2009.
[191] D. Needell and R. Vershynin, "Signal recovery from incomplete and inaccurate measurements via regularized orthogonal matching pursuit," *IEEE J. Select. Top. Signal Processing*, vol. 4, no. 2, pp. 310-316, 2010.
[192] D. Needell and R. Vershynin, "Greedy signal recovery and uncertainty principles," *Conference on Computational Imaging*., Proceedings of the SPIE, vol. 6814, no. 68140J-12, San Jose, CA, 2008.
[193] N. G. Kingsbury, "Complex wavelets for shift invariant analysis and filtering of signals," *Appl. Comput. Harmon. Anal.*, vol. 10, no. 3, pp. 234-253, 2001.
[194] T. Blumensath and M. E. Davies, "Iterative thresholding for sparse approximations," *Journal of Fourier Analysis and Applications*, vol. 14, no. 5-6, pp. 629-654, 2007.
[195] L. I. Rudin, S. Osher, and E. Fatemi, "Nonlinear total variation based noise removal algorithms," *Physica D*, vol. 60, no. 1-4, pp. 259-268, 1992.
[196] M. S. Lobo, L. Vandenberghe, S. Boyd and H. Lebret, "Applications of second-order cone programming," *Linear Algebra and its Applications*, vol. 284, no. 1-3, pp. 193-228, 1998.
[197] D. Takhar, J. Laska, M. Wakin, M. Duarte, D. Baron, S. Sarvotham, K. Kelly, and R. Baraniuk, "A new compressive imaging camera architecture using optical-domain compression," *Proc. SPIE*, vol. 6065, pp. 6509, 2006.
[198] D. J. Brady, K. Choi, D. L. Marks, R. Horisaki, and S. Lim, "Compressive holography," *Opt. Express*, vol. 17, no. 15, pp. 13040-13049, 2009.
[199] M. E. Gehm, R. John, D. J. Brady, R. M. Willett, and T. J. Schulz, "Single-shot

compressive spectral imaging with a dual-disperser architecture," *Opt. Express*, vol. 15, no. 21, pp. 14013-14027, 2007.

[200] F. J. Herrmann, Y. A. Erlangga, and T. T. Y. Lin, "Compressive simultaneous full-waveform simulation," *Geophys.*, vol. 74, no. 4, pp. A35-A40, 2009.

[201] B. Jafarpour, V. K. Goyal, D. B. McLaughlin, and W. T. Freeman, "Transform-domain sparsity regularization of inverse problems in geosciences," *Geophys.*, vol. 74, no. 5, pp. R69-R83, 2009.

[202] M. Lustig, D. Donoho, and J. M. Pauly, "Sparse MRI: The application of compressed sensing for rapid MR imaging," *Magnetic Resonance in Medicine*, vol. 58, no. 6, pp. 1182-1195, 2007.

[203] J. Provost and F. Lesage, "The application of compressed sensing for photo-acoustic tomography," *IEEE Trans. Med. Imaging*, vol. 28, no. 4, pp. 585-594, 2009.

[204] D. Zimdars, "High speed terahertz reflection imaging,"*Proc. SPIE*,vol. 5692, pp. 255-259, 2005.

[205] W. U, Bajwa, J. D. Haupt, G. M. Raz, S. J. Wright, and R. D. Nowak, "Toeplitz-structured compressed sensing matrices," In Proc. IEEE Workshop on Statistical Signal Processing, pp. 294-298, Washington D. C., USA, 2007.

[206] J. D. Haupt, W. U. Bajwa, G. M. Raz, and R. D. Nowak, "Toeplitz compressed sensing matrices with applications to sparse channel estimation," IEEE Trans. Inf. Theory, vol. 56, no. 11, pp. 5862-5875, 2010.

[207] F. Sebert, Y. M. Zou, L. Ying, "Toeplitz block matrices in compressed sensing and their applications in imaging," in 5th International Conference on Information Technology and Application and Biomedicine, pp. 47-50, Shenzhen, P. R. C., 2008.

[208] H. Rauhut, "Compressive sensing and structured random matrices," Theoretical Foundations and Numerical Methods for Sparse Recovery, vol. 9 of Radon Series Comp. Appl. Math., pp. 1-92. M. Fornasier, ed., deGruyter, 2010.

[209] W. Yin, S. P. Morgan, J. Yang, and Y. Zhang, "Practical compressive sensing with Toeplitz and circulant matrices," Rice University CAAM Technical Report TR10-01, 2010.

[210] M. Herman and T. Strohmer, "High-resolution radar via compressed sensing," IEEE Trans. Signal Processing, vol. 57, no. 6, pp. 2275-2284, 2009.

[211] D. L. Donoho, "For most large underdetermined systems of linear equations, the minimal l1 norm solution is also the sparsest solution," Comm. Pure Appl. Math., vol. 59, no. 6, pp. 797-829, 2006.

[212] D. L. Donoho, "For most large underdetermined systems of linear equations, the minimal l1 norm near-solution approximates the sparsest near-solution," Comm. Pure Appl. Math., vol. 59, no. 7, pp. 907-934, 2006.

[213] Y. Tsaig, D. L. Donoho, "Extensions of compressed sensing," Signal Processing, vol. 86, no. 3,pp. 549-571, 2006.

[214] H. Fang, Q. B. Zhang and S. Wei, "A method of image reconstruction based on sub-gaussian random projection," J. Computer Research and Development, vol. 45, no. 8, pp. 1402-1407, 2008.

[215] T. T. Do, T. D. Trany and L. Gan, "Fast compressive sampling with structurally random matrices," in 33rd IEEE International Conference on Acoustics, Speech and Signal Processing, pp. 3369-3372, Las Vegas, NV, 2008.
[216] L Gan, L Liu, YC Shen, “Golay sequence for partial Fourier and Hadamard compressive imaging”, 2013 IEEE International Conference on Acoustics, Speech and Signal Processing (ICASSP), (2013) 6048-6052
[217] Shrekenhamer, David, Claire M. Watts, and Willie J. Padilla. "Terahertz single pixel imaging with an optically controlled dynamic spatial light modulator," Optics Express, vol. 21, no.10, pp. 12507-12518, 2013.
[218] Nachappa Gopalsami, Shaolin Liao, Thomas W. Elmer, Eugene R. Koehl, Alexander Heifetz, Apostolos C. Raptis, "Passive millimeter-wave imaging with compressive sensing", Opt. Eng, 51(9), 091614, 2012.
[219] M. F. Duarte, M. A. Davenport, D. Takhar, J. N. Laska, K. F. Kelly and R. G. Baraniuk, "Single-pixel imaging via compressive sampling,"IEEE Sig. Proc. Mag., vol. 25, no. 2, pp. 83-91, 2008.
[220] A. Heidari and D. Saeedkia, "A 2D Camera Design with a Single-pixel Detector,"34th International Conference on infrared, millimeter, and terahertz waves, vol. 1-2, 694-695, Pusan, South Korea, 2009.
[221] H. Shen, N. Newman, L. Gan, S. C. Zhong, Y. Huang and Y. C. Shen, "Compressed terahertz imaging system using a spin disk,"35th International Conference on infrared, millimeter, and terahertz waves, Rome, Italy, 2010.
[222] Kai-Erik Peiponen, J. Axel Zeitler, Makoto Kuwata-Gonolami, "Generation and Detection of Terahertz Radiation". In: W. T. Rhodes(Ed.): "Terahertz Spectroscopy and Imaging". vol. 171. (USA: Springer, 2013), pp. 1-25
[223] Zhang, Lin, et al. "FSIM: a feature similarity index for image quality assessment." IEEE Trans. Image Processing, vol. 20, no. 8, pp. 2378-2386, 2011
[224] W. U, Bajwa, J. D. Haupt, G. M. Raz, S. J. Wright, and R. D. Nowak, "Toeplitz-structured compressed sensing matrices,"In Proc. IEEE Workshop on Statistical Signal Processing, pp. 294-298, Washington D. C., USA, 2007.
[225] F. Sebert, Y. M. Zou, L. Ying, "Toeplitz block matrices in compressed sensing and their applications in imaging,"in 5th International Conference on Information Technology and Application and Biomedicine, pp. 47-50, Shenzhen, P. R. C., 2008.
[226] H. Rauhut, "Compressive sensing and structured random matrices,"Theoretical Foundations and Numerical Methods for Sparse Recovery, vol. 9 of Radon Series Comp. Appl. Math., pp. 1-92. M. Fornasier, ed., deGruyter, 2010.
[227] J. D. Haupt, W. U. Bajwa, G. M. Raz, and R. D. Nowak, "Toeplitz compressed sensing matrices with applications to sparse channel estimation," IEEE Trans. Inf. Theory, vol. 56, no. 11, pp. 5862-5875, 2010.
[228] W. Yin, S. P. Morgan, J. Yang, and Y. Zhang, "Practical compressive sensing with Toeplitz and circulant matrices," Rice University CAAM Technical Report TR10-01, 2010.
[229] Hore, Alain,and Djemel Ziou. "Image quality metrics: PSNR vs. SSIM." in 20th International Conference on Pattern Recognition, IEEE, pp. 2366-2369, Istanbul,

Turkey, 2010.
[230] Hsieh, H., Andrews, H.: ‘Cubic splines for image interpolation and digital filtering’, IEEE Trans.Acoustics, Speech and Signal Processing,1983, vol. 31, no. 4, pp. 532-540
[231] Islam, S.R., Maity, S.P.,Ray, A.K.: ‘On compressed sensing image reconstruction using multichannel fusion and adaptive filtering’, in 2015 International Conference on Image Processing Theory, Tools and Applications (IPTA), Orleans, France,2015, pp. 479-484
[232] L. Gan, "Block compressed sensing of natural images," in Proceedings of the International Conference on Digital Signal Processing, Cardiff, UK, July 2007, pp. 403-406.
[233] http://www.sci-techdaresbury.com/about/sci-tech/
[234] Peter Williams, on behalf of the ALICE team, “10 years of ALICE: From Concept to Operational User Facility,” the 56th ICFA advanced beam dynamics workshop on energy recovery linacs, June,2015.
[235] Q. Wu and X.C. Zhang, "Free-space electro-optics sampling of mid-infrared pulses,"*Appl. Phys. Lett.*,vol. 71, no. 10, pp. 1285-1286, 1997.
[236] M. Duarte and Y. Eldar, "Structured compressed sensing: From theory to applications," IEEE Trans. Signal Processing, vol. 59, no. 9, pp. 4053-4085, Sep. 2011.
[237] T. Do, L. Gan, N. Nguyen, and T. Tran, "Fast and efficient compressive sensing using structurally random matrices," IEEE Trans. Signal Processing, vol. 60, no. 1, pp. 139-154, Jan. 2012.
[238] M. Golay, "Complementary series," IEEE Trans. Inform. Theory, vol. 7, no. 2, pp. 82-87, Apr. 1961.
[239] R. Coifman, F. Geshwind, and Y. Meyer, "NESTA: a fast and accurate first-order method for sparse recovery," SIAM Journal on Imaging Sciences, vol. 4, no. 1, pp. 1-39, 2011.
[240] N. P. Pitsianis, D. J. Brady, and X. Sun, "Sensor-layer image compression based on the quantized cosine transform," Proc. SPIE, vol. 5817, pp. 250-257, 2005.